



**POLITECNICO  
DI TORINO**

**POLITECNICO DI TORINO**

Master Degree course in Electronic Engineering

Master Degree Thesis

# **Optical fiber sensors for low cost water quality monitoring**

**Supervisors**

Prof. Guido PERRONE

**Candidate**

Chiara BELLEZZA PRINSI

ACADEMIC YEAR 2021-2022

## Abstract

Ensure availability and sustainable management of water and sanitation for all is one of the Sustainable Development Goals settled by the United Nations for the 2030. However, today, billions of people in the world still live without safe drinking water and millions die every year due to waterborne diseases.

People are dying due to contaminated and polluted water. For this reason, a new, real-time, effective and low-cost device to detect various pollution could help improving the quality of life of a huge part of humanity, not to mention the reduction in deaths.

Nowadays the water quality monitoring is performed without a real global "water quality standard": most water quality is evaluated at a local or national level. The World Health Organization (WHO) has released guidelines for the drinking water quality, but it is not mandatory to follow guidelines and it is under the responsibility of the local authority to ensure safe water.

This thesis investigates the possibility of applying optical fiber-based sensors for real time, continuous and on field monitoring of water for the early detection of the quality variation. The focus of the thesis is the development of a very low-cost device able to help in particular the developing countries, in which the water quality problem is the worst.

The choice of working with optical fibers is due to their advantages, like small dimensions, robustness to environment, electromagnetic immunity, and the possibility to implement real time and remote sensing. Thanks to those advantages, optical fibers are widely used both in scientific and industrial applications. Water quality monitoring can take advantage of these qualities too, overcoming the limitations of traditional measurement approaches, which require in-situ sampling, transportation to labs, and finally the quantification through complex instruments. And this requires hours to days and specialized technicians able to perform tests and read the results.

The goal is to build a low cost and small device, that allows the real-time and ubiquitous monitoring of the water quality, and without the need of trained personnel for the reading of the results. This is done implementing an optical fiber-based refractometer that exploits the surface plasmon resonance (SPR) to measure the variation of the refractive index, instantly warning any change occurred from the normal situation.

The surface plasmon is an electromagnetic surface wave that propagates in a direction parallel to the interface between the metal and the outer dielectric, being very sensitive to any change that can occur at the external medium (water in this application). SPR sensors are known for their very high sensitivity, which allows the detection of part per million (ppm) contamination in the water. The SPR sensor is complemented by an all-fiber temperature sensor based on fiber Bragg gratings to compensate for the temperature dependence.

The results shows that an accurate refractive index sensing can be done also with low-cost devices such as a LED and a photodiode connected to a microcontroller. This keeps also very compact the device and allows also to build a solution usable at the end side of the water distribution system, ideally on every tap. The actual device is a prototype implemented for preliminary validations of the results. Further studies must be done to improve the LED's driving circuit to integrate it removing the external breadboard and to design a proper shape of the device to mount it on taps or pipes.

# Contents

<b>List of Figures</b>	v
<b>List of Tables</b>	viii
<b>1 Introduction</b>	1
<b>2 Theoretical background</b>	5
2.1 Surface Plasmon Resonance (SPR)	5
2.2 Prism implementation	6
2.3 Optical fiber implementation	8
2.4 Interrogation methods	10
2.4.1 Wavelength interrogation	10
2.4.2 Intensity interrogation	10
2.4.3 Angular interrogation	11
2.5 Transmission and reflection configurations	11
<b>3 Wavelength interrogation</b>	13
3.1 Experimental setup and materials	13
3.2 Experimental tests	15
3.2.1 First test	17
3.2.2 Overnight stability	18
3.2.3 Second test	21
3.2.4 Third test	24
3.3 Refractive index of a solution	26
3.4 Real measurements	28
3.4.1 Test 1	29
3.4.2 Test 2	30
<b>4 Intensity interrogation</b>	33
4.1 Implementation of the theoretical model	33
4.1.1 Simulation with 1 LED	37
4.1.2 Simulations with a single laser	38
4.1.3 Simulations with two lasers	39
4.1.4 Simulation with two LED	40
4.2 Experimental setup and materials	42

4.3	Experimental test with one LED . . . . .	47
<b>5</b>	<b>Temperature compensation</b>	<b>51</b>
5.1	Theoretical model . . . . .	51
5.2	Intensity interrogation . . . . .	52
5.2.1	Temperature compensation: measurements . . . . .	52
5.2.2	Refractive index measurements with temperature compensation . .	61
5.3	Wavelength interrogation . . . . .	62
5.3.1	Temperature compensation: measurements . . . . .	62
<b>6</b>	<b>Low-cost set-up</b>	<b>69</b>
6.1	Experimental set-up and materials . . . . .	69
6.1.1	Design of the fiber holder and set-up . . . . .	69
6.2	Experimental tests . . . . .	71
6.2.1	Acquisition with temperature compensation . . . . .	72
6.3	Real measurements . . . . .	77
6.3.1	Lago Maggiore - Angera . . . . .	77
6.3.2	Lago Maggiore - Stresa . . . . .	77
6.3.3	Lago d'Orta . . . . .	79
<b>7</b>	<b>Conclusion</b>	<b>83</b>
	<b>Bibliography</b>	<b>85</b>

# List of Figures

1.1	Global Water quality monitoring market [1]. . . . .	1
2.1	Prism based configurations. (a) Otto configuration (b) Kretschmann configuration. . . . .	6
2.2	Angular shift due dielectric refractive index variation. . . . .	7
2.3	Basic structure (not in scale) of a OFSPR sensor. . . . .	8
2.4	Numerical Aperture acceptance cone representation. . . . .	9
2.5	Intensity and wavelength interrogation methods. . . . .	10
3.1	Set-up components. . . . .	14
3.2	Set-up overview, wavelength interrogation. . . . .	14
3.3	Acquired spectra, test with water and alcohol. . . . .	15
3.4	Normalized spectra with respect to air reference, test with water and alcohol. . . . .	16
3.5	Normalized spectra with respect to air reference, test with water and salt. . . . .	17
3.6	Normalized spectra with respect to air reference, test 1. . . . .	18
3.7	Normalized spectra with respect to air reference, test 1. . . . .	19
3.8	Wavelength of dips with filter 1, overnight stability. . . . .	20
3.9	Wavelength of dips with filter 2, overnight stability. . . . .	21
3.10	Normalized spectra with respect to air reference with interpolation, overnight stability. . . . .	21
3.11	Wavelength of dips after interpolation, overnight stability. . . . .	22
3.12	Wavelength of dips, test 2. . . . .	22
3.13	Wavelength of dips after interpolation, test 2. . . . .	23
3.14	Wavelength of dips after interpolation and filtering, test 2. . . . .	23
3.15	Average value of wavelength for each alcohol concentration, test 2. . . . .	24
3.16	Wavelength of dips, test 3. . . . .	25
3.17	Wavelength of dips with interpolation, test 3. . . . .	25
3.18	Wavelength of dips after interpolation and filtering, test 3. . . . .	26
3.19	Average value of wavelength for each alcohol concentration, test 3. . . . .	26
3.20	Refractive index of different water-alcohol solutions in function of wavelength. . . . .	28
3.21	Refractive index of water-alcohol solution in function of alcohol concentration. . . . .	28
3.22	Acquired spectra, test with different water samples. . . . .	29

3.23	Normalized spectra with respect to air reference, test with different water samples. . . . .	30
3.24	Normalized spectra with respect to air reference and interpolation, test with different water samples. . . . .	30
3.25	Acquired spectra, test with different water samples. . . . .	31
3.26	Normalized spectra with respect to air reference, test with different water samples. . . . .	32
3.27	Normalized spectra with respect to air reference and interpolation, test with different water samples. . . . .	32
4.1	2D slab structure. . . . .	33
4.2	Reflectivity of the SPR sensor using water as dielectric ( $n = 1.33$ ). . . . .	36
4.3	Reflectivity of the SPR sensor using different water-alcohol solutions as dielectric. . . . .	36
4.4	Simulation of the SPR behaviour with a LED source (670 nm). . . . .	37
4.5	Output power in function of refractive index, simulation with one LED. . . . .	39
4.6	Simulation of the SPR behaviour with a laser source (672 nm). . . . .	40
4.7	Output power in function of refractive index, simulation with one laser. . . . .	41
4.8	Simulation of the SPR behaviour with a laser source (660 and 740 nm). . . . .	42
4.9	Output power in function of refractive index, simulation with two lasers. . . . .	42
4.10	Simulation of the SPR behaviour with a laser source (645 and 740 nm). . . . .	43
4.11	Output power in function of refractive index, simulation with two lasers. . . . .	43
4.12	Difference of two output power in function of refractive index with linear interpolation. . . . .	44
4.13	Simulation of the SPR behaviour with a LED source (645 and 735 nm). . . . .	44
4.14	Output power in function of refractive index, simulation with two LED. . . . .	45
4.15	Difference of two output power in function of refractive index with linear interpolation. . . . .	45
4.16	LED testing. . . . .	47
4.17	Spectral response of the SPR sensor and of the LED used in the set-up (not in scale). . . . .	48
4.18	Output power in function of refractive index. . . . .	49
5.1	Acquisition of power and temperature. . . . .	53
5.2	Acquired power in function of temperature. . . . .	53
5.3	Acquisition of power and temperature. . . . .	54
5.4	Acquisition of power and temperature. . . . .	54
5.5	Acquired power in function of temperature. . . . .	55
5.6	Acquired power in function of temperature. . . . .	55
5.7	Acquisition of power and temperature. . . . .	56
5.8	Acquired power in function of temperature. . . . .	56
5.9	Acquisition of power and temperature. . . . .	57
5.10	Acquired power in function of temperature. . . . .	57
5.11	Acquisition of power and temperature. . . . .	58
5.12	Acquired power in function of temperature. . . . .	58

5.13	Multiple temperature acquisitions. . . . .	59
5.14	Temperature acquisition with filtering. . . . .	60
5.15	Acquisition of power and temperature. . . . .	61
5.16	Acquired power compensated in temperature. . . . .	62
5.17	Wavelength of the dips and temperature. . . . .	63
5.18	Wavelength of the dips filtered and temperature. . . . .	63
5.19	Acquired power in function of the temperature with interpolation. . . . .	64
5.20	Wavelength of the dips and temperature. . . . .	64
5.21	Wavelength of the dips filtered and temperature. . . . .	65
5.22	Acquired power in function of the temperature with interpolation. . . . .	65
5.23	Wavelength of the dips and temperature. . . . .	66
5.24	Wavelength of the dips filtered and temperature. . . . .	66
5.25	Acquired power in function of the temperature with interpolation. . . . .	67
6.1	3D view of the fiber holder. . . . .	70
6.2	Intensity interrogation setup. . . . .	71
6.3	Voltage and temperature acquisition with patchcord. . . . .	72
6.4	Voltage and temperature acquisition with patchcord, filtered. . . . .	72
6.5	Voltage and temperature acquisition with room temperature tap water. . . . .	73
6.6	Voltage and temperature acquisition with room temperature tap water, filtered. . . . .	73
6.7	Voltage and temperature acquisition with hot tap water. . . . .	74
6.8	Voltage and temperature acquisition with hot tap water, filtered. . . . .	75
6.9	Voltage in function of temperature. . . . .	75
6.10	Acquired voltage with compensation. . . . .	76
6.11	Voltage acquisition for Lago Maggiore - Angera. . . . .	78
6.12	Voltage acquisition for Lago Maggiore - Angera, filtered and with temperature compensation. . . . .	78
6.13	Voltage acquisition for Lago Maggiore - Stresa. . . . .	79
6.14	Voltage acquisition for Lago Maggiore - Stresa, filtered and with temperature compensation. . . . .	79
6.15	Voltage acquisition for Lago d'Orta. . . . .	80
6.16	Voltage acquisition for Lago d'Orta, filtered and with temperature compensation. . . . .	80

# List of Tables

3.1	Wavelength of the minimum of the actual acquired spectra and the interpolated one. . . . .	31
3.2	UVC quantities for sanitation. . . . .	31
3.3	Wavelength of the minimum of the actual acquired spectra and the interpolated one. . . . .	32
4.1	Summary of simulation results. . . . .	46
5.1	Summary of the computation of the temperature coefficient, intensity interrogation. . . . .	59
5.2	Summary of the computation of the temperature coefficient, wavelength interrogation. . . . .	67

# Chapter 1

## Introduction

Ensure availability and sustainable management of water and sanitation for all is one of the Sustainable Development Goals (SDG) settled by the United Nations (UN) for the 2030 [2].

Today, half-way in the ambitious program of the UN, still billions of people in the world live without safe drinking water (one in four people in 2020) and die every year due to water-related diseases. The approaching deadline demands new actions and if we want to invert current trends, a quadrupling of current rates of progress is required to reach the goal by 2030 [3]. Among them, a real-time and low-cost device to effectively detect various pollution could provide a significant help.

Nowadays the water quality monitoring is performed without a real global “water quality standard”: most water quality is evaluated at a local or national level. Only the World Health Organization (WHO) has released guidelines for the drinking water quality, but it is not mandatory to follow these guidelines, as it is under the responsibility of the local authority to ensure safe water [4].

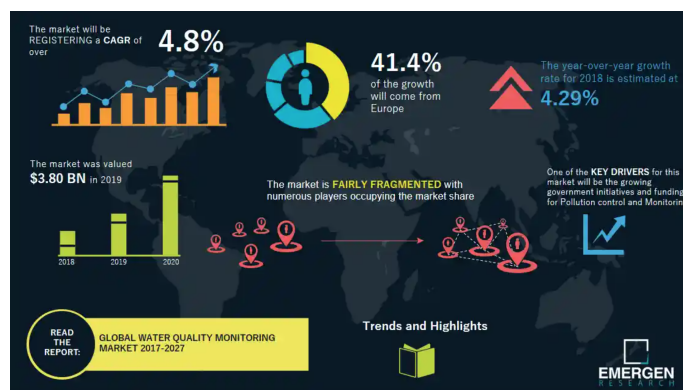


Figure 1.1: Global Water quality monitoring market [1].

*“The Global Water quality monitoring market size was valued at USD 3.80 Billion in 2019 and the forecasts predict to reach USD 5.38 Billion by 2027 at a CAGR of 4.8%” [1] (Fig. 1.1).*

The increase in the amount of industrial toxic wastes and chemicals sent to water resources causes an increase in the need of water quality monitoring to ensure safe drinking water to all. The lack of freshwater, especially in developing countries, has led to an increase of government investment in water management systems. The introduction of IoT-based devices in water quality monitoring has led to an increase in the market demand since it allows collecting and trace data for remote monitoring. The increasing number of initiatives to control the water quality is slowed down by the high maintenance and installation costs of water quality monitoring systems [1].

But how is the water analysed?

Water is periodically sampled in different places of the distribution system and sent to the laboratory, where tests are performed. This procedure is not easy to perform and does not guarantee the total security of water: the sample must represent the effective composition of the water under test and must maintain properties until the test is performed. Moreover the laboratory analysis requires dedicated instruments, specialized technicians and hours to days to be completed.

The common performed tests are chemical (chloride, heavy metal ion concentration, ammonia etc.), radiological, bacteriological and sensorial (taste, odour, colour) analysis. This, at least where the water supply is constant, can guarantee an adequate water quality. The problem becomes tough when the water supply is not continuous or the network has losses and uncontrolled contamination. In this case the periodical sampling can't provide safe water at the end user. To guarantee a safe distribution of water can be useful to have a distributed monitoring system, ideally in each house: in this way is possible to ensure that the quality of the water is not modified by the travel. Also performing a 24h monitoring allows knowing in each moment if the water is safe and generate an early warning if it is not.

The goal of this work is to build a prototype of a low cost and small device to monitor the quality of water in real time and everywhere. A possible parameter to monitor in order to obtain a qualitative measure of the water quality can be the refractive index.

The refractive index is a dimensionless quantity indicating the ability of refraction of the material; since it depends on the physical and chemical properties of the material composition, its variation can be a good candidate for an indicator of the presence of contaminants. For example, adding 1ppm of chlorine will increase the Refractive Index (RI) of  $1 \times 10^{-4}$  and a variation of  $1^\circ\text{C}$  of the temperature causes a variation of  $-1 \times 10^{-4}$  [5, 6].

Clearly, a sensor based on the measurement of the refractive index only cannot distinguish the origin of the contamination. Nevertheless a refractive index sensor is very attractive because it can be used a issue an early warning that something has changed and thus more specific tests are needed. Moreover, it can be relatively low cost. Besides, more complex implementations can developed for molecule specific sensing, and this can be used to detect the presence of traces of well-defined contaminants.

The proposed device is a fiber-based refractometer that exploits the Surface Plasmon Resonance (SPR) to analyze water-based fluids. The main focus is the development of a

low-cost device to detect pollutant quantities in water to enable the realization of a widely employable monitoring networks, particularly suitable for application in underdeveloped countries. SPR allows fabricating sensors capable of measuring very small refractive index variations of the surrounding dielectric and this can be used to detect any change in the water composition, down to part-per-billion. Particularly important is to highlight that the developed system works in real-time and thus it allows overcoming the limitations of traditional measurement approaches, which require in-situ sampling first, then transportation of the samples in a lab, and finally the quantification through complex instruments. And this requires hours to days.



## Chapter 2

# Theoretical background

### 2.1 Surface Plasmon Resonance (SPR)

SPR is a phenomenon that occurs at the interface between two materials with the real part of the permittivity has opposite signs, such as in the case of a thin metallic film deposited onto a dielectric.

In these conditions, for a p-polarized wave at a certain angle of incidence the refraction of the light becomes almost zero. For an appropriate thickness of the metal layer, the incidence angle becomes highly sensitive to the refractive index of the medium surrounding the metal, allowing the usage of this principle to build a refractometer.

A fraction of the light that enters in the system at a defined angle interacts with the electrons at the metal film interface, reducing the amount of reflected light. Physically there is a surface electromagnetic wave that propagates parallel to the metal/dielectric surface. Being on the interface with the dielectric (e.g., water) these waves are really sensitive to any variation of the external refractive index [7].

To excite the surface plasmons a light beam in visible or infrared range is needed. Only the p-polarized light (or TM, where the polarisation is parallel to the plane of the interface) passing through a prism with a thin layer of metal on top excites the resonant condition at a given angle and wavelength [8].

A full theoretical and analytical explanation of the phenomenon can be provided solving Maxwell's equation at the interface of metal and dielectric, considering the proper boundary conditions.

The first condition to satisfy is about the materials to use: one must be positive but with smaller absolute value than the second one, that must be negative.

Using any dielectric and metals, respectively, we are sure to satisfy this first condition.

A second condition to satisfy is to have a p-polarized light evanescent in the dielectric medium. This last condition is satisfied by Eq. 2.1 between the propagation constants:

$$k_{\text{sp}}(\omega) = \frac{\omega}{c} \sqrt{\frac{\varepsilon_{\text{m}} \cdot \varepsilon_{\text{d}}}{\varepsilon_{\text{m}} + \varepsilon_{\text{d}}}} > k_{\text{light}}(\omega) = \frac{\omega}{c} \sqrt{\varepsilon_{\text{d}}} \quad (2.1)$$

This means that in a dielectric the light has not enough energy to excite the plasmon wave in the metal interface. In order to have a SPW excitation we need that, for a given

$\omega$  value, the two sides of Eq. 2.1 have at least one common value. Considering an interface between a glass ( $\varepsilon_g \approx 1.45$ ), a thin layer of gold and water ( $\varepsilon_d \approx 1.33$ ) the interaction point is at 615 nm. Exactly at this wavelength can be seen the dip in the reflectivity in an experimental implementation.

## 2.2 Prism implementation

To experimentally generate the evanescent waves two different setups can be implemented.

The first one, proposed by Otto, presents a glass prism and a thin metal layer parallel to the surface of the prism. Glass and metal are separated by the dielectric layer (Fig. 2.1 a).

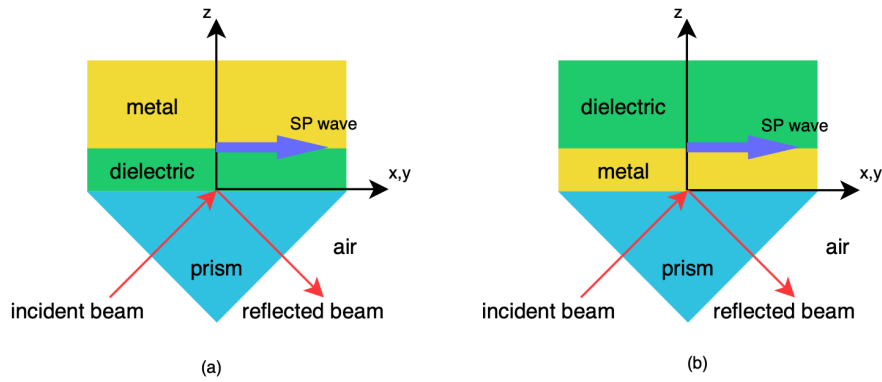


Figure 2.1: Prism based configurations. (a) Otto configuration (b) Kretschmann configuration.

The dielectric must be really thin (within 200 nm) in order to avoid the complete field decay before the interface with the metal. This constraint is not so easy to satisfy during the production of the set-up [9].

For this reason there is a second configuration (implemented by Kretschmann, Fig. 2.1b) that puts the metal layer directly in contact with the glass prism, produced by evaporating the metal on the glass, obtaining the same experimental result reducing the manufacturing complexity. Also in this case the metallic film must be thin enough to avoid field extinction, but evaporating the metal is quite easy to obtain a 50/60 nm layer [7].

To obtain the evanescent wave the incident TM light must have an incident angle  $\theta_i$  larger than the critical angle  $\theta_c$ ; this is possible thanks to the higher refractive index of the material in contact with the glass. Therefore, the light is in total internal reflection (TIR), and the generated wave is parallel to the interface and the amplitude decays moving from the interface. The evanescent wave propagation constant is given by Eq. 2.2:

$$k_{ev}(\omega) = \frac{\omega}{c} \sqrt{\varepsilon_g} \sin \theta_i \quad (2.2)$$

Satisfying the relation in Eq. 2.3 there is a perfect match between the evanescent wave propagation constant  $k_{\text{ev}}$  and the lossy propagation constant  $k_{\text{sp}}$ , allowing the creation of the plasmon wave at the metal-dielectric interface.

$$\frac{\omega}{c} \sqrt{\varepsilon_g} \sin \theta_i = \frac{\omega}{c} \sqrt{\frac{\varepsilon_m \cdot \varepsilon_d}{\varepsilon_m + \varepsilon_d}} \quad (2.3)$$

The angle that allows the match is called resonance angle. The interrogation method used with those two configurations is called “angular interrogation method” and requires a monochromatic light at a suitable wavelength (given by Eq. 2.1), allowing the detection of the angle that generates the resonance.

As it can be seen from Eq. 2.3 the angle depends from the dielectric refractive index, allowing the use of it as a refractometer [7].

Considering the entire spectrum instead of a single wavelength the reflectivity presents a dip. The position of the peak represents the angular shift due to the variation of the dielectric permittivity  $\varepsilon_d$ . The angular shift of the reflectivity dip is proportional to the variation of the dielectric refractive index (Fig. 2.2). The minimum value of the reflectivity depends on material parameters like thickness and refractive index.

The missing energy that generates the dip is due to the photons that are absorbed by the metal layer and that are converted in surface plasmons [9].

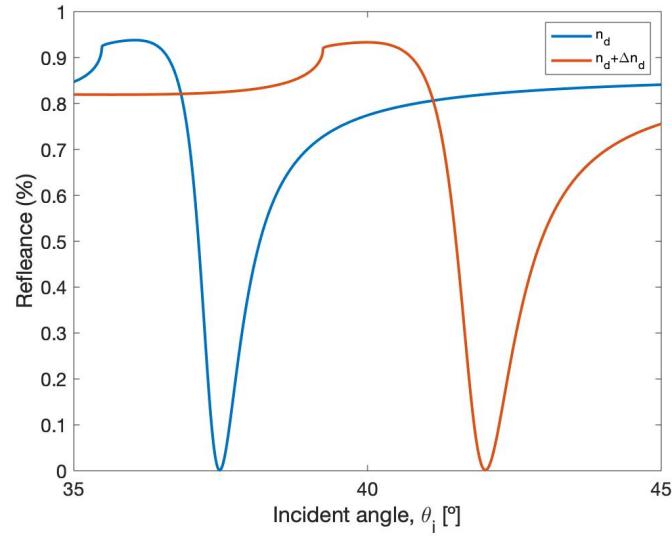


Figure 2.2: Angular shift due dielectric refractive index variation.

## 2.3 Optical fiber implementation

SPR can also be implemented with optical fibers instead of prisms, they are called OFSPR sensors (Optical Fiber SPR sensors).

The configuration is similar to the Kretschmann prism based one. The prism is replaced by the core of the fiber: in a small portion (few cm) of the fiber the cladding is replaced by the thin metal film, created by evaporation on the core. The SPR phenomenon takes place at the section where the metal is deposited. In Fig. 2.3 the basic structure (not in scale) of a OFSPR sensor is displayed. In order to improve the adhesion between glass and metal sometimes an additional chromium or titanium film is added between the core and the thin metal film [9].

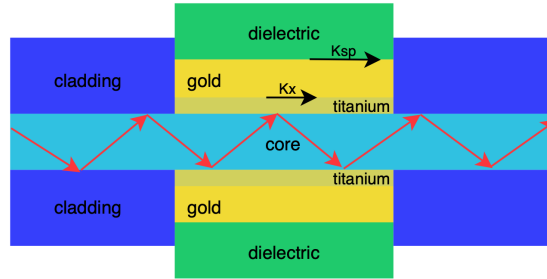


Figure 2.3: Basic structure (not in scale) of a OFSPR sensor.

The use of an optical fiber instead of a prism has some advantages such as lower implementation cost, flexibility, simpler design and possibility to have a portable, light and miniaturised product. All these considerations make optical fibers highly suitable for the creation of sensors to measure refractive index in solutions.

The incident light is coupled at the inner end of the fiber and collected at the end side, where the reflectivity dip can be seen using the wavelength interrogation. Similarly to the prism set-up, also OFSPR exploit TIR to generate the evanescent waves. To guarantee the light confinement the rays propagating in the core must be in TIR at the interface between the core and the cladding of the optical fiber. This is always possible because, considering a multi-mode optical fiber as those used in the experiments, all the rays that propagate into the fiber satisfy the TIR condition, since the accepted angles of a fiber are all included between  $\theta_c$  and  $90^\circ$ , as imposed by the numerical aperture (NA) of the fiber [9]. The numerical aperture is defined by Eq. 2.4 and defines, as illustrated in Fig. 2.4, the acceptance cone of the fiber (Eq. 2.5), determining also the angle of incidence of the light at the glass/metal interface.

$$NA = \sqrt{n_{\text{core}}^2 - n_{\text{cladding}}^2} \quad (2.4)$$

$$\theta_{\text{max}} = \arcsin(NA) \quad (2.5)$$

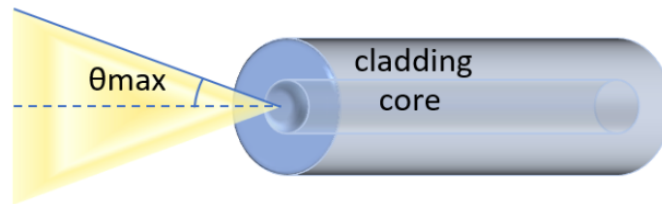


Figure 2.4: Numerical Aperture acceptance cone representation.

Since the NA of the fiber defines the range of acceptable angles is preferable to use the wavelength interrogation method instead of the angular one, in order to have the possibility to detect the whole refractive index range. The wavelength interrogation method works launching the input polychromatic light and observing the wavelength at which the dips occurs instead of the angle. Also in this case the shift is proportional to the refractive index change.

Another issue that must be taken into account is the length of the sensing region: in the prism the light interacts with the metal once and then exits the prism while in an optical fiber the light that enters the fibers interacts several times with the metallic layer before being collected at the end-side. For this reason the sensing region must be designed accurately, also because the number of reflections affects performance parameters, such as SNR and sensitivity.

## 2.4 Interrogation methods

As said, the fiber interrogation method can vary according to the set-up and the application.

### 2.4.1 Wavelength interrogation

The first and most common method is called wavelength interrogation and it is the main method in OFSPR. It requires a white broadband light source, the SPR fiber, and a spectrometer or a spectrum analyser. Using a broad band light at the end side of the fiber the entire spectrum is collected: it presents a dip in correspondence of the resonance wavelength and the position of the dip shifts according to the changes of the external refractive index.

An increase in the refractive index will cause an increase of the wavelength (red shift) while a decreasing of the RI causes a blue shift. This method is widely used in fiber optic SPR sensor because it does not require additional parts in the set-up and it can be easily manufactured [9].

### 2.4.2 Intensity interrogation

The second method commonly used in OFSPR is called intensity interrogation: in this case the source is monochromatic (usually, in case of a gold metallic layer, a red LED or a laser). At the end side the spectrum analyser is replaced by a photodiode that monitors the changes of the intensity at a certain wavelength. The wavelength and the intensity interrogation method are graphically illustrated in Fig. 2.5.

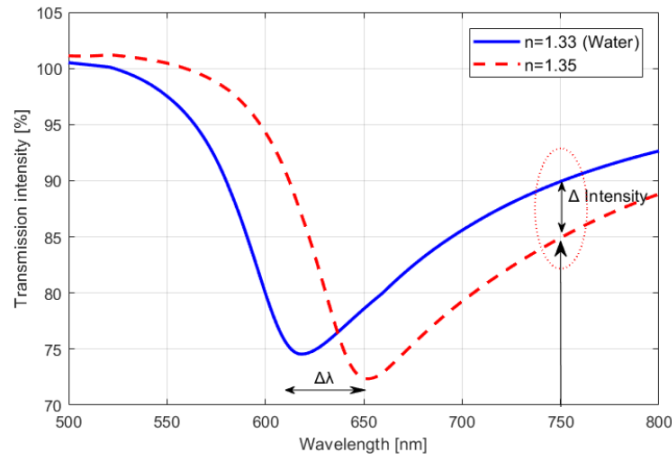


Figure 2.5: Intensity and wavelength interrogation methods.

### 2.4.3 Angular interrogation

The angular interrogation method is mainly used in prisms configuration due to the difficulties of implementation with OFSPR. It requires a monochromatic light that, once coupled with the prism, reaches the metal layer, excites the plasmon wave and then is reflected and exits the prism being collected by a photodiode. In order to achieve the angular monitoring the source must be mounted on a rotatory stage that covers all the angles that allow TIR while the photodiode at the end collects the light. At a certain angle the transmitted light reaches the minimum value: that is the resonance angle for the specific input wavelength, that depends on the external RI. This method can be easily manufactured but the need of the rotatory stage implies a bulky set-up that greatly reduces the advantages of using the optical fibers.

## 2.5 Transmission and reflection configurations

Independently on the interrogation method, OFSPR can be used in two different ways: transmission and reflection [10].

In the first case the sensing region is in the middle of the fiber and the source and the spectrometer are positioned at the two ends of it.

The second configuration is more complex because it presents the sensing region at one end of the fiber, while the source and the spectrometer are positioned at the other end. In order to work, this set-up needs a mirror on the tip of the fiber and a y-junction or a coupler on the other end to separate the two waves.

Both solution have some advantages and some drawbacks.

The major advantage of the transmission set-up is the simplicity: only few components are needed. On the other hand, it can be difficult to manage it in case of use as probe for in-situ measurements, while it can be a good option to monitor a water flow in a pipe. The reflection set-up presents a lot of manufacturing problem, such as the application of the mirror on the tip and the splicing of the coupler. However, it is really useful for probe measurements, exploiting better the advantages of optical fibers.



## Chapter 3

# Wavelength interrogation

### 3.1 Experimental setup and materials

The metal layer on the fibers used for this research were deposited in the clean rooms of Convergent Photonics - Prima Electro S.p.A, an industrial company in the market of high power lasers. More details about the fabrication process can be found in [11].

In particular, fibers having 400  $\mu\text{m}$  core were used. The sensing region is formed by a metal coating made by a 20 nm layer of Titanium (added for adhesive purposes), followed by a 40 nm Gold layer.

A particular issue that must be taken into account using those fibers is that the layers deposition is not uniform: the desired thickness of layers (20 nm Ti + 40 nm Au) can be considered only at the two opposite sides of the circular section. This can lead to some differences between the experimental result and theoretical study because the latter doesn't take this issue into account.

Another problem that can lead to some experimental unexpected behavior is that the thin gold layer can be affected by manual operations due to the usage of the fiber in laboratory (such as manual cleaning of the fiber after the conclusion of an experiment).

The first set-up is realised with “laboratory instruments” to test the fibers, evaluate the refractive index detection range, and, overall, have a background to understand if the low cost solution implemented in the following are feasible for the scope.

The set-up is a transmission configuration based on the wavelength interrogation method, with a broadband light and a spectrum analyser.

- The broadband light is provided by a Thorlabs fiber-coupled LED (MBB1F1 [12], Fig. 3.1b), that provides at least 0.8 mW in the range 470 - 850 nm, driven by the T-Cube LED Driver by Thorlabs (LEDD1B [13], Fig. 3.1a).
- The spectrometer, which is connected to the other end of the sensing fiber, is the AvaSpec-3648 [14], Fig. 3.1d.
- Both ends of the bare fiber are connected to the instruments with a Thorlabs Universal Bare Fiber Terminator (BFT1 [15], Fig. 3.1c, left) equipped with an SMA905 multimode connector (B10440A [16], Fig. 3.1c, right).



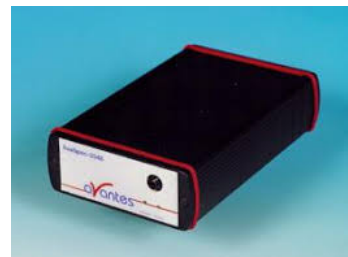
(a) Thorlabs T-Cube LED Driver (LEDD1B [13]).



(b) Thorlabs fiber-coupled LED (MBB1F1 [12]).



(c) Thorlabs Universal Bare Fiber Terminator (BFT1) and SMA905 multimode connector (B10440A [15,16]).



(d) AvaSpec-3648 fiber optic spectrometer [14].

Figure 3.1: Set-up components.

The spectrum analyser is connected to the PC allowing to see how the spectrum changes and to save the acquired spectra. The sensing fiber is placed in a plastic plate and fixed with a tape; the set-up can be seen in Fig. 3.2.



Figure 3.2: Set-up overview, wavelength interrogation.

## 3.2 Experimental tests

### Test with water and alcohol

The first test is performed with solutions of water and alcohol in different concentrations in order to understand how to manage the spectrum acquired to have significant results. The volumes of the solute and solvent, in all the tests, are measured with a 10 mL syringe, with accuracy 0.1 mL.

During the test several spectra are acquired (Fig. 3.3):

- Reference with a patch cord; used to acquire the effective spectrum of the LED;
- Reference of the SPR fiber in air;
- Spectrum of the SPR fiber immersed in 70 mL of water;
- Spectrum of the SPR fiber immersed in solution of 70 mL of water and alcohol (10 mL, 20 mL, 30 mL, 40 mL and 50 mL);

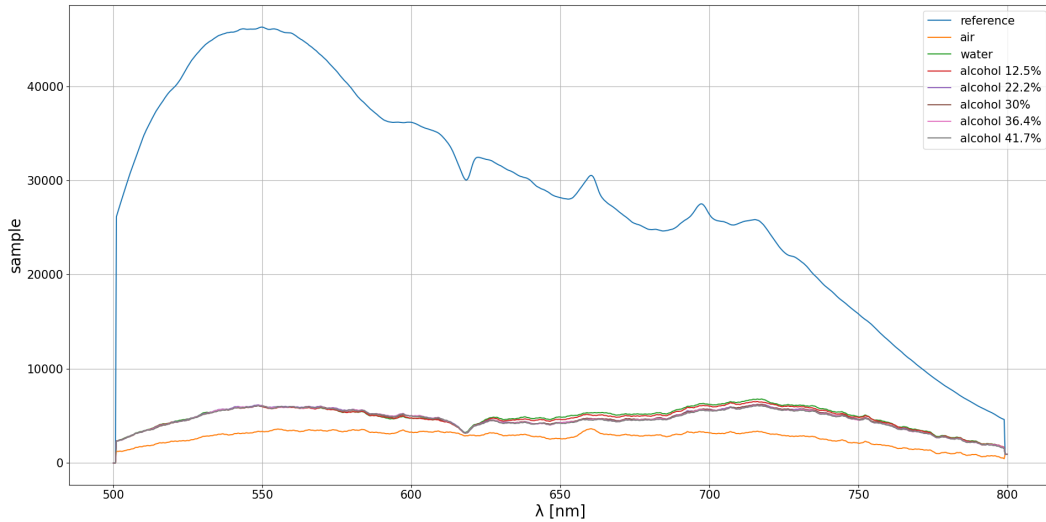


Figure 3.3: Acquired spectra, test with water and alcohol.

In order to remove the LED and system noises all the spectra with water and water-alcohol are normalized, in a first time with respect to the patch cord reface and then to the air reference. The second choice is made in order to reduce the noise and the contribution of the SPR fiber itself and the connectors.

As it can be seen from Fig. 3.4 all the curves, as expected, present a shift: the centre of the dip is moving to the right part of the spectrum (higher wavelength) as the concentration of alcohol increases.

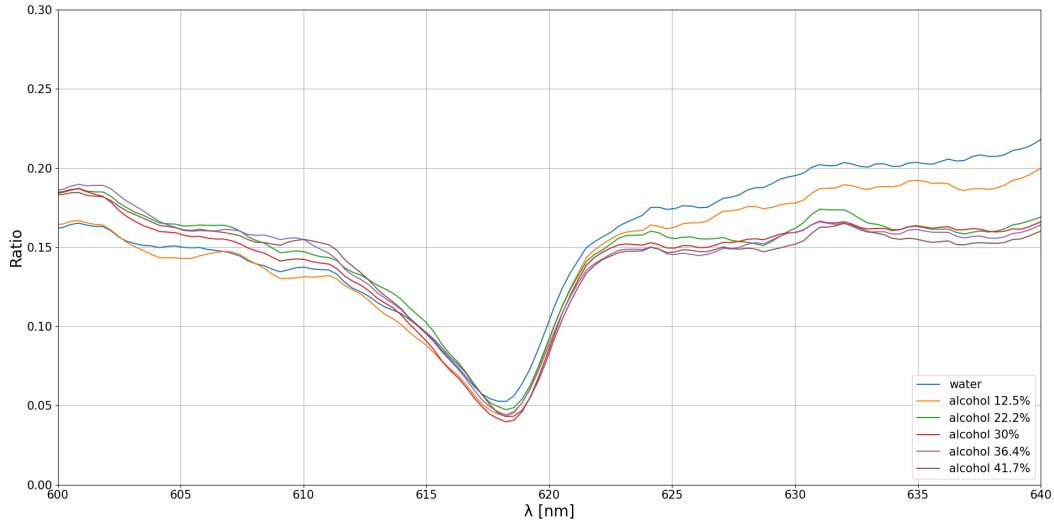


Figure 3.4: Normalized spectra with respect to air reference, test with water and alcohol.

### Test with water and salt

Another test is performed using a solution of water and salt. Even in this case the procedure is the same and in Fig. 3.5 it can be clearly seen the red shift at the increase of the the salinity (and so the refractive index). The two measures are performed to evaluate the best procedure to carry on the tests and to analyze the data acquired.

As already said, from the original spectrum is really difficult to detect the presence of the SPR dip, mainly because the spectrum of the LED is not so smooth and presents some dips and peaks. To remove the contribution of the LED the best solution is to take into account not the original acquired spectrum but the ratio between the original one and the reference acquired in air. The ratio can also be done with the reference taken with the patch cord but presents a lot of noise due to the contribution of the sensitive region of the SPR fiber that is not present into the patch cord.

Another issue to solve before carrying on other tests is the following: with the software of the spectrometer is not possible to acquire multiple spectrum automatically. Without this possibility it is impossible to perform measures on the stability of the system. A solution of this problem is found implementing a software in LabVIEW that acquires the spectra from the spectrometer and saves them on a *.txt* file after a little processing.

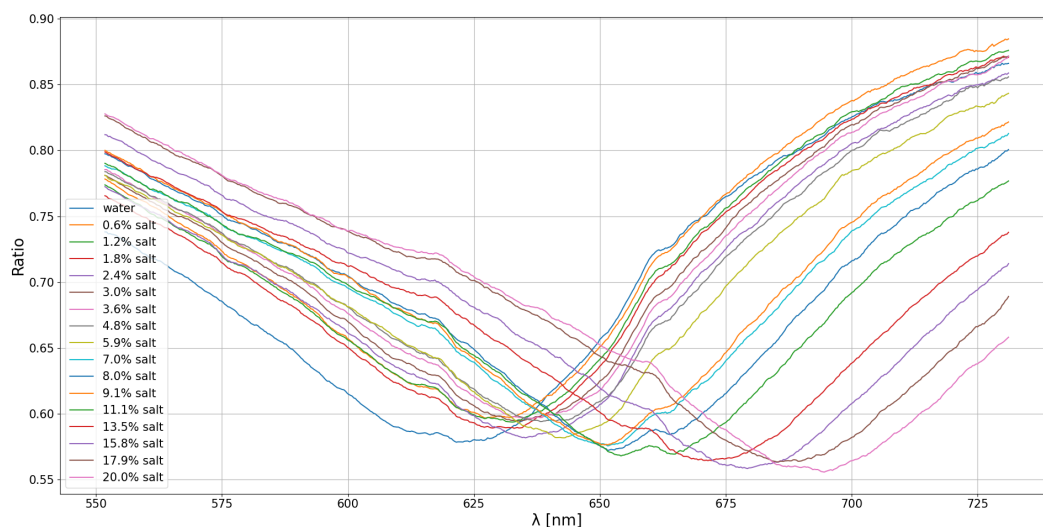


Figure 3.5: Normalized spectra with respect to air reference, test with water and salt.

The processing performed by LabVIEW is the following:

- It reduces the acquired spectra to a limited range selectable by the user (for this application the interval 500 - 800 nm is a good choice), considering that entire spectrum spans from 200 nm to 900 nm.
- It saves a reference spectra used to perform the ratio of the following acquisitions.
- It performs and saves the ratio between the current acquisition and the reference spectra.
- It saves a .txt file that contains all the wavelength values of the dip of the spectrum.
- The software allows the user to select also the interval between two consecutive acquisitions.

This acquisition system has been used to perform some tests: the main issues are presented in the following and it's shown how they have been solved.

### 3.2.1 First test

The test is performed again with a solution of water and alcohol, this because the salt needs a longer time to dissolve, being less suitable for experimental purposes. In Fig. 3.6 the acquired data are reported. As explained before the LabVIEWs software saves directly the ratio between the reference spectra and the current acquisition. The acquisition is performed with LabVIEW, selecting a proper interval between two consecutive acquisitions that allows the change of the concentration of the solution (1 min circa).

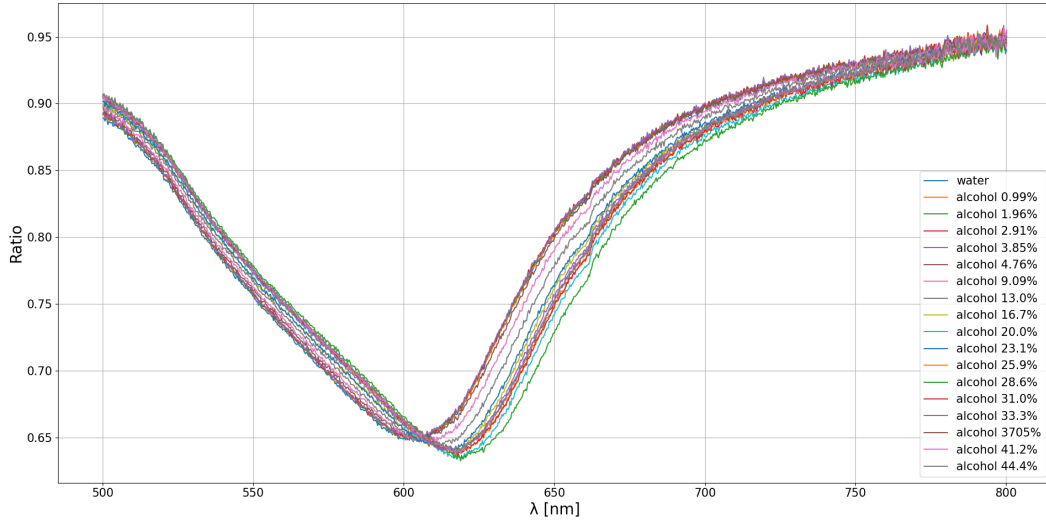
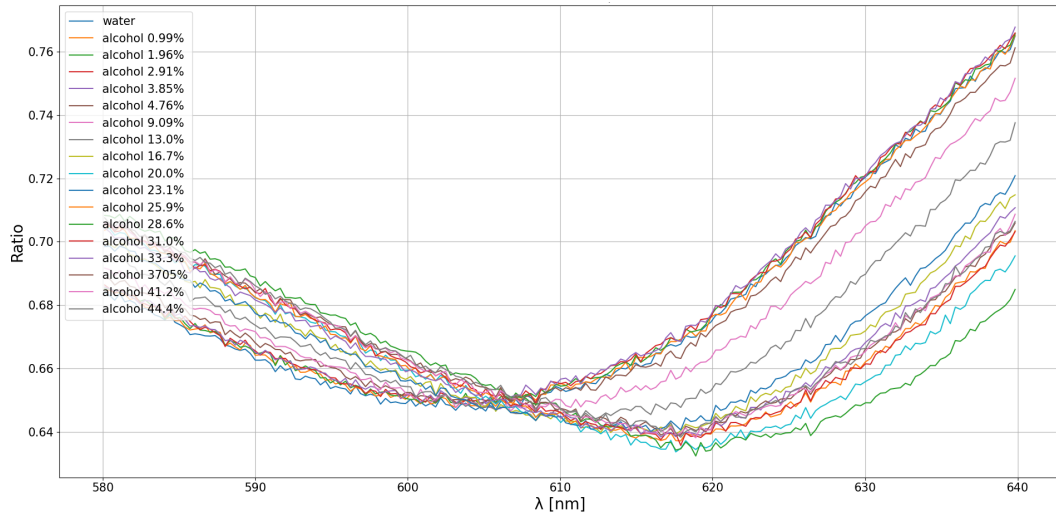


Figure 3.6: Normalized spectra with respect to air reference, test 1.

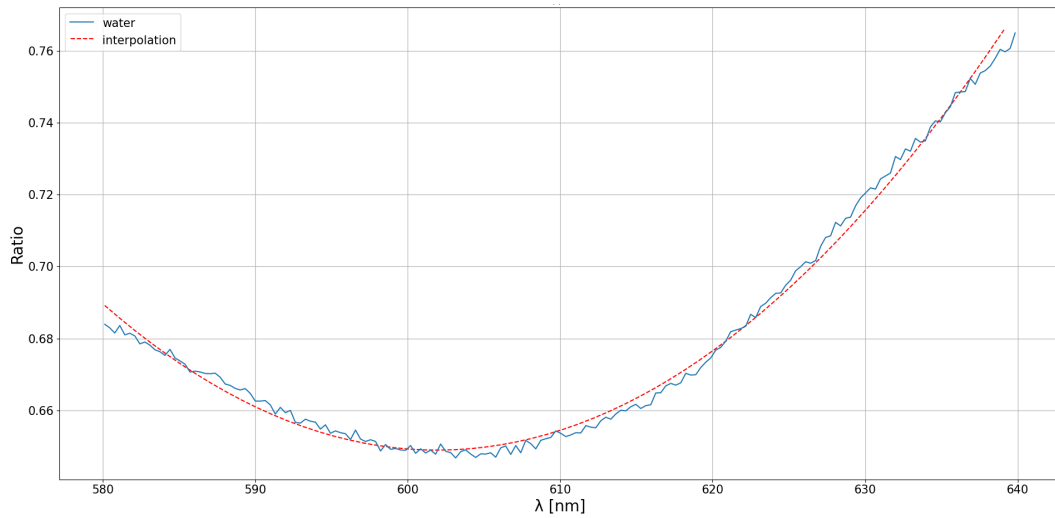
In Fig. 3.7a a more detailed image of the acquired data is presented: the shift of the dip as the reactive index changes is clearly detectable, but it is also clear how noisy the spectra are. The noise in this case causes a real damage on the analysis of data because the addition of the noise can move the point of minimum, thus reducing the accuracy of refractive index measurements. A possible solution for this issue is represented by the interpolation: the SPR's, in a small interval around the dip, seems to perfectly follow a parabolic behaviour (Fig. 3.7b). This simplifies a lot the problem because just adding a parabolic interpolation allows to detect clearly the minimum point.

### 3.2.2 Overnight stability

The possibility to acquire data continuously allows to study the stability of the sensor. The acquisition is performed overnight (for 17 hours), saving the spectrum every 10 seconds. The sample used is demineralised water since tap water can present a non stable concentration of solutes in response to the evaporation (the plate is not covered). Demineralised water instead, even in case of evaporation, guarantees a constant, null, concentration of solutes. Due to the extremely large number of spectra acquired, the plot of each one cannot be understood. For this reason only the wavelength of each dip is reported in Fig. 3.8(blue line): as it can be seen the wavelength of the minimum varies a lot, even if the sample is always the same and a constant behaviour is expected. This is due to the noise present in each acquisition, as already highlighted before. Some manipulation has been done in order to overcome this problem.



(a) Normalized spectra with respect to air reference.



(b) Normalized spectra of water with respect to air reference with parabolic interpolation.

Figure 3.7: Normalized spectra with respect to air reference, test 1.

As a first try a filter is applied, showing some improvement in the reduction of fluctuations (Fig. 3.8, orange line). The filter is a FIR digital filter designed in [17] with the following characteristics:

- sampling frequency: 100 Hz
- 0 Hz - 1.5 Hz
  - gain = 1
  - desired ripple = 0.2 dB

- actual ripple = 0.0308 dB
- 5 Hz - 50 Hz
  - gain = 0
  - desired attenuation = -60 dB
  - actual attenuation = -73.6143 dB

A second try with another similar FIR filter has been done. This filter is designed by [18] with:

- Sample rate = 100
- ripple = 60 dB
- Cut-off frequency = 1 Hz

The result is presented in (Fig.3.9, red line).

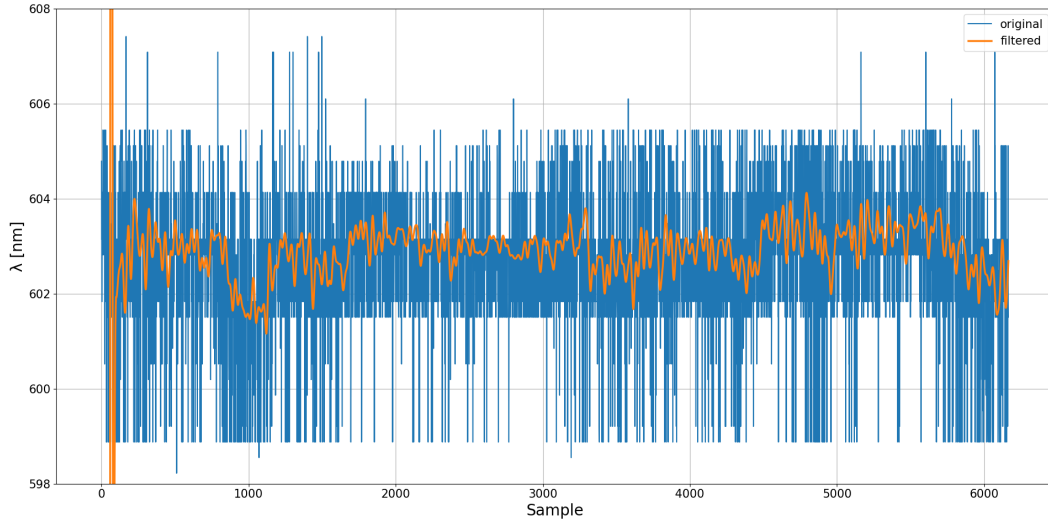


Figure 3.8: Wavelength of dips with filter 1, overnight stability.

Comparing the standard deviation after the two filters, 0.485 and 0.411 respectively, it is clear that the behaviour is quite similar, even if it is not a perfect solution due to the fact that the stability is not guaranteed. As already said the fluctuations are due to the presence of noise on the spectrum that changes the minimum point of the dip.

In Fig. 3.10 is clearly visible that the actual minimum is at 605 nm while the real one is around 602 nm. To overcome this issue the best solution is to interpolate all the spectra, in a small interval around the dip, with a parabola and consider the minimum of the interpolated curve instead of the acquired spectrum. This procedure increases the complexity of the analysis but allows to obtain significant results even in presence of noise. As reported in Fig. 3.11, applying the interpolation at each spectra the wavelength of the minimum is quite constant, showing that the sensor is really stable and reliable.

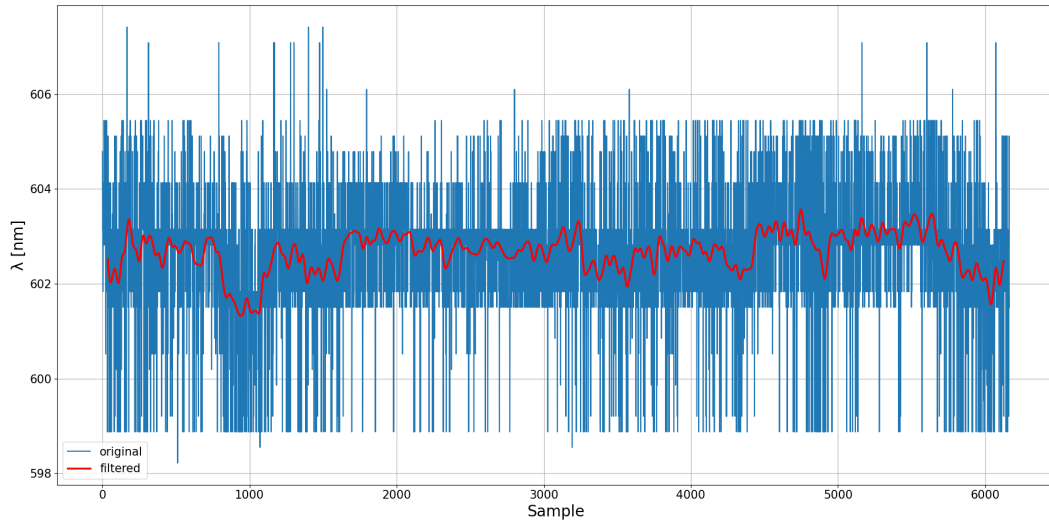


Figure 3.9: Wavelength of dips with filter 2, overnight stability.

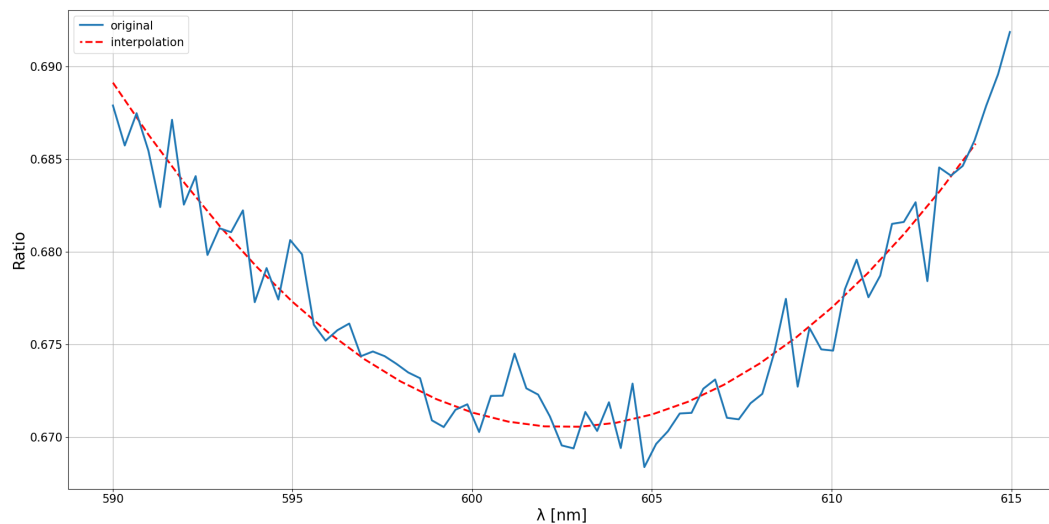


Figure 3.10: Normalized spectra with respect to air reference with interpolation, overnight stability.

### 3.2.3 Second test

Even in this case the test is performed with water and alcohol, acquiring multiple spectra for each concentration, in particular the acquisition is performed every 200 ms and the concentration is varied approximately every minute, in order to allow the solution to become quite homogeneous. Fig. 3.12 shows the position of the minimum of each dip: the blue vertical lines represent the separation between different concentration of alcohol

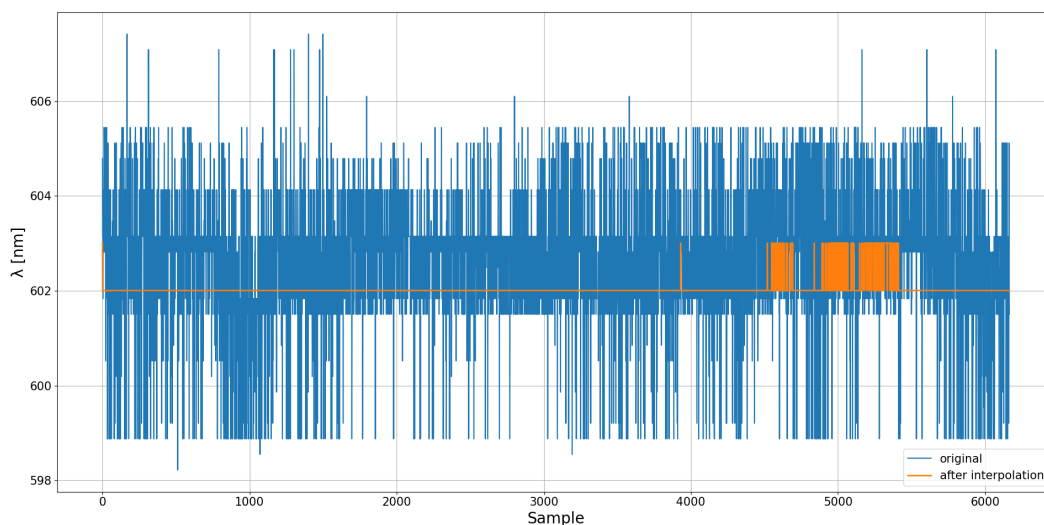


Figure 3.11: Wavelength of dips after interpolation, overnight stability.

in the solution. At a first sight a step behaviour can be identified, even with a lot of noise and some peaks. The noise allows to see some steps but, mainly in correspondence of

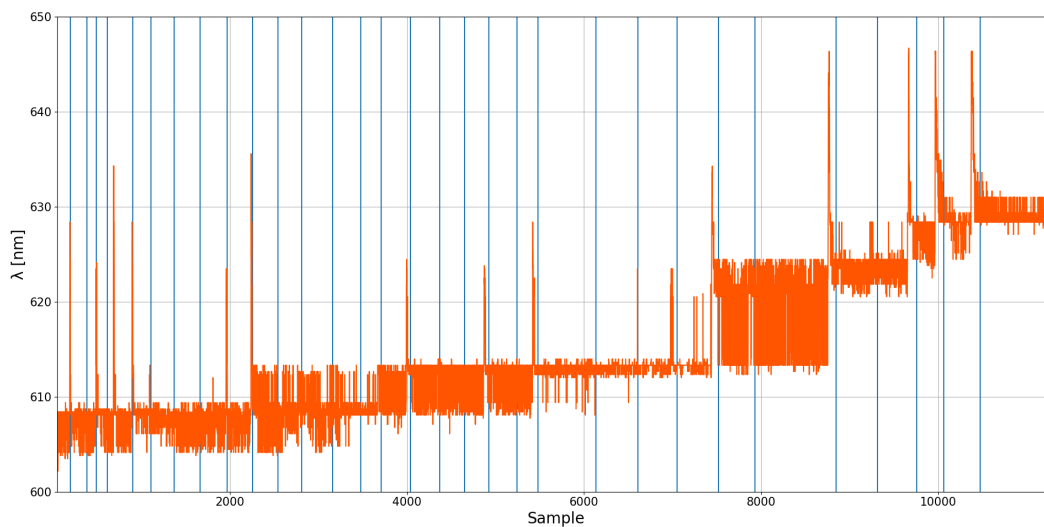


Figure 3.12: Wavelength of dips, test 2.

lower concentrations of alcohol (in the left side of the graph), reduces the sensibility of the system: the variations due to the changes in refractive index are covered by the noise's fluctuations. Even in this case the data are manipulated to reduce the influence of the noise. As a first step is applied the interpolation with a parabola in the interval  $\pm 12$  nm with respect to the minimum founded with the original spectrum (the interval is chosen

to allow the best correspondence between the interpolation and the original spectrum). In Fig. 3.13, red line is reported the position of the minimum after the interpolation.

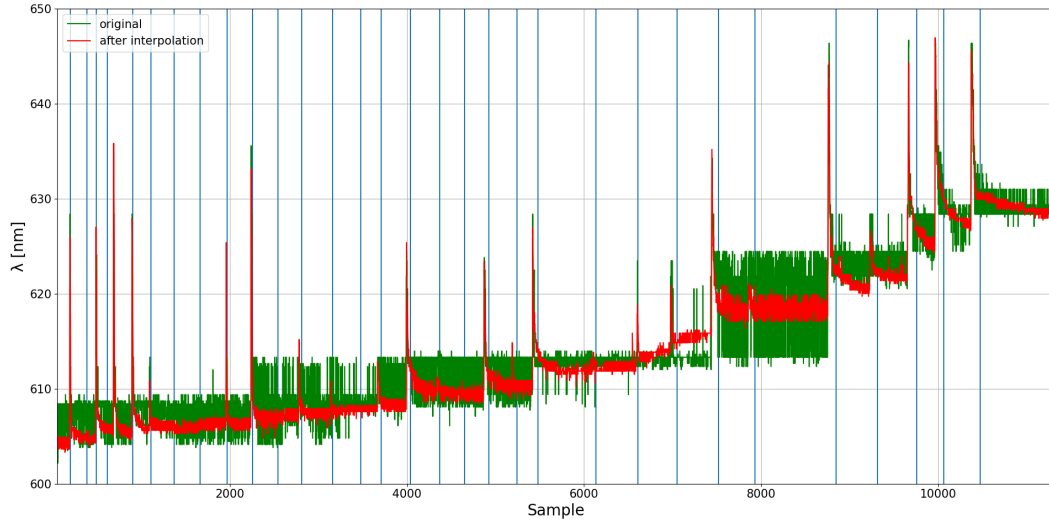


Figure 3.13: Wavelength of dips after interpolation, test 2.

Since the result is still a bit noisy, is performed also the filtering (with the second filter presented before). The result is presented in Fig. 3.14: the noise is removed, obtaining a sequence of steps. The difference in the height of steps is due to the fact that, as reported in Fig. 3.12, the quantity of alcohol added in each step is larger in the right side of the graph, leading to higher differences of RI and so higher wavelength shift. The presence of

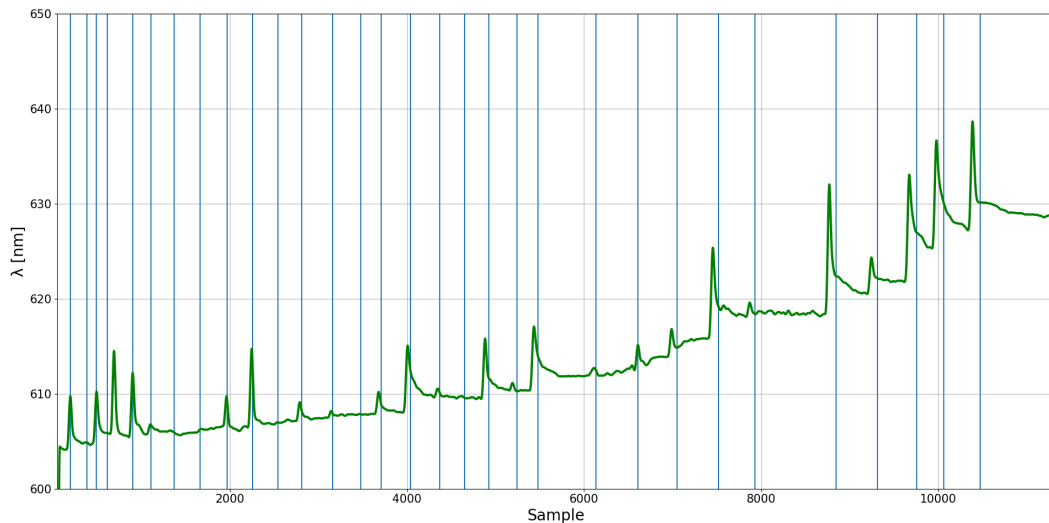


Figure 3.14: Wavelength of dips after interpolation and filtering, test 2.

peaks at each step is due to the manual process concentration variation, that is performed by manually adding a small quantity of alcohol directly in the preexistent solution with a syringe. This procedure if performed too near to the SPR sensing region causes a violent change in the SPR's resonance wavelength, partly due to the strain caused by the flow of the liquid and partly due to the fact that locally, for a moment, the solution is completely formed by alcohol, causing a huge increase of the RI. In Fig. 3.15 is reported a graph that shows the average value of wavelength for each alcohol concentration. The plot reports the value of wavelength in function of the refractive index: the value of the refractive index starting from the alcohol concentration is obtained with the procedure explained in Section 3.3. It is interesting to notice that the relation between wavelength and refractive index is almost linear, allowing a simple detection of the refractive index starting from the measured wavelength.

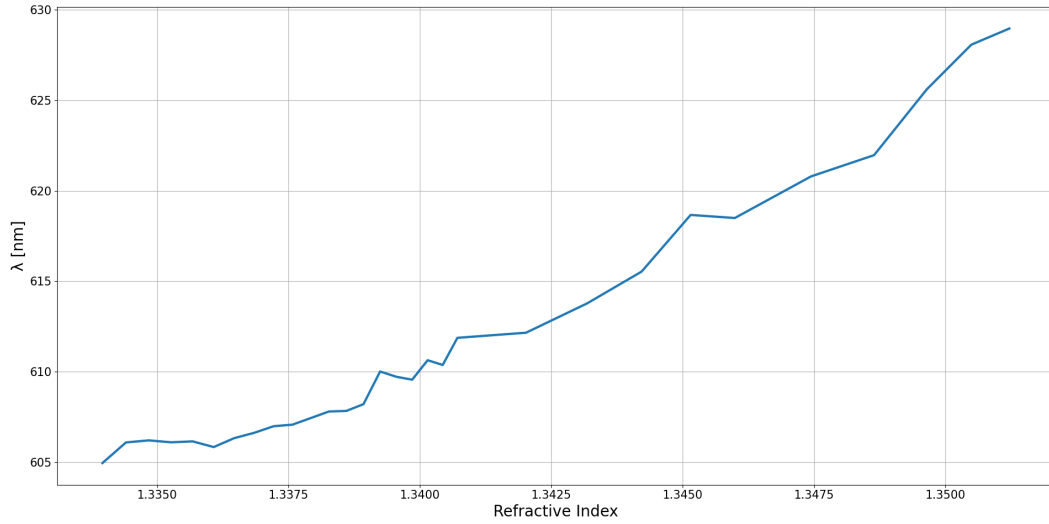


Figure 3.15: Average value of wavelength for each alcohol concentration, test 2.

### 3.2.4 Third test

Another test, very similar to the previous one, is carried on in order to understand if the repeatability is good and to validate the theory expressed before about the origin of the peaks. During the test the alcohol used to change the concentration of the solution is again injected with the syringe but paying attention to inject it in a region far from the sensing region. As it can be seen in Fig. 3.16 and better in Fig. 3.17 and Fig. 3.18, with this procedure the peaks are reduced and the steps are rather horizontal. As before Fig. 3.16 represents the wavelength of each SPR's dip, each concentration interval is again separated by the vertical line. In Fig. 3.17 is reported the wavelength position of each minimum point after the interpolation of each spectrum with a parabola in the interval  $\pm 12$  nm from the centre. Fig. 3.18 reports the minimum of the interpolated functions filtered with the FIR filter. In Fig. 3.19 is reported the average wavelength of

each alcohol concentration. Also in this case the plot reports the value of wavelength in function of the refractive index: the value of the refractive index starting from the alcohol concentration is obtained with the procedure explained in Section 3.3. also in this case is interesting to notice that the relation between wavelength and refractive index is almost linear.

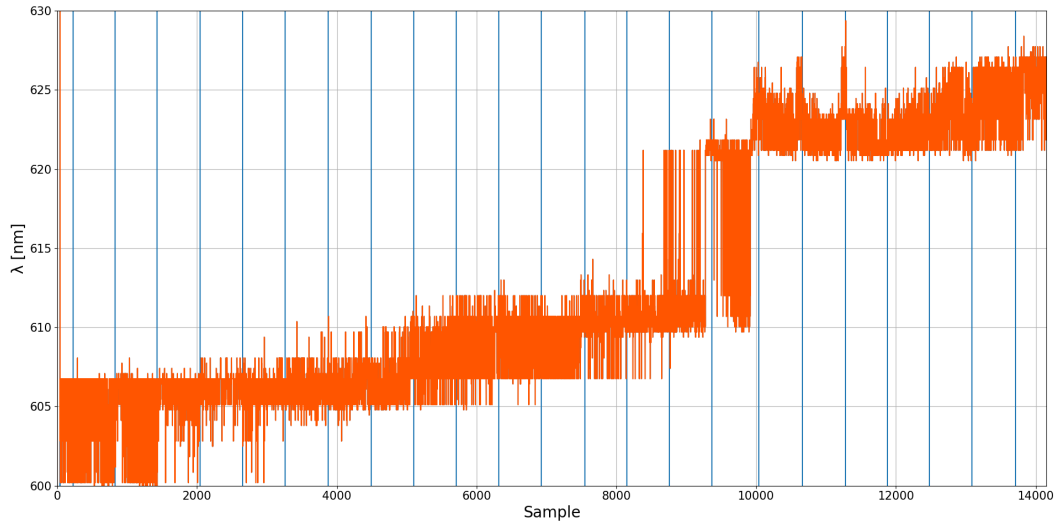


Figure 3.16: Wavelength of dips, test 3.

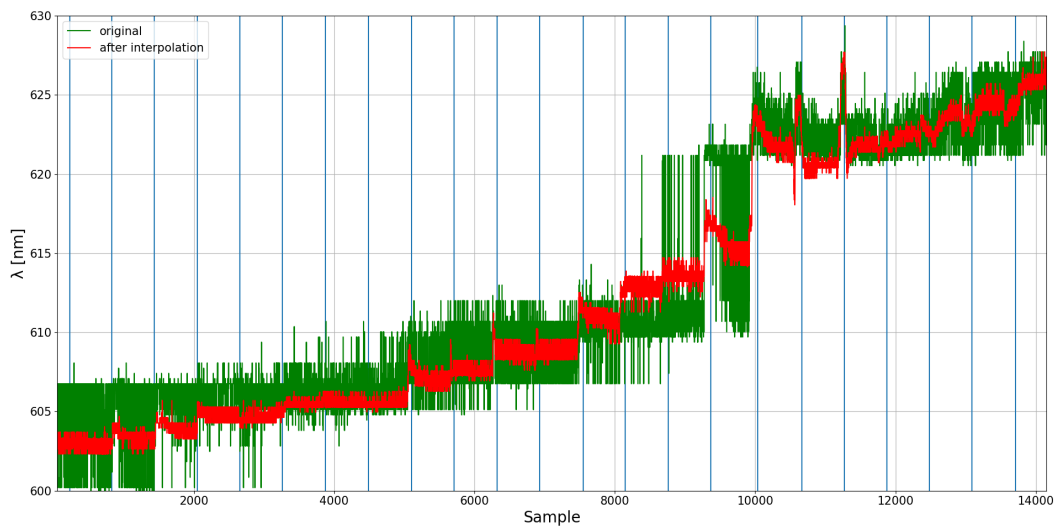


Figure 3.17: Wavelength of dips with interpolation, test 3.

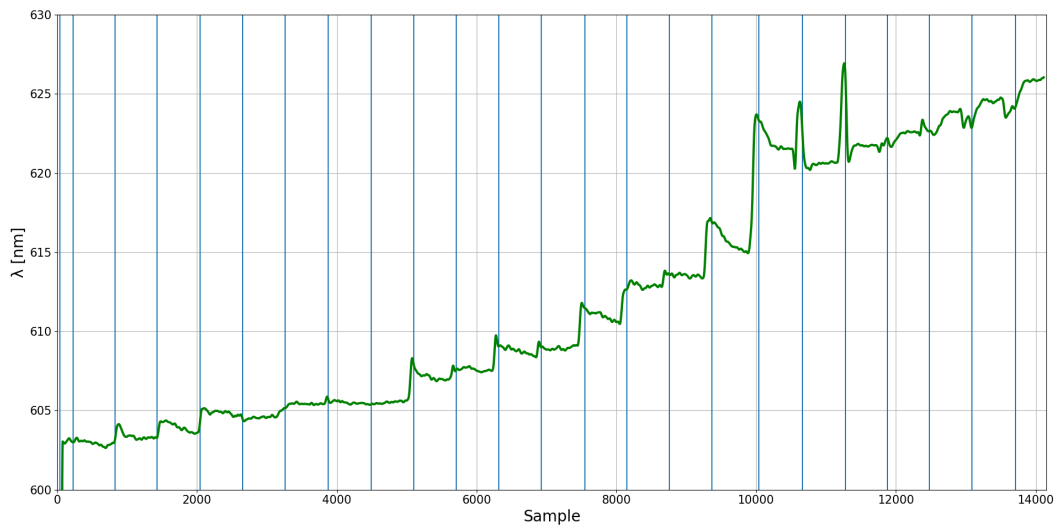


Figure 3.18: Wavelength of dips after interpolation and filtering, test 3.

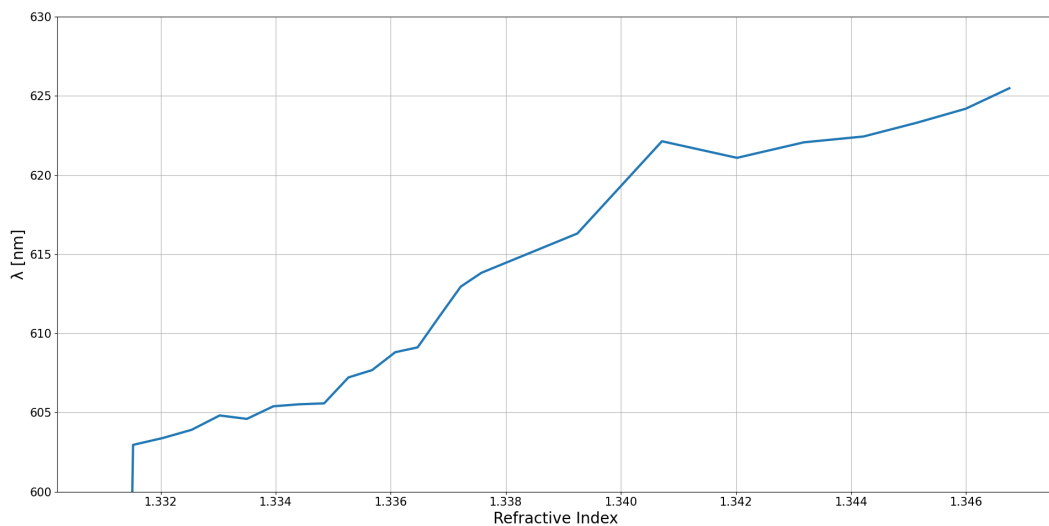


Figure 3.19: Average value of wavelength for each alcohol concentration, test 3.

### 3.3 Refractive index of a solution

The results obtained until now correlate the wavelength shift to the concentration of the water-alcohol solution, without considering the refractive index. The advantage of using alcohol instead of salt, in addition to the velocity of mixing already mentioned, is the fact that exists a formula (Eq. 3.1 [19]) that, given some parameters, allows to compare the resultant refractive index of a solution of two liquids.

The needed parameters are:

- Refractive index of solvent and solute ( $n_s(\lambda)$  and  $n_a(\lambda)$ );
- Density of solvent and solute ( $\rho_s$  and  $\rho_a$ );
- Mass fraction of solvent and solute ( $w_s$  and  $w_a$ ).

$$\frac{n^2(\lambda) - 1}{n^2(\lambda) + 2} = \frac{n_a^2(\lambda) - 1}{n_a^2(\lambda) + 2} \cdot \frac{\rho}{\rho_a} \cdot w_a + \frac{n_s^2(\lambda) - 1}{n_s^2(\lambda) + 2} \cdot \frac{\rho}{\rho_s} \cdot w_s \quad (3.1)$$

The refractive index of water  $n_a^2(\lambda)$  is computed with Eq. 3.2 [20]:

$$\frac{n_a^2(\lambda) - 1}{n_a^2(\lambda) + 2} \cdot \frac{1}{\rho^*} = a_0 + a_1\rho^* + a_2T^* + a_3\lambda^{*2}T^* + \frac{a_4}{\lambda^{*2}} + \frac{a_5}{\lambda^{*2} - \lambda_{UV}^{*2}} + \frac{a_6}{\lambda^{*2} - \lambda_{IR}^{*2}} + a_7\rho^{*2} \quad (3.2)$$

Where:

$$\begin{aligned} \rho^* &= \rho/\rho_0 & \rho_0 &= 1000\text{kg}/\text{m}^3 \\ \lambda^* &= \lambda/\lambda_0 & \lambda_0 &= 0.589\mu\text{m} \\ T^* &= T/T_0 & T_0 &= 273.15\text{K} \end{aligned}$$

In Eq. 3.2 the refractive index is computed in function of wavelength ( $\lambda$ ), temperature (T) and density ( $\rho$ ) but for this application the contribution of the temperature and density are not relevant, so the value are kept constant. The values of the coefficient  $a_0$  to  $a_7$  and of the effective infrared ( $\lambda_{IR}^*$ ) and ultraviolet ( $\lambda_{UV}^*$ ) resonances are listed in [20].

The refractive index of alcohol  $n_s^2(\lambda)$  is computed with the Sellmeier equation (Eq. 3.3 [21]):

$$n^2 = 1 + \frac{B \cdot \lambda^2}{\lambda^2 - C} + \frac{D \cdot \lambda^2}{\lambda^2 - E} \quad (3.3)$$

Using, in the case of alcohol (Ethanol),

$$\begin{aligned} B &= 0.0165 \pm 0.0002 \\ C &= 9.08 \pm 0.02 \\ D &= 0.8268 \pm 0.0001 \\ E &= 0.01039 \pm 0.00001 \end{aligned}$$

The dispersion relations for solutions with different percentages of water and alcohol are presented in Fig. 3.20. Considering that the working interval in this specific application is around 615-650 nm, the refractive index can be considered quite constant in this interval. In Fig. 3.21 is reported the refractive index of the water-alcohol solution in function of the percentage of alcohol, considering, for each concentration the mean value in the interval 615-650 nm.

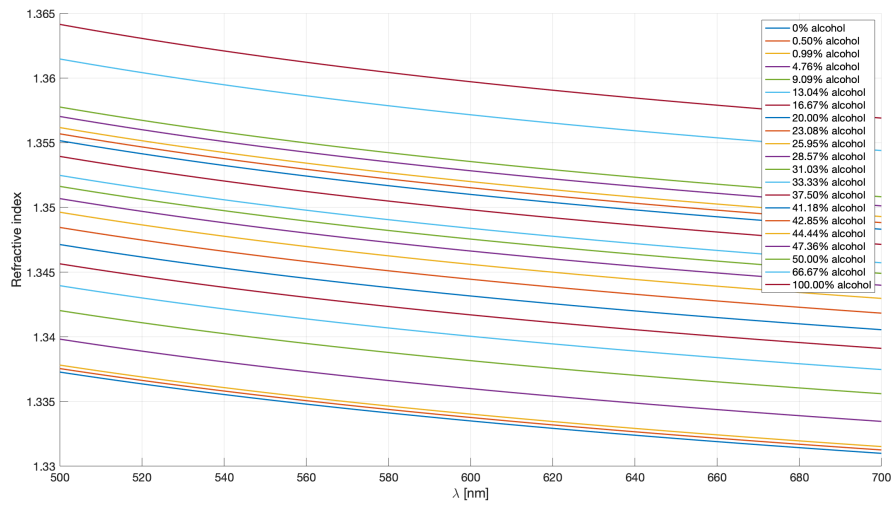


Figure 3.20: Refractive index of different water-alcohol solutions in function of wavelength.

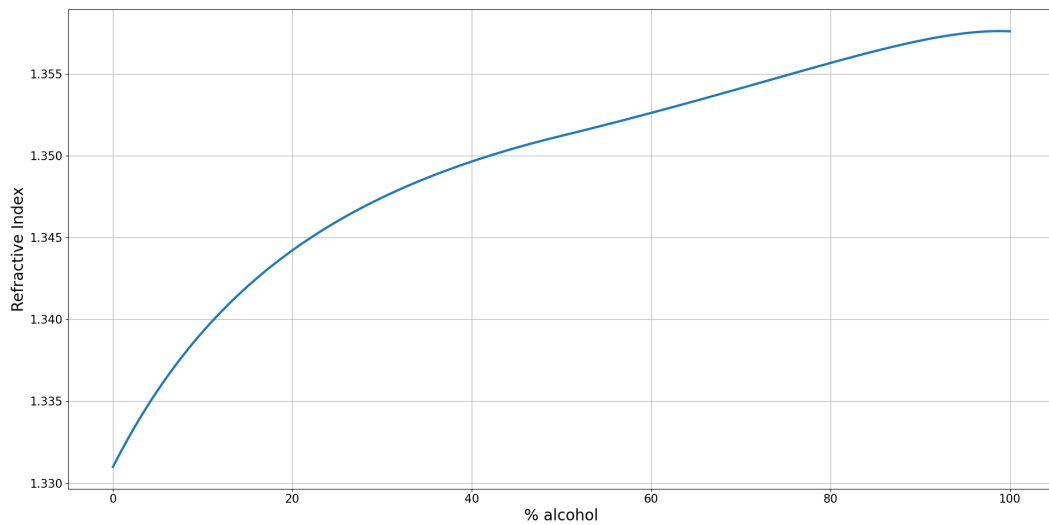


Figure 3.21: Refractive index of water-alcohol solution in function of alcohol concentration.

### 3.4 Real measurements

Since some tests have been performed with water-alcohol solution is interesting to try some tests with real water samples.

### 3.4.1 Test 1

The first test is done acquiring three different spectra for tap water, distilled water and contaminated water. The contaminated water is done on purpose using tap water and cat faeces. In Fig. 3.22 is reported the spectrum acquired directly from the Avantes software, without any processing. The acquisition is not performed with LabVIEW, so just one spectrum for each condition is present.

In Fig. 3.22 four spectra are reported: three correspond to the water samples while the fourth one is the reference in air, used to compute the ratio to remove the noise and highlight the SPR dip. The result of the ratio is presented in Fig. 3.23. To better

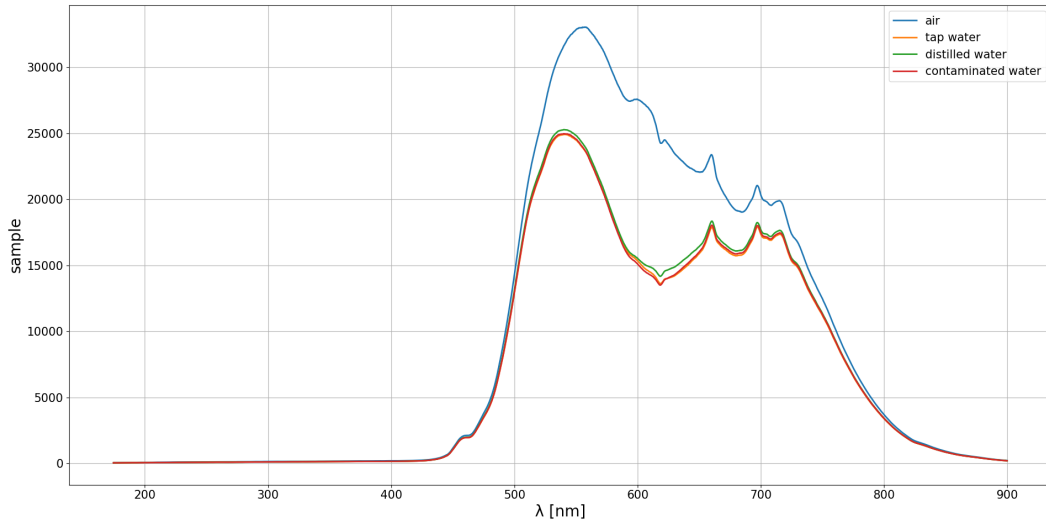


Figure 3.22: Acquired spectra, test with different water samples.

highlight the behaviour of the dip in the three cases in Fig. 3.24 is reported an enlarged version of the minimum of the dip. From the theory the distilled water has the lowest refractive index, so the lowest resonance wavelength, followed by tap water and then the contaminated water. In Fig. 3.24, and better in Tab. 3.1, can be noticed that the distilled water and the tap water follows the expected behaviour, while the contaminated water has a resonance wavelength in the middle of the other two while from theory must have the larger wavelength shift. In Tab. 3.1 are reported two values for each sample: the first one is the wavelength of the minimum of the actual acquired spectra (the ones reported in Fig. 3.23) while the second value represents the wavelength of the minimum of the parabola interpolated to the actual spectrum (dashed lines in Fig. 3.24). The difference between the expected behaviour and the experimental one is due to two main factors: The lack of temperature compensation, since the SPR shift is affected both by refractive index and temperature changes. The fact that the fiber is connected to the light source and to the spectrometer with mobile connectors that does not allow to have perfectly repeatable measures. Every time the liquid is changed into the plate all the setup is moved and so the measurements cannot be considered repeatable.

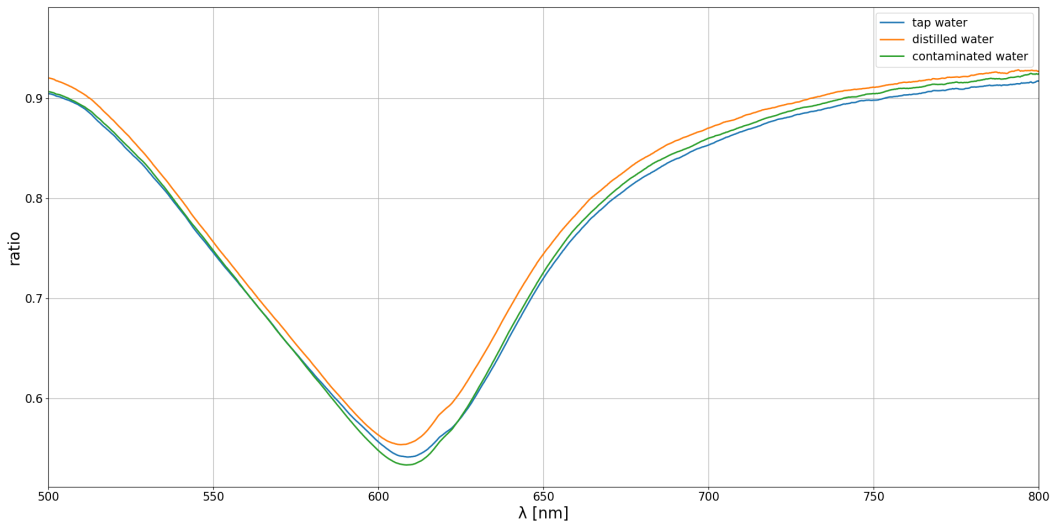


Figure 3.23: Normalized spectra with respect to air reference, test with different water samples.

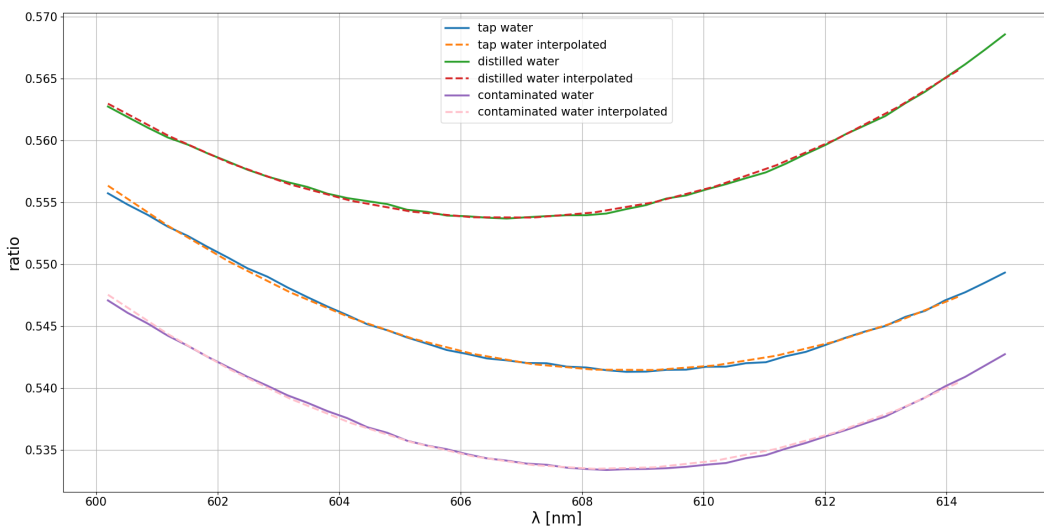


Figure 3.24: Normalized spectra with respect to air reference and interpolation, test with different water samples.

### 3.4.2 Test 2

A second try has been done using again distilled water, tap water and contaminated water. In addition three other samples have been considered: the contaminated water has been sanitised with UVC light in different quantities (Tab. 3.2). In Fig. 3.25 are reported all the acquired spectra (also the reference in air used to compute the ratio).

Sample	$\lambda_{SPR}$	$\lambda_{SPR}$
Distilled water	608.727 nm	607.193 nm
Tap water	606.758 nm	609.193 nm
Contaminated water	608.399 nm	608.193 nm

Table 3.1: Wavelength of the minimum of the actual acquired spectra and the interpolated one.

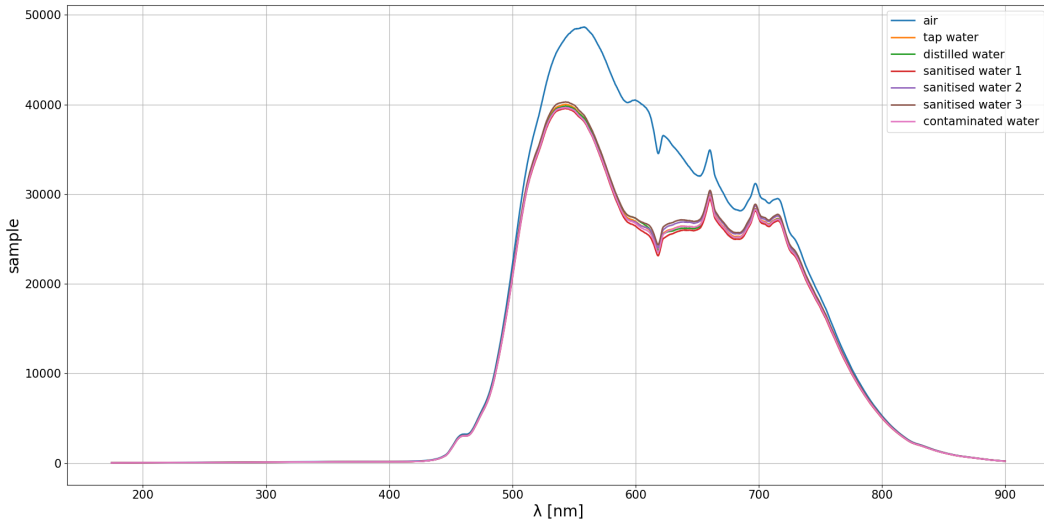


Figure 3.25: Acquired spectra, test with different water samples.

In Fig. 3.26 is reported the result of the ratio between the reference in air and the other spectra. In Fig. 3.27 and better in Tab. 3.3 is possible to see the shift between the various curves. Again the experimental measures are not consistent with the theory since the set up does not allow to perform measurements in which the liquid is changed after every measure. The set up work properly only if the concentration of the solute is changed gradually without removing all the liquid every time.

Sample	Irradiance	Height	Time
1	9 mW/cm <sup>2</sup>	1.8 cm	1 s
2	4.9 mW/cm <sup>2</sup>	2.5 cm	2 s
3	1.26 mW/cm <sup>2</sup>	5 cm	8 s

Table 3.2: UVC quantities for sanitation.

Sample	$\lambda_{SPR}$	$\lambda_{SPR}$
Distilled water	608.071 nm	606.833 nm
Tap water	604.461 nm	605.373 nm
Contaminated water	606.430 nm	605.673 nm
Sanitised water 1	605.117 nm	604.433 nm
Sanitised water 2	607.414 nm	606.463 nm
Sanitised water 2	603.804 nm	604.463 nm

Table 3.3: Wavelength of the minimum of the actual acquired spectra and the interpolated one.

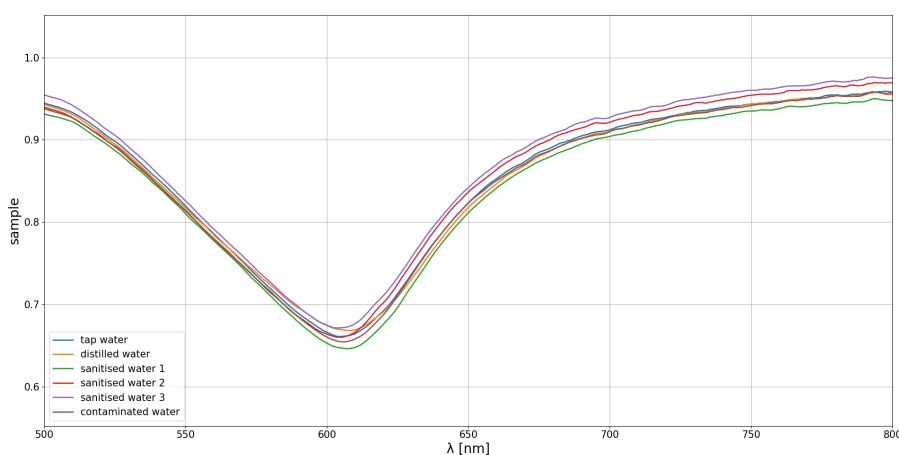


Figure 3.26: Normalized spectra with respect to air reference, test with different water samples.

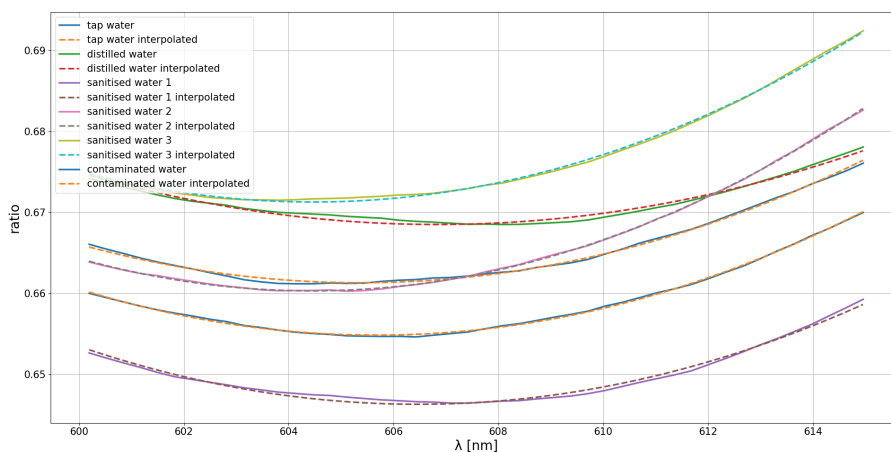


Figure 3.27: Normalized spectra with respect to air reference and interpolation, test with different water samples.

## Chapter 4

# Intensity interrogation

Since the set-up needed for the wavelength interrogation is bulky, really costly and has some other drawbacks like the noise injected by the LED and the huge quantity of data to acquire (each spectrum is acquired in a single *.txt* file), it is suitable for a laboratory and experimental usage only, but not for a low cost and accessible application. An alternative that can lead to a device more compact and less expensive is to implement the intensity interrogation method as it only needs a power meter and a LED in the visible with a small wavelength range. To implement correctly this method a deep knowledge of the SPR's behavior is needed, in order to know approximately the achievable sensibility and to choose the correct LED.

### 4.1 Implementation of the theoretical model

The sensor's behavior can be understood by analysing the reflection coefficient at the glass-metal interface. This model simplifies the problem modeling the fiber as a 2D slab structure made by three layers, with the first and the last having infinite extension (Fig. 4.1).

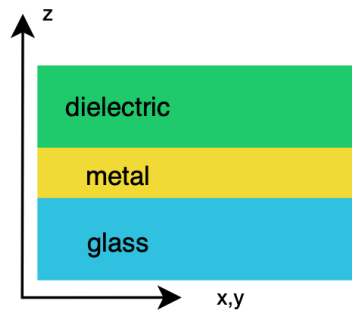


Figure 4.1: 2D slab structure.

The gold layer has a 50 nm thickness while the titanium layer is neglected, since it does

not affect the overall behavior. Any layer can be characterised as a piece of transmission line and described with its own propagation constant  $k$  and its characteristic impedance  $Z_\infty$  [22, 23].

As already said the SPR occurs only in presence of p-polarized light (TM, where the polarisation is parallel to the plane of the interface), hence the model is solved only for TM incident light.

The first step is to compute the refractive index of each one of the three layers:

- Prism ( $n_p$ ): Sellmaier equation Eq. 4.1 [24]

$$n_p^2 = 1 + \frac{A \cdot \lambda^2}{\lambda^2 - B} + \frac{C \cdot \lambda^2}{\lambda^2 - D} + \frac{E \cdot \lambda^2}{\lambda^2 - F} \quad (4.1)$$

with coefficients

$$\begin{aligned} A &= 0.6961663 & B &= 0.0684043 \\ C &= 0.4079426 & D &= 0.1162414 \\ E &= 0.8974794 & F &= 9.896161 \end{aligned}$$

- Gold ( $n_g$ ):  $\varepsilon_g = -13 - 1.1j$ , knowing that  $n_g = \sqrt{\varepsilon_g}$
- Dielectric ( $n_d$ ): in case of water, alcohol or water-alcohol solution Eq. 3.2, Eq. 3.3 and Eq. 3.1 respectively.

The angle of incidence of the light is found by solving Eq. 2.3, obtaining Eq. 4.2:

$$\theta = \arcsin\left(\frac{1}{n_p} \cdot \sqrt{\frac{\varepsilon_g \cdot n_d^2}{\varepsilon_g + n_d^2}}\right) = 71.24^\circ \quad (4.2)$$

As said before, the refractive index variations due to the wavelength are not relevant in this application, since the working interval is limited. For this reason all the refractive indexes are computed considering only  $\lambda = 650$  nm.

Then the equivalent transmission line parameters must be computed, paying attention to use the propagation constant with negative imaginary part, for both gold (Eq. 4.3) and dielectric (Eq. 4.4):

$$k_g = k_0 \cdot \sqrt{\varepsilon_g - n_p^2 \cdot \sin(\theta)^2} \quad (4.3)$$

$$k_d = k_0 \cdot \sqrt{n_d^2 - n_p^2 \cdot \sin(\theta)^2} \quad (4.4)$$

where  $k_0 = 2\pi/\lambda$ . Also the characteristic impedance of each layer is computed, here the condition on the sign of the imaginary part is already satisfied since it's imposed on the propagation constant.

$$Z_p = \frac{1}{\cos(\theta) \cdot n_p} \quad (4.5)$$

$$Z_g = \frac{k_g}{\varepsilon_g} \quad (4.6)$$

$$Z_d = \frac{k_d}{n_d^2} \quad (4.7)$$

Once the characteristic impedances are computed the reflection coefficient in B can be computed and propagated in A- through the computation of  $Z$  in A. The impedance in the section B is equal to  $Z_d$  since the dielectric layer is considered with infinite length.

The first step is the computation of the transmission coefficient in the section B (Eq. 4.8):

$$\Gamma_B = \frac{Z_d - Z_g}{Z_d + Z_g} \quad (4.8)$$

Then the gamma has to be moved to section A+ (Eq. 4.9)

$$\Gamma_{A+} = \Gamma_B e^{-2jk_g d_g} \quad (4.9)$$

At this point the characteristic impedance in section A can be computed (Eq. 4.10), obtaining then, from Eq. 4.11, the reflectivity ( $R$ ) at the end of the transmission line and so at the glass-metal interface.

$$Z_A = Z_g \frac{1 + \Gamma_{A+}}{1 - \Gamma_{A+}} \quad (4.10)$$

$$R = |\Gamma_{A-}|^2 = \left| \frac{Z_A - Z_p}{Z_A + Z_p} \right|^2 \quad (4.11)$$

In Fig. 4.2 it is reported the behavior of the reflectivity using water as dielectric ( $n = 1.33$ ), while in Fig. 4.3 that in the case of water-alcohol solution with different concentrations.

It is interesting to notice in Fig. 4.2 that the wavelength at which we find the dip (652 nm) is quite different from the experimental value (602 nm (Fig. 3.11)); this is due to the fact that the model used here is a simplification of the real behavior of the sensor and that the metallic layer is considered only composed by gold without the titanium. The goal of this model is to understand if, with a generic single wavelength LED, it is possible to detect a meaningful variation in the refractive index of the medium in contact with the sensor. Therefore, the exact position of the dip is not necessary in this analysis. The only issue is on the choice of the best LED and the wavelength blue shift must be considered. It is also interesting to notice in Fig. 4.3 that the working interval of the SPR, at least in water-related applications, is limited approximately to 50 nm, as also noticed in the experimental tests. The fact that the working interval is constant through theory and experiments confirms that the wavelength shift is constant and that, considering the offset, it is possible to apply the theoretical model in practice.

Always in Fig. 4.3, it can also be noticed the intensity variation that occurs between two curves, suggesting that the intensity interrogation method can lead to good results.

In order to analyze in a deeper way the behavior of the interrogation method it is also necessary to simulate the contribution of the LED.

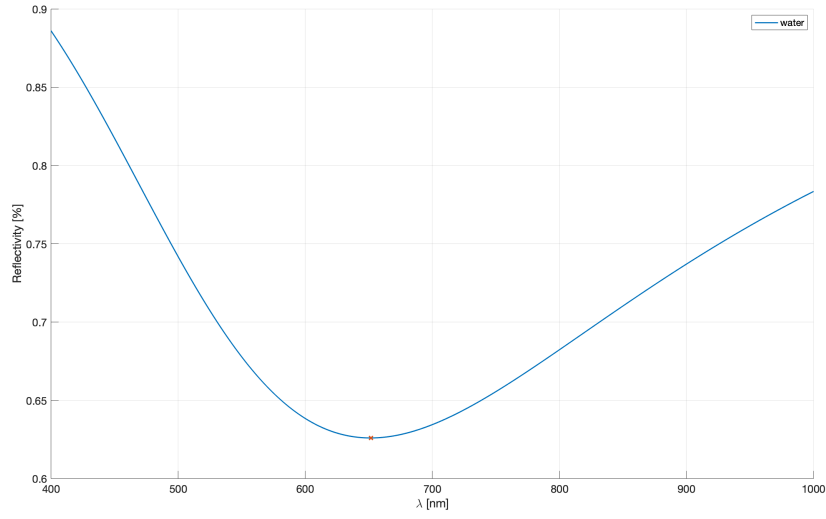


Figure 4.2: Reflectivity of the SPR sensor using water as dielectric ( $n = 1.33$ ).

The intensity interrogation method works evaluating the power at the output of the sensor. To simulate its behavior two things are necessary:

- The spectral response of the SPR sensor, computed above and reported in Fig. 4.3;
- The spectral response of the LED.

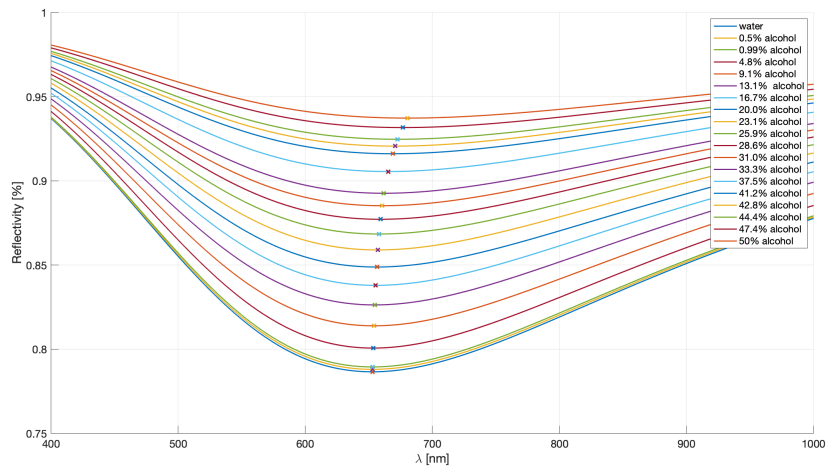


Figure 4.3: Reflectivity of the SPR sensor using different water-alcohol solutions as dielectric.

The spectral response of the LED is obtained from a data sheet of a real LED from Thorlabs [25]. Since the spectral response is not available for each LED sold by Thorlabs, the shape of the spectral response is assumed to be almost equal for each available LED, varying only the peak wavelength.

The output power is computed by multiplying the two spectra and then integrating the product over the wavelength. The simulation is performed with Python, applying the function `np.trapz()` to compute the integral of the product. This computation allows finding the output power for each RI. Repeating the procedure in a suitable, for the application, range of refractive indexes, it is possible to obtain the relation between the RI and output power. This relation, as shown in the following, can be linear or parabolic depending on the position of the light source; so, choosing the best light source improves the sensitivity and can also lead to a simpler relation that reduces the computational effort needed to detect the RI.

#### 4.1.1 Simulation with 1 LED

Fig. 4.4 reports the first simulation of the behavior of the intensity interrogation method. The light source is a LED centred at 670 nm. In Fig. 4.4 the SPR behavior and the spectral response of the LED are not reported in scale and only the spectral position has to be considered; the height is modified for visibility purposes.

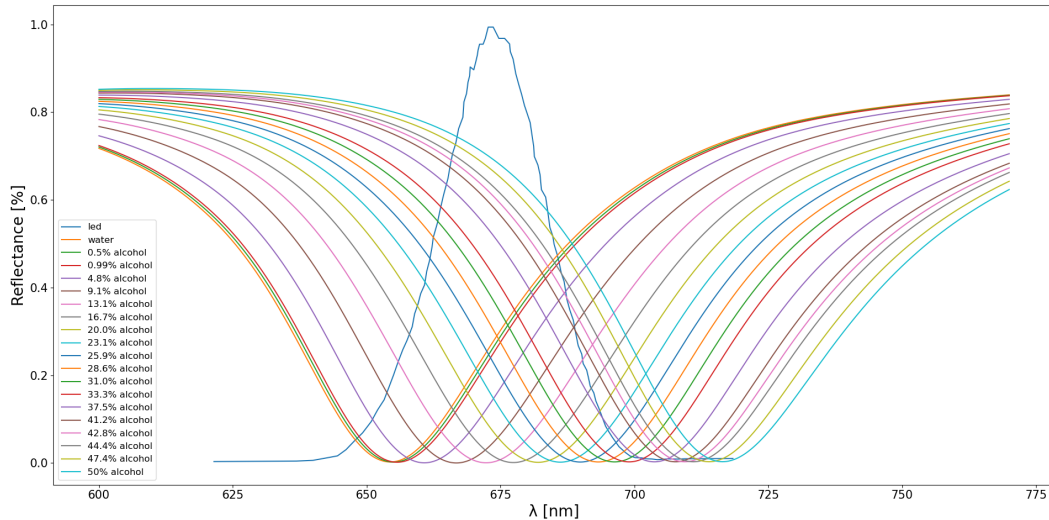


Figure 4.4: Simulation of the SPR behaviour with a LED source (670 nm).

As said before, the spectral response of the LED is obtained from a generic LED from Thorlabs, moved into the spectrum to reach the wanted peak value. The spectral response is not really accurate using this procedure but it leads to good results, allowing the selection of the proper peak wavelength for the source.

The peak wavelength is in middle of the working interval. This allows having a good

sensibility in the interval of interest.

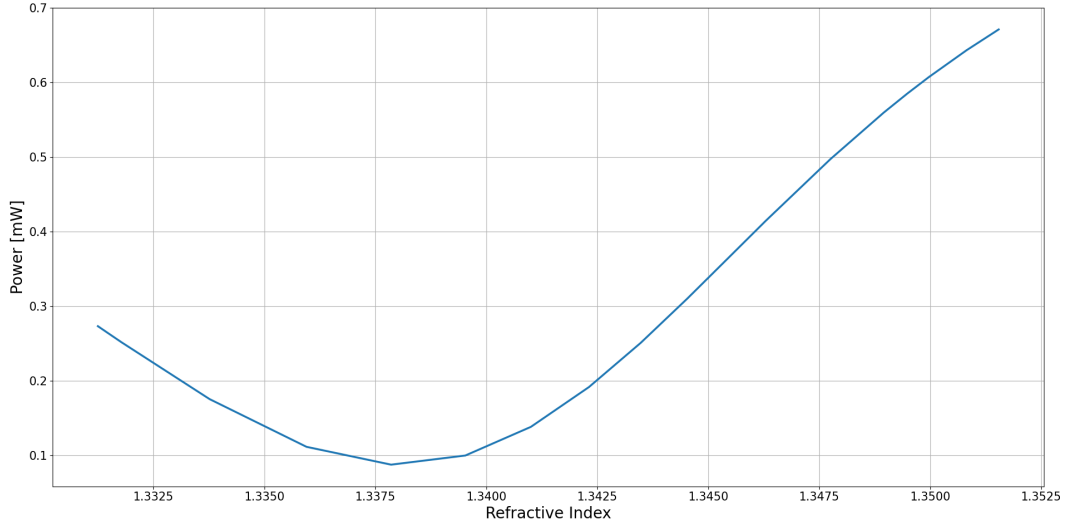
As shown in Fig. 4.5a, one single LED is not enough to sense correctly and in a unique way the refractive index: one value of output power corresponds to two different refractive indexes. So to use this configuration, we must be sure to work in a specific RI range, such as 1.34-1.35 in the considered case. Selecting the proper working range for the RI leads also to a better relation between power and RI: in the case reported in Fig. 4.5a, as visible in Fig. 4.5b, from 1.34 to 1.35 Refractive Index Unit (RIU) the characteristic is approximately linear, leading to an easier analysis of data. Moving the peak wavelength of the LED modifies the range at which the power in function of the RI is linear: the higher the peak wavelength, the higher the RI.

Using the proposed LED leads to a sensitivity of 54 mW/RIU (Eq. 4.12).

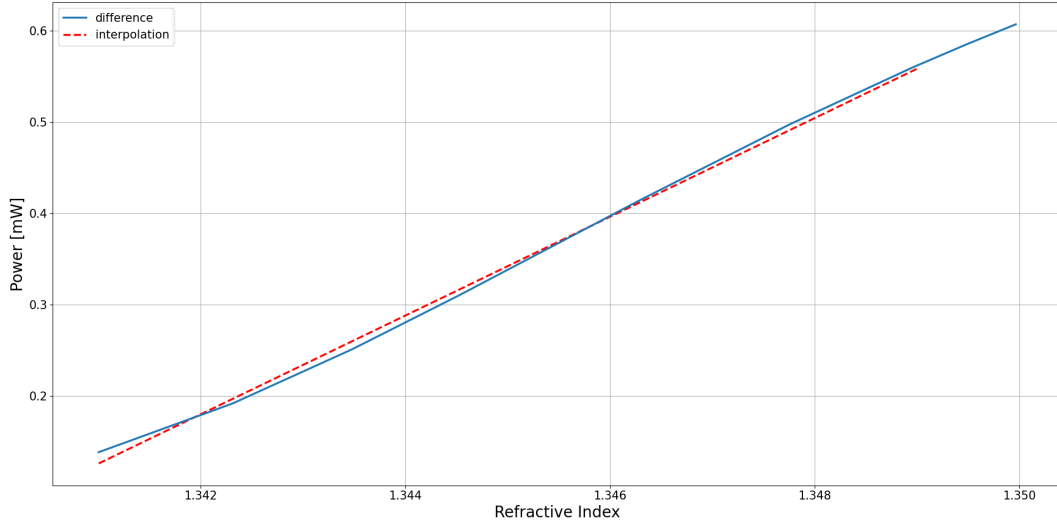
$$S = \frac{\delta P}{\delta n} \left( \frac{\text{mW}}{\text{RIU}} \right) \quad (4.12)$$

#### 4.1.2 Simulations with a single laser

The simulation is repeated considering a laser emitting at  $\lambda = 672$  nm, as reported in Fig. 4.6. Here too, the spectral response of the laser is obtained from a datasheet of a real laser available from Thorlabs [26] and, in Fig. 4.6, the plot is not reported with the correct scale, since the intensity has been modified for visibility purposes. The overall behavior of the system can be considered as unmodified when varying the light source: also in this case the RI cannot be sensed unequivocally in the entire range but only in a reduced interval where the characteristic is linear (Fig. 4.7a, Fig. 4.7b). The main drawback in using lasers instead of LEDs is the reduction of the sensitivity that goes from 54 mW/RIU to 2.5 mW/RIU. While in the case of LED source, accepting to work in a reduced RI interval, it can be possible to implement the intensity interrogation system employing just one LED, in the case of a laser source the low sensitivity does not allow the use of only one laser.



(a) Output power in function of refractive index.



(b) Output power in function of refractive index with linear interpolation.

Figure 4.5: Output power in function of refractive index, simulation with one LED.

### 4.1.3 Simulations with two lasers

Since it is not useful working with one laser, also simulations with two lasers emitting at different wavelengths is proposed. The first simulation presents two lasers at 660 nm and 740 nm, as shown in Fig. 4.8. In this case it is reported the relation between the output power and the refractive index for the two different lasers (Fig. 4.9). The two curves are not linear and the one correspondent to the laser at 660 nm presents also a quasi-horizontal part that does not allow to sense properly the RI. It is interesting to notice that, computing the difference between the two previous curves, the relation between the

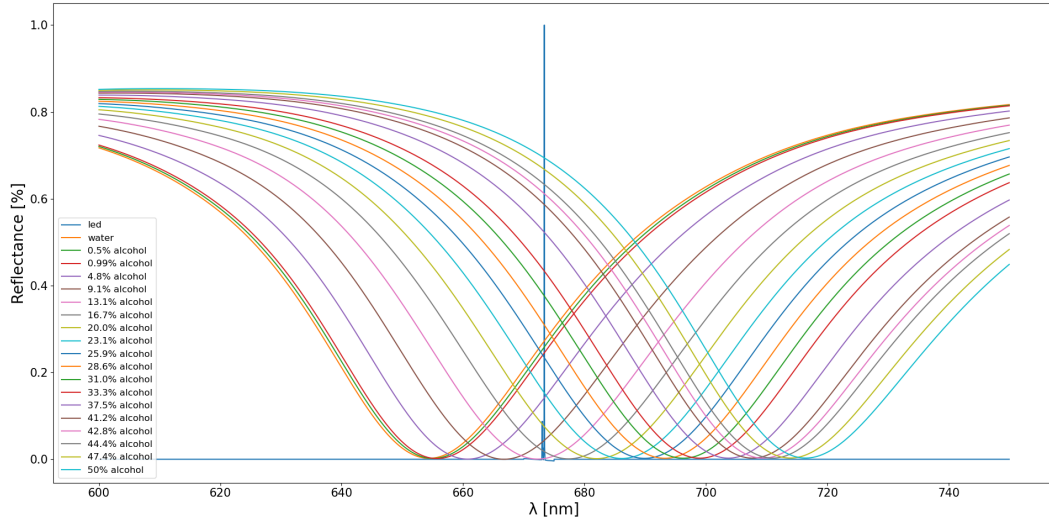


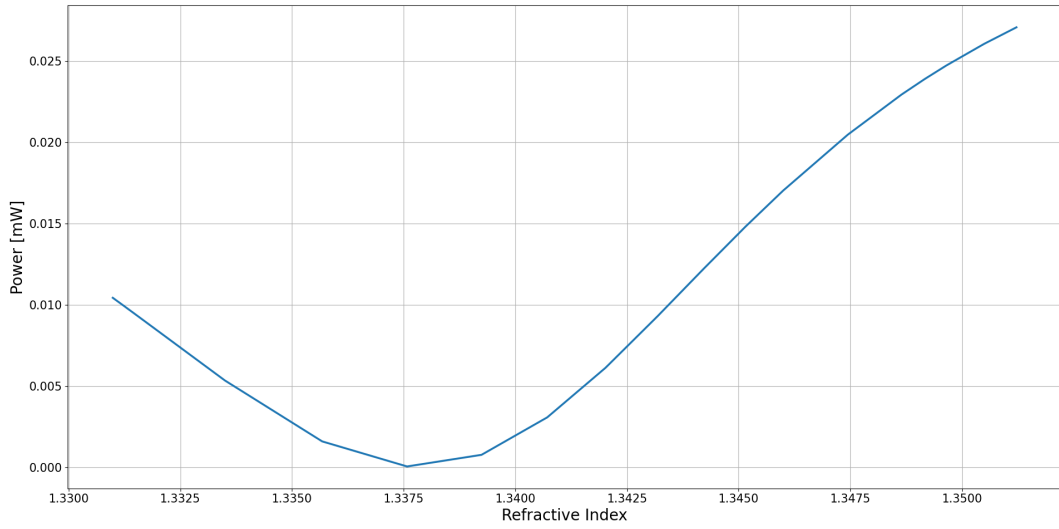
Figure 4.6: Simulation of the SPR behaviour with a laser source (672 nm).

power and the refractive index becomes quite linear, even if still presents the horizontal part that limits the RI interval.

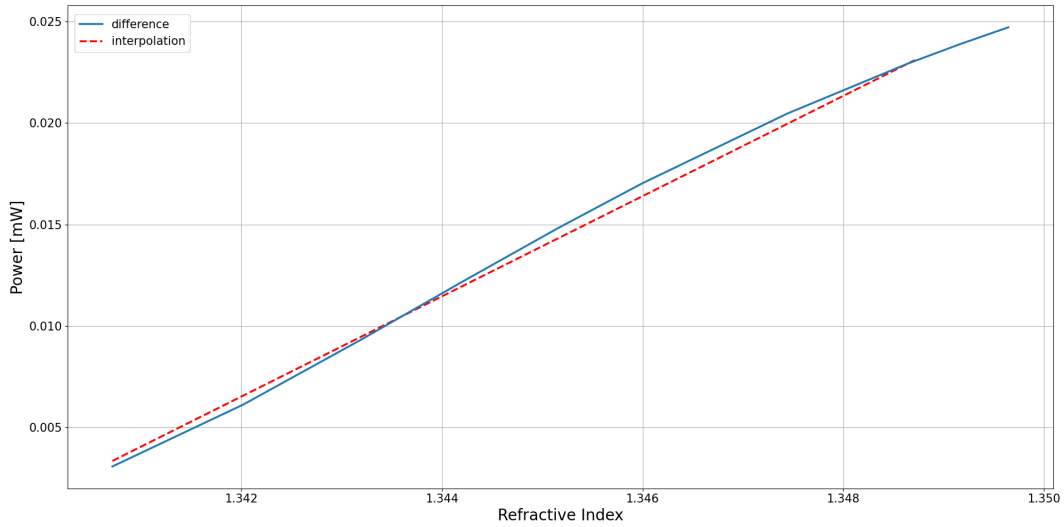
Repeating the simulation with a laser at 740 nm as before and a laser at 645 nm instead of 660 nm (Fig. 4.10) shows that the relations of power and RI again are not linear (Fig. 4.11) but performing the difference between the two a linear relation is obtained (Fig. 4.12) in a RI interval that suits perfectly the range needed for water-related applications, which goes from 1.33 (RI of water) to a RI of 1.35 (50% water-alcohol, a huge equivalent contamination for drinking water). In this case the sensitivity of the sensor is 64 mW/RIU, a really good improvement with respect to the case with a single laser, where the sensitivity is around 2.5 mW/RIU. The main drawback of this solution is that it requires a fiber coupler to use simultaneously two lasers, making the set-up more complicated and expensive.

#### 4.1.4 Simulation with two LED

Given the good results obtained with two lasers, we have decided to analyze also the use of two LEDs, even if the solution with a single LED has an already pretty good performance. The results are shown in Fig. 4.13 (figure not in scale). The two LED are placed at 645 nm and 735 nm, respectively. As shown in Fig. 4.14, the relations between power and RI are nonlinear, while the difference between the two curves (Fig. 4.15), is again linear over a useful range. In this case the sensitivity is 58 mW/RIU suggesting that the introduction of a second LED is not so relevant for the improvement of the sensitivity since before was 54 mW/RIU. The main improvement done by the introduction of the second LED is the larger RI range in which the characteristic is linear, from 1.33 to 1.35, while before it was only 0.01 RIU. The improvement in RI range is not so relevant for



(a) Output power in function of refractive index.



(b) Output power in function of refractive index with linear interpolation.

Figure 4.7: Output power in function of refractive index, simulation with one laser.

the considered application since the RI interval in which water is considered drinkable is limited.

All the results from the simulations are summarised in Table 4.1.

Considering the drawbacks related to hardware needed for the second light source and the differences in terms of RI interval and sensitivity, the best compromise in terms of performances vs complexity and costs is the solution with one single LED.

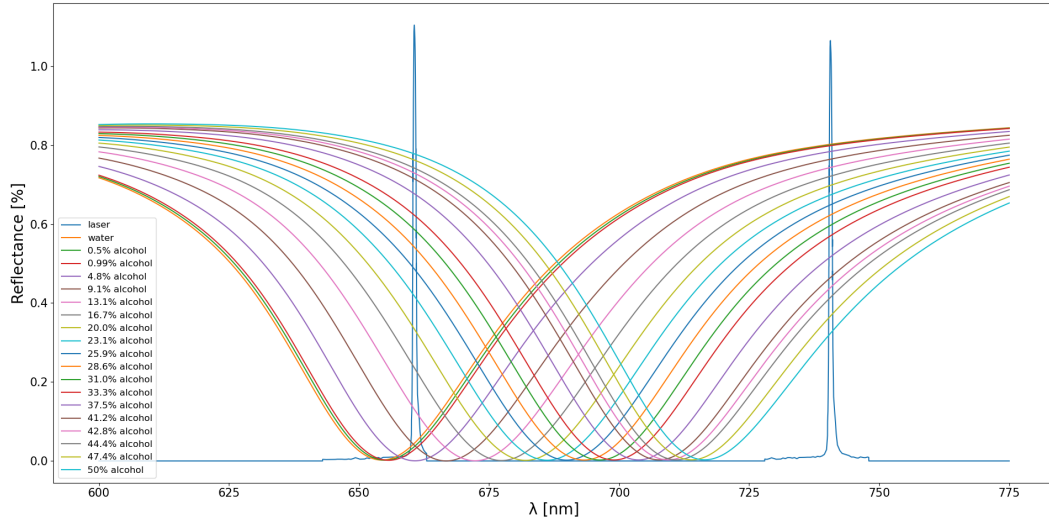


Figure 4.8: Simulation of the SPR behaviour with a laser source (660 and 740 nm).

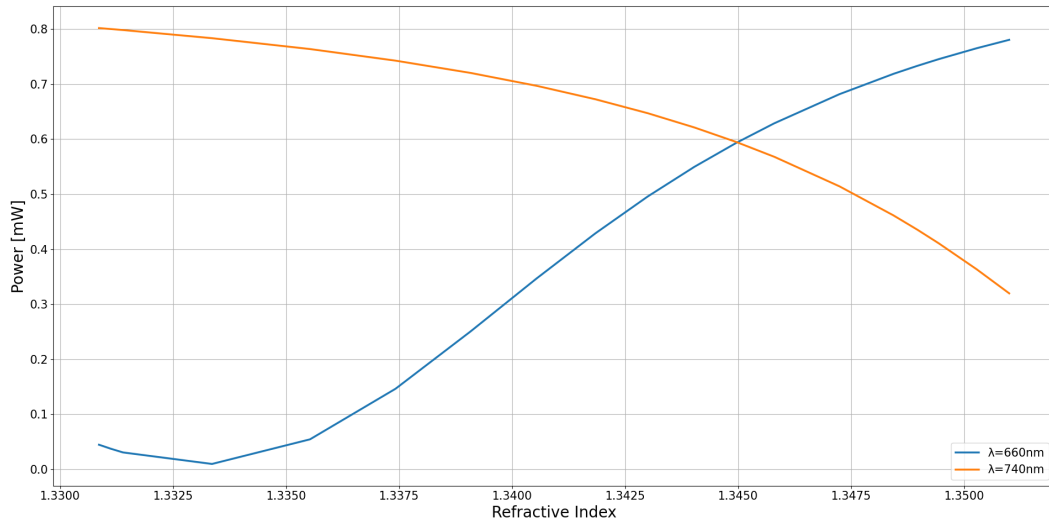


Figure 4.9: Output power in function of refractive index, simulation with two lasers.

## 4.2 Experimental setup and materials

The set-up is a transmission configuration based on the intensity interrogation method, with a single wavelength light and a power meter. The light source is a Ratioplast 660 nm LED with SMA connector (905SE660SM106 [27]), driven by a current generator. The other end of sensing fiber is connected to a Compact USB Power Meters (PM16-120 [28]). On both ends a Thorlabs Universal Bare Fiber Terminator (BFT1 [15]) equipped with a SMA905 multimode connector (B10440A [16]) is used to connect the fiber sensor to the

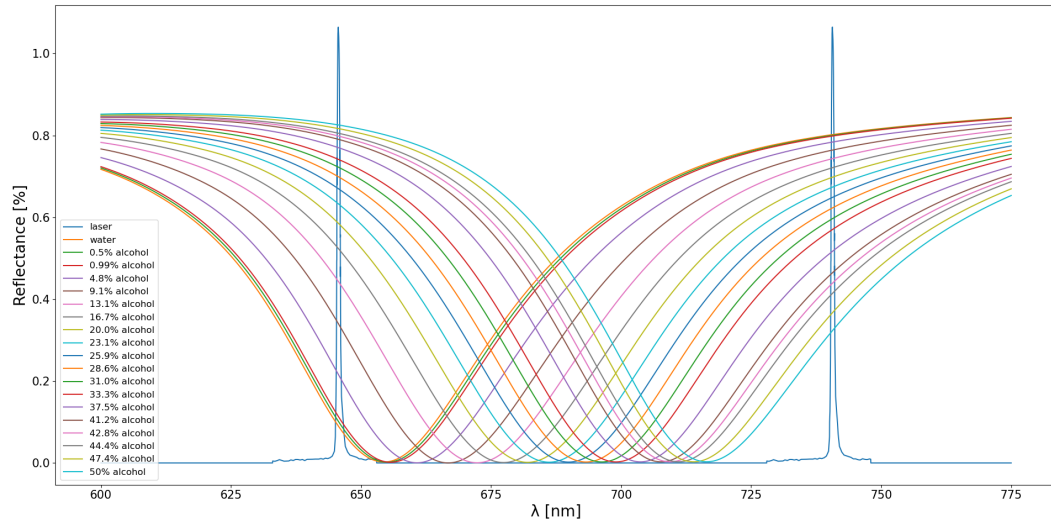


Figure 4.10: Simulation of the SPR behaviour with a laser source (645 and 740 nm).

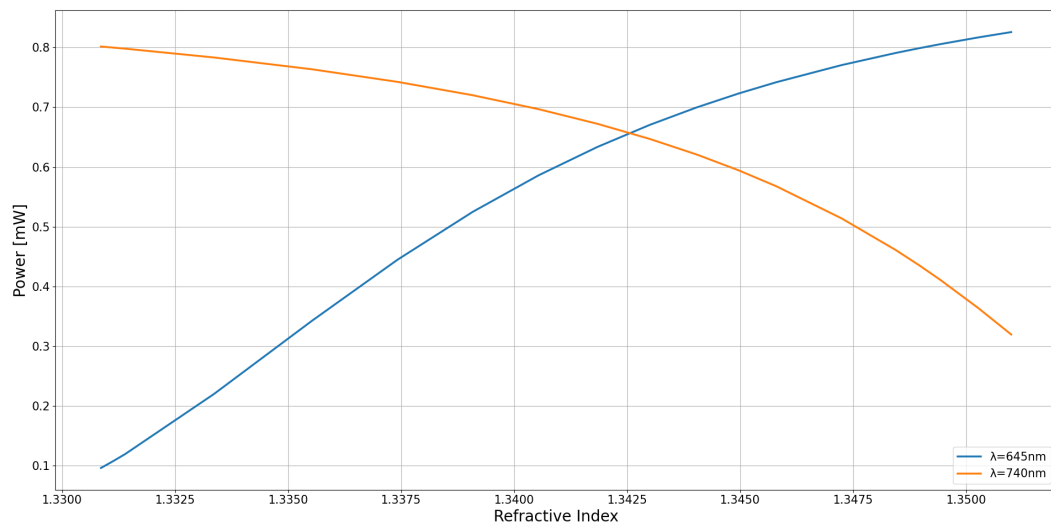


Figure 4.11: Output power in function of refractive index, simulation with two lasers.

instruments.

Since the SPR's behavior is affected also by the temperature variations, it is useful to monitor it in order to have more accurate RI measurements. In our experiments, the temperature has been measured through an Fiber Bragg Grating (FBG) interrogated with an Ibsen spectrometer.

The FBG sensor is glued to a metallic support in order to reduce the strain applied on it while the water-alcohol solution is modified by adding alcohol, otherwise the fluid movement would introduce artifacts due to the strain-temperature cross sensitivity.

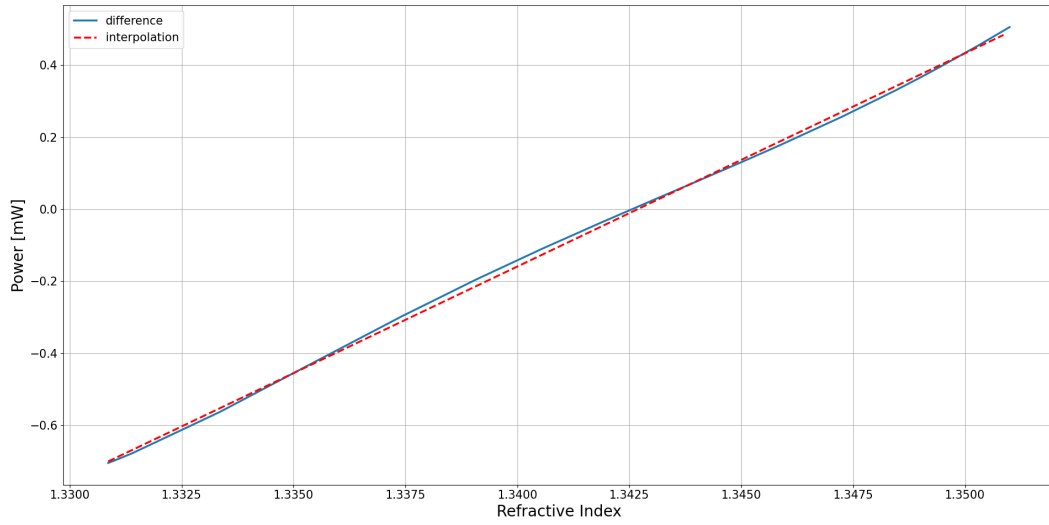


Figure 4.12: Difference of two output power in function of refractive index with linear interpolation.

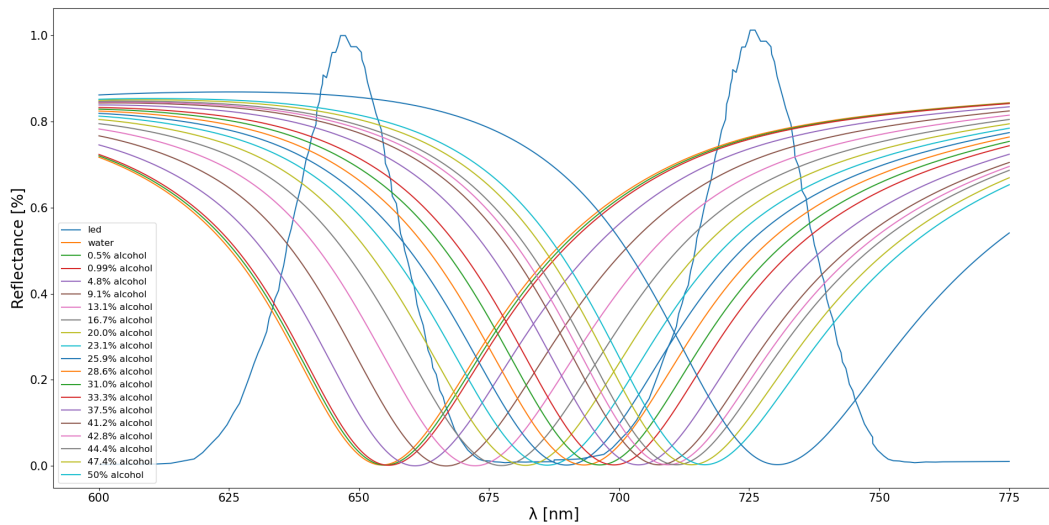


Figure 4.13: Simulation of the SPR behaviour with a LED source (645 and 735 nm).

### LED testing

First of all the LED is connected to the set up to measure the value of the power in air, without any solution in the surrounding of the sensor. This measure is performed in order to understand the stability of the LED in time. In Fig. 4.16a it is reported the result: the output power decreases for the first 20 minutes, then it reaches a constant value, suggesting that for accurate measurements the LED requires to be switched on in

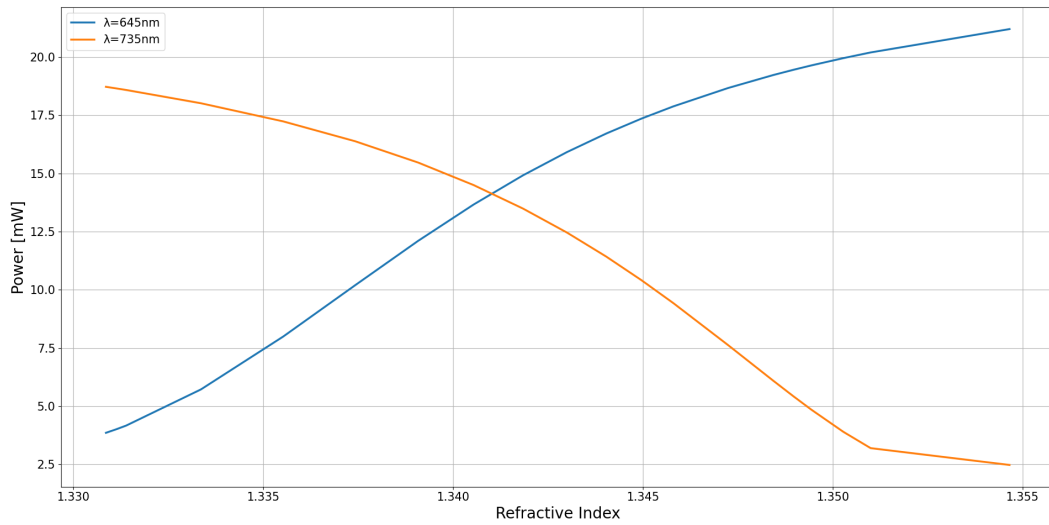


Figure 4.14: Output power in function of refractive index, simulation with two LED.

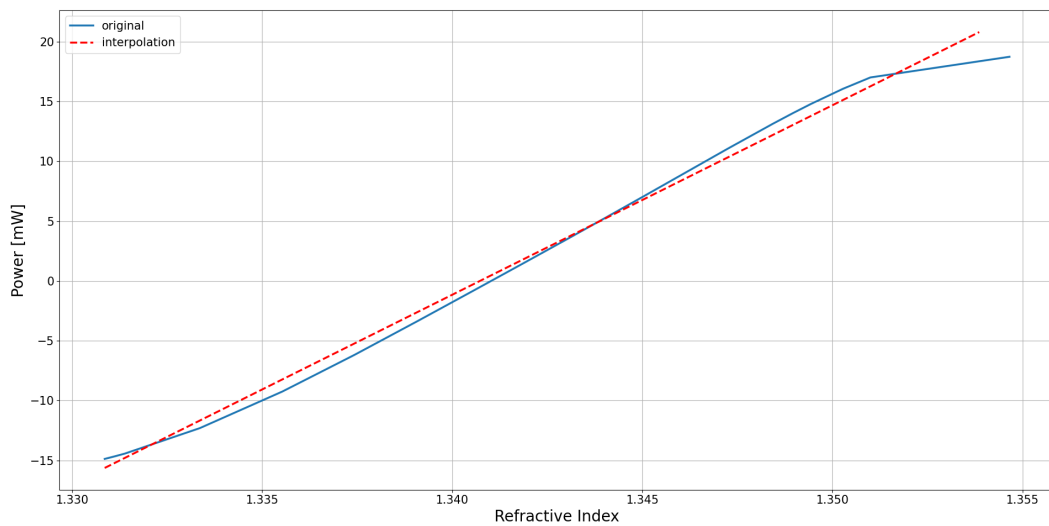


Figure 4.15: Difference of two output power in function of refractive index with linear interpolation.

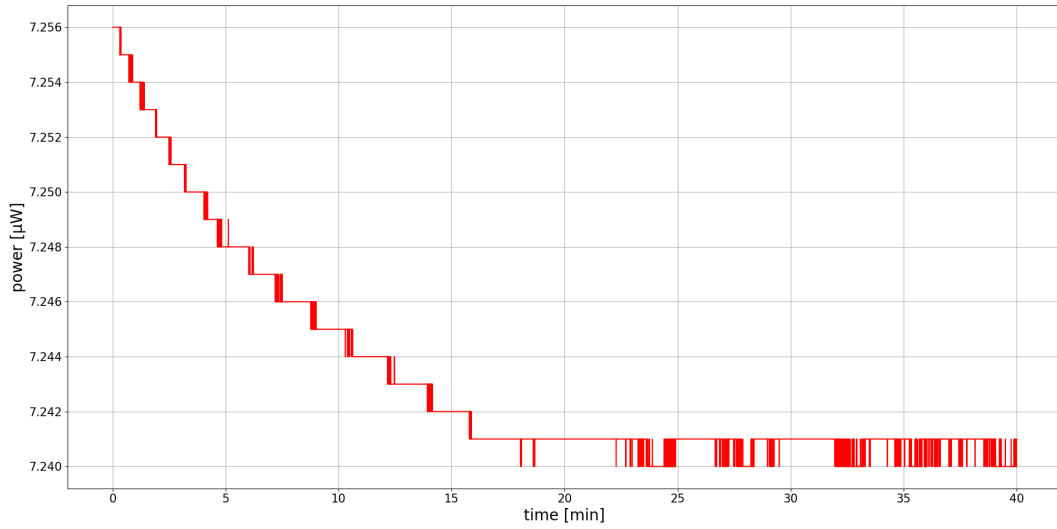
advance to let it warm up or to use it in a pulsed way in order to maintain it at the same temperature at every pulse. The test is repeated a second time (Fig. 4.16b) showing a similar behaviour: it takes around 20 minutes to reach the correct output power. The usage of the LED in the first 20 minutes leads to incorrect measures both in terms of temperature compensation and in terms of refractive index. This issue must be taken into account in any test performed in the following.

In Fig. 4.17 it is reported, not in scale, the spectral response of the SPR sensor

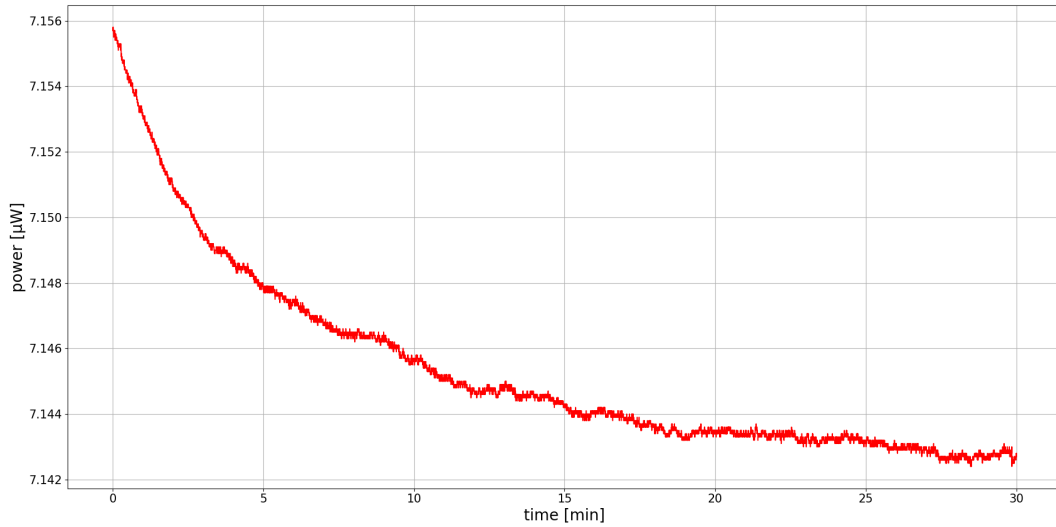
Table 4.1: Summary of simulation results.

Light source	$\lambda_{1\text{peak}}$	$\lambda_{2\text{peak}}$	RI interval	Sensitivity
LED	670 nm		1.34-1.35	54 mW/RIU
laser	672 nm		1.338-1.350	2.5 mW/RIU
laser	660 nm	740 nm	1.332-1.350	64 mW/RIU
laser	645 nm	740 nm	1.330-1.355	64 mW/RIU
LED	645 nm	735 nm	1.330-1.355	58 mW/RIU

and of the LED used in this set-up. The three spectra are acquired with the Avantes spectrometer already used for the wavelength interrogation method; also the broadband light source used to obtain the spectra of the SPR is the same already used before. As it can be seen the peak of the LED is on the right of the SPR dip relative to the water, while in the simulation it was used a LED on the left side. Fig. 4.17 also reports the spectral responses relative to pure alcohol, which represents the extreme limit reachable with the solution used for the further tests. All the spectra relative to water-alcohol solution will be in between these two spectral responses. The position of the LED is optimized for the detection with larger sensitivity of the solution with higher concentration of alcohol, rather than that with more water.



(a) First test.



(b) Second test.

Figure 4.16: LED testing.

### 4.3 Experimental test with one LED

The procedure followed for the test is very similar to the previous ones where the wavelength interrogation method was used. The power meter is connected to the PC with an USB cable and the output power is read in real time through an application from Thorlabs (Optical Power Monitor) without having to develop a specific LabVIEW program. Also the processing of the acquired data is really simplified in this case: indeed, it is necessary to acquire the output power value only to obtain the relative RI value, while in the wavelength interrogation method it is necessary to acquire the entire spectrum (a

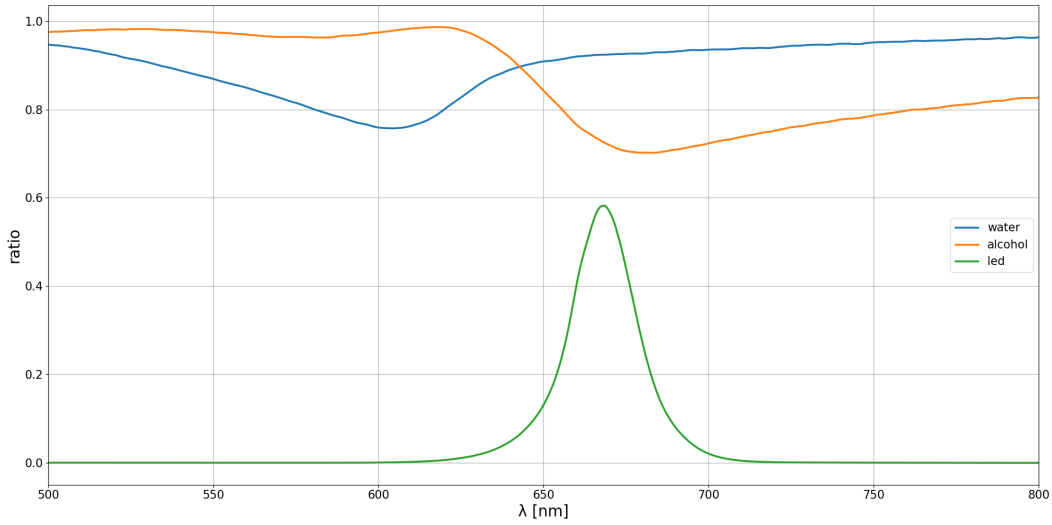


Figure 4.17: Spectral response of the SPR sensor and of the LED used in the set-up (not in scale).

huge quantity of data with respect to a single power value), which then must be divided by the reference one. In addition, the result also needs to be filtered or interpolated to reduce the noise. The power value in this case is “ready to use” and does not require any post processing. Also in this case the tests are performed using a water-alcohol solution with different concentrations, thus with different refractive indexes.

## Results

The test is performed by acquiring manually one power value for each concentration of the solution. A small interval of time (about one minute) is waited before acquiring the power value in order to allow the solution to be homogeneous after the introduction of the alcohol. In Fig. 4.18 is reported the result of the test. The concentration of the alcohol is translated into a refractive index value using the model proposed in Eq. 3.1. As expected the relation between the output power and the refractive index is linear. The fact that the line has a negative angular coefficient while in the simulations it was positive is because here the peak wavelength of the LED is at the right of the SPR dip, while in the simulations the LED was on the left side. The noisy behavior of the plot is because both the concentration of alcohol cannot be changed exactly (the syringe we used is not accurate enough), and the acquisition is performed manually, acquiring only one value for each concentration, without averaging in a small interval of time. An other issue to notice is the reduction of the sensibility from the theoretical simulation (54 mW/RIU) to the experimental test (0.2 mW/RIU): this can be due to the losses at the interface between the LED and the fiber and between the fiber and the power meter. Even with this reduction of sensibility the sensing of the RI can be considered successful but this aspect will need further investigations and optimizations. Considering

the standard deviation with respect to the trend line a good result is obtained (0.049): even if the characteristic presents some noise, it has a good linear behavior the allows using the acquisitions without further data processing.

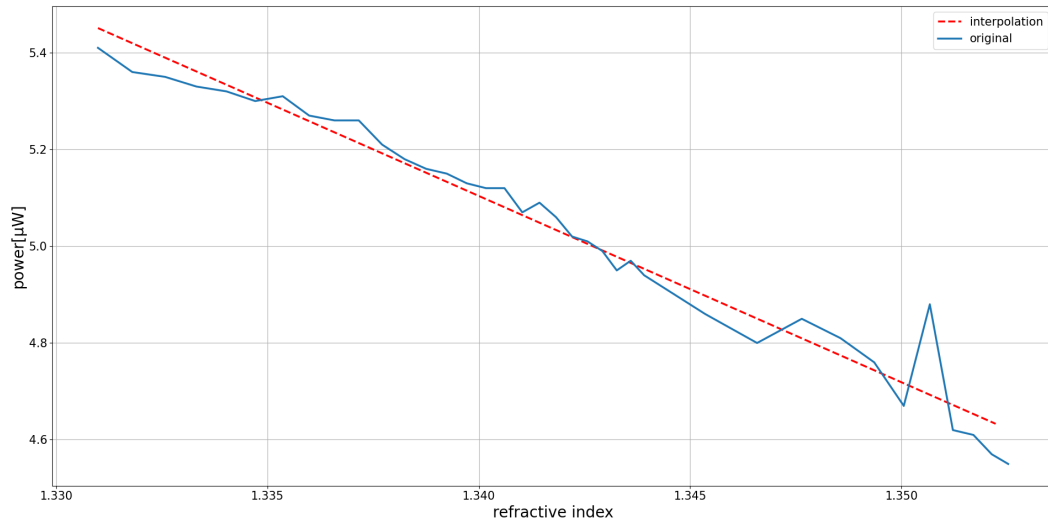


Figure 4.18: Output power in function of refractive index.



## Chapter 5

# Temperature compensation

### 5.1 Theoretical model

The temperature monitoring is done after a characterisation of the SPR sensor in terms of temperature and refractive index.

The relation between the SPR shift, the refractive index and the temperature is expressed in Eq. 5.1:

$$\begin{cases} \Delta P_{\text{SPR}} = c_1 \Delta T + c_2 \Delta n \\ \Delta \lambda_{\text{FBG}} = c_3 \Delta T + c_4 \Delta n \end{cases} \quad (5.1)$$

where:

$$c_1 = \left. \frac{\Delta P_{\text{SPR}}}{\Delta T} \right|_{\Delta n=0} \quad (5.2)$$

$$c_2 = \left. \frac{\Delta P_{\text{SPR}}}{\Delta n} \right|_{\Delta T=0} \quad (5.3)$$

$$c_3 = 10 \text{ pm/K} \quad (5.4)$$

The value of  $c_3$  is characteristic of the behavior of the FBGs, while the value of  $c_4$  is irrelevant because the evaluation of the  $\Delta \lambda_{\text{FBG}}$  is done with pure water and so  $\Delta n = 0$ . By evaluating  $c_1$  (Eq. 5.2) it is possible to remove the dependence of the temperature in the first equation in Eq. 5.1, allowing the computation of the RI in a more accurate way, since Eq. 5.3 can be rewritten as Eq. 5.5:

$$c_2 = \frac{\Delta P_{\text{SPR}} - c_1 \Delta T}{\Delta n} \quad (5.5)$$

Eq. 5.1 is valid also in the case of wavelength interrogation, just substituting  $\Delta P_{\text{SPR}}$  with  $\Delta \lambda_{\text{SPR}}$ .

## 5.2 Intensity interrogation

### 5.2.1 Temperature compensation: measurements

Several tests have been done in order to compute in a more accurate way the coefficient  $c_1$ , also because several issues were found. All the test are performed with hot water left cooling at room temperature. The FBG, since it has been carefully calibrated, provides only a temperature variation, not the absolute value, but for this application it is enough to know  $\Delta T$ . All the temperature measurements are performed submerging the FBG in water and measuring the correspondent wavelength displacement with the Ibsen spectrometer with an acquisition frequency of 100 Hz. In the same time also the acquisition of the power is carried on with the Thorlabs Optical Power Monitor, using an acquisition frequency of 1 kHz.

#### Test 1

In Fig. 5.1 it is reported the result of the first acquisition. Some considerations about it are reported in the following:

- The acquisition has been performed for 30 minutes, with a temperature variation of 20 °C.
- The temperature at the very beginning of the plot presents a step: this is due to the fact that the hot water was added after the beginning of the acquisition. The choice of adding the water after the start of the acquisition is made in order to have a reference for the room temperature. Also the power presents an abrupt change due to the introduction of water. This variation is not visible in Fig. 5.1 since the starting value is around 7  $\mu\text{W}$ , too large to allow to appreciate variations due to temperature changes.
- The temperature presents some steps characterised by a lot of oscillations: the cause of this behavior is not clear but probably, as discussed in the following, it is due to some physical characteristics of the FBG fiber.
- The behavior of the power and the temperature are very similar, suggesting a linear relation between the two values.

To further investigate the relation between the power and the temperature, in Fig. 5.2 it is reported the power in function of the temperature: as suggested before the relation is linear: the interpolating line has equation  $y = 0.006x + 5.25$ , from where the value of  $c_1$  can be obtained, since is the angular coefficient of the line (0.006  $\mu\text{W}/^\circ\text{C}$ ). One test is not enough to assume that 0.006  $\mu\text{W}/^\circ\text{C}$  is the correct value for  $c_1$ .

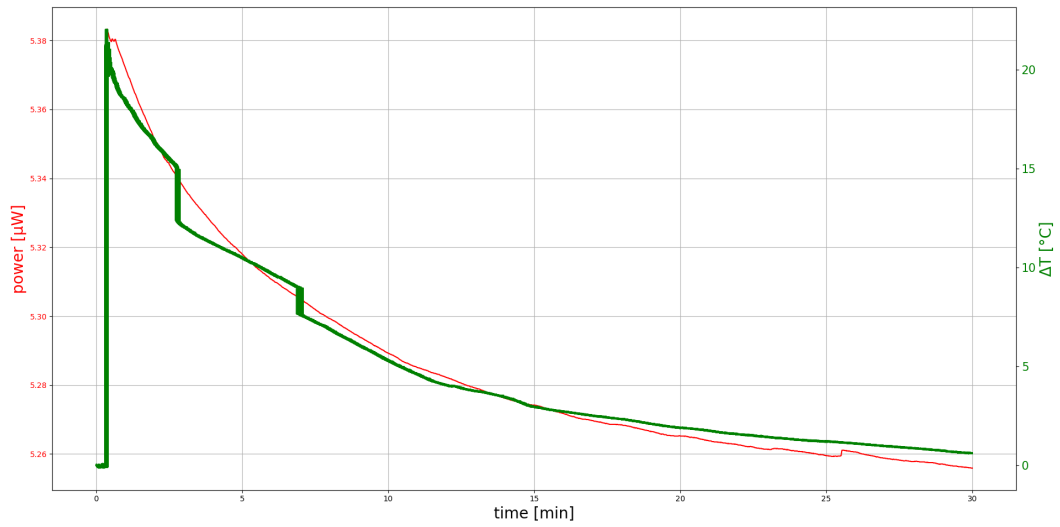


Figure 5.1: Acquisition of power and temperature.

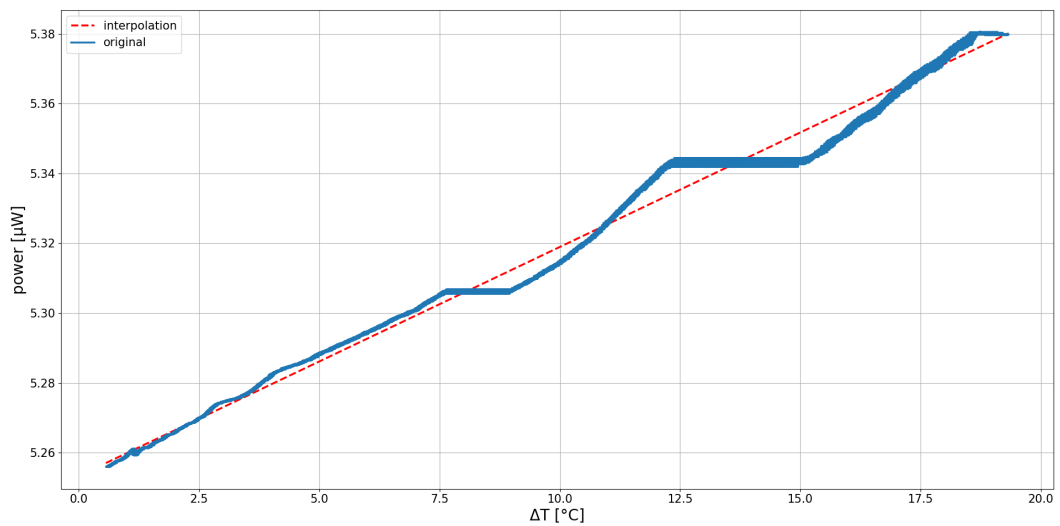


Figure 5.2: Acquired power in function of temperature.

## Test 2

The second test (Fig. 5.3) is not useful for the computation of the  $c_1$ , since the temperature is too noisy and disturbed. The problem in this case is the fact that the FBG is saturated, leading to random values of wavelength. To solve this issue it is enough to bend the optical fiber between the interrogator and the FBG to introduce some losses. During the first test the saturation of the FBG was not a problem because the fiber between the interrogator and the FBG was already bent due to the different position of the interrogator on the

working bench. To solve this issue the fiber is bent and fixed with a tape.

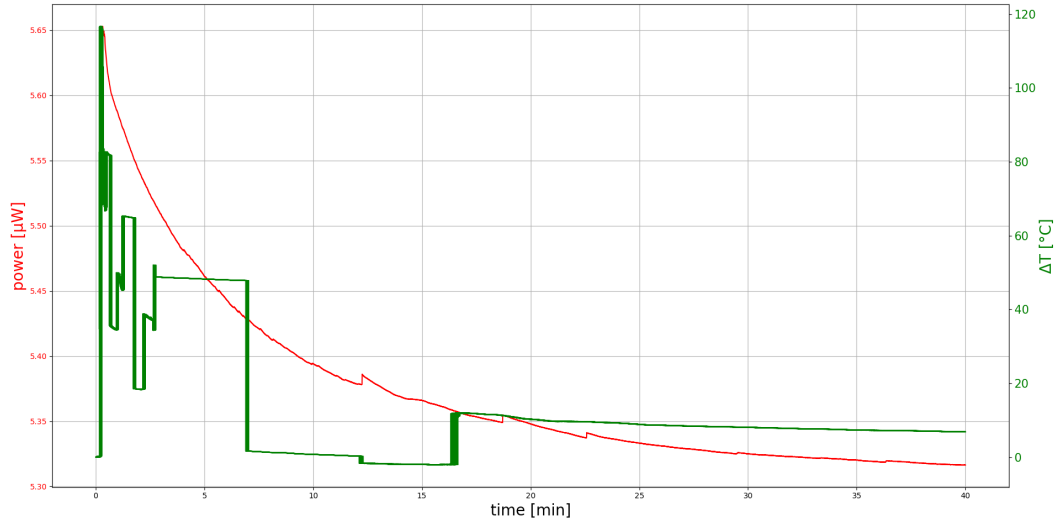


Figure 5.3: Acquisition of power and temperature.

### Test 3

In Fig. 5.4 it is reported the result of the third test. As it can be seen the acquisition has been performed for 40 minutes with a  $\Delta T = 90^{\circ}\text{C}$ .

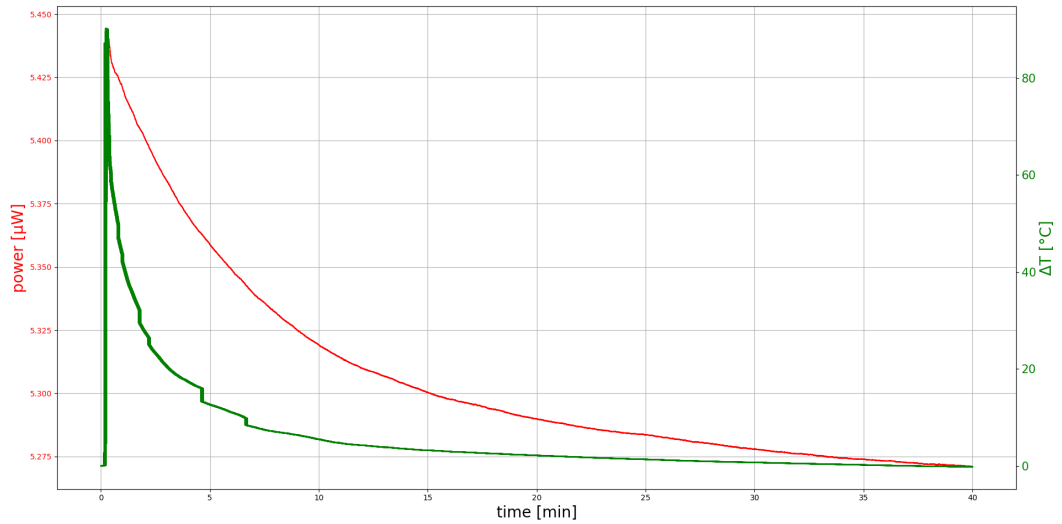


Figure 5.4: Acquisition of power and temperature.

Also in this case the issues highlighted for test 1 are valid except the last one: in this

case the relation between the power and the temperature is not linear.

As reported in Fig. 5.5 the relation in this case looks more like a parabola than a line. It is otherwise interesting to notice that the linear behavior is present in the first 20 °C, as reported in Fig. 5.6, suggesting that the linear relation is true only for limited temperature variations, from 25 °C (assumed as room temperature) and 45/50 °C in the specific case. This behavior can be considered as a limitation in the usage of the sensor but it must be kept in mind the application field: the drinking water can change its temperature, but it's quite impossible that reaches really high temperatures into the distribution system. From Fig. 5.6 it can also be found the interpolation line and its equation ( $y = 0.006x + 5.28$ ), from where it can be possible to obtain a second value for  $c_1 = 0.006 \mu\text{W}/^\circ\text{C}$ .

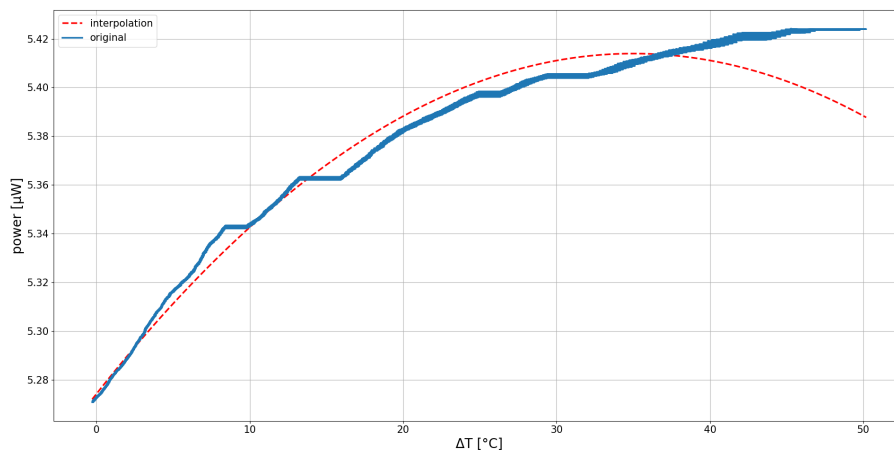


Figure 5.5: Acquired power in function of temperature.

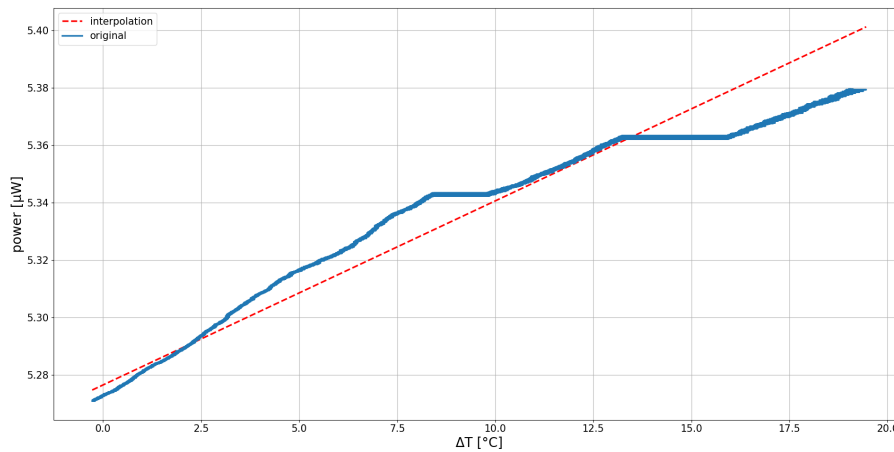


Figure 5.6: Acquired power in function of temperature.

**Test 4**

Fig. 5.7 reports the data acquired in the fourth test. Also in this case the test is performed with hot water left to cool at room temperature for 40 minutes, presenting a  $\Delta T = 40^\circ\text{C}$ . Also in this case the relation between power and temperature has a linear behavior for a limited range of temperature (Fig. 5.8). In the temperature range from  $0^\circ\text{C}$  to  $25^\circ\text{C}$  it is possible to interpolate the characteristic with a line with equation  $y = 0.0059x + 5.23$ , obtaining  $c_1 = 0.0059 \mu\text{W}/^\circ\text{C}$ .

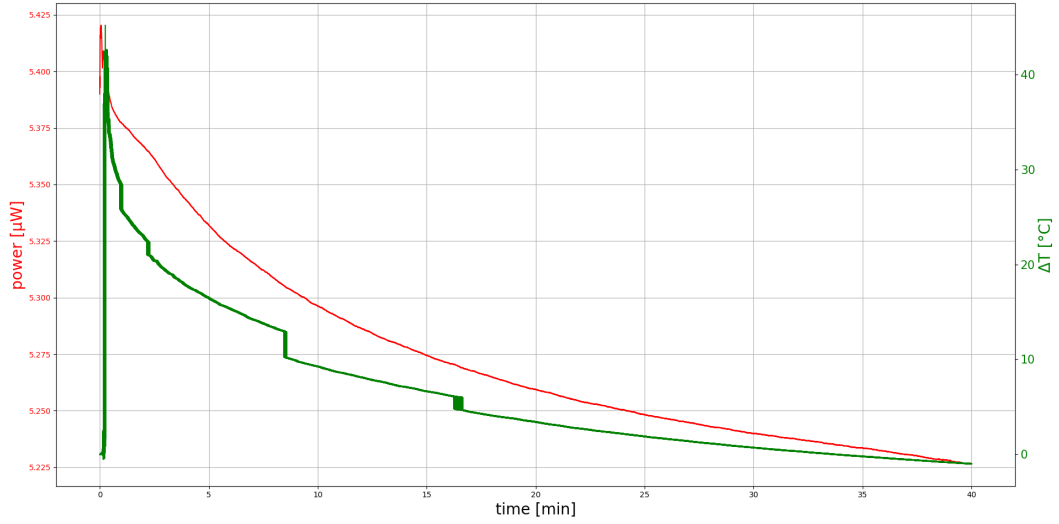


Figure 5.7: Acquisition of power and temperature.

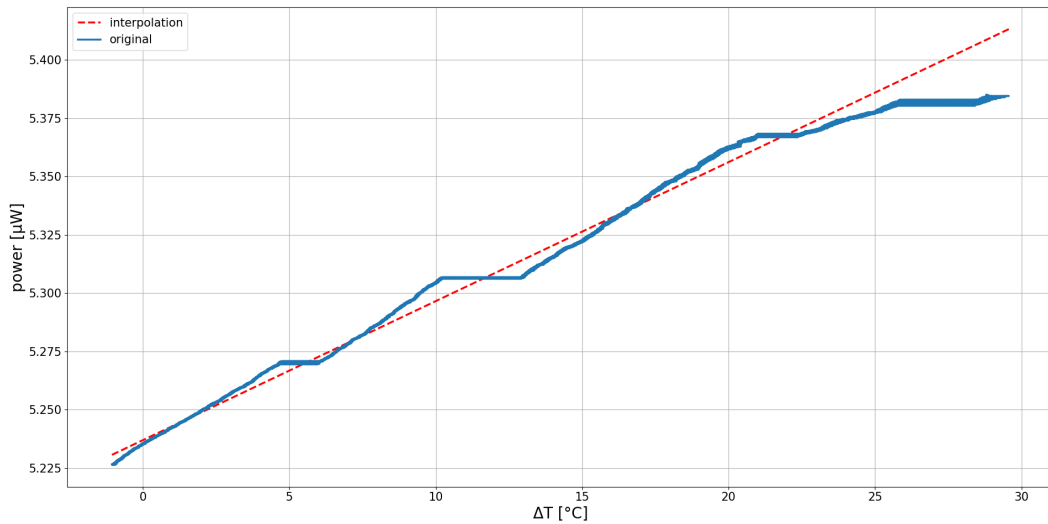


Figure 5.8: Acquired power in function of temperature.

**Test 5**

The previous considerations are also true for the fifth test, performed for 40 minutes with a  $\Delta T = 100^\circ\text{C}$  (Fig. 5.9). Also here the temperature range has to be limited to have a linear behavior, that allows obtaining  $c_1 = 0.0040 \mu\text{W}/^\circ\text{C}$  (Fig. 5.10).

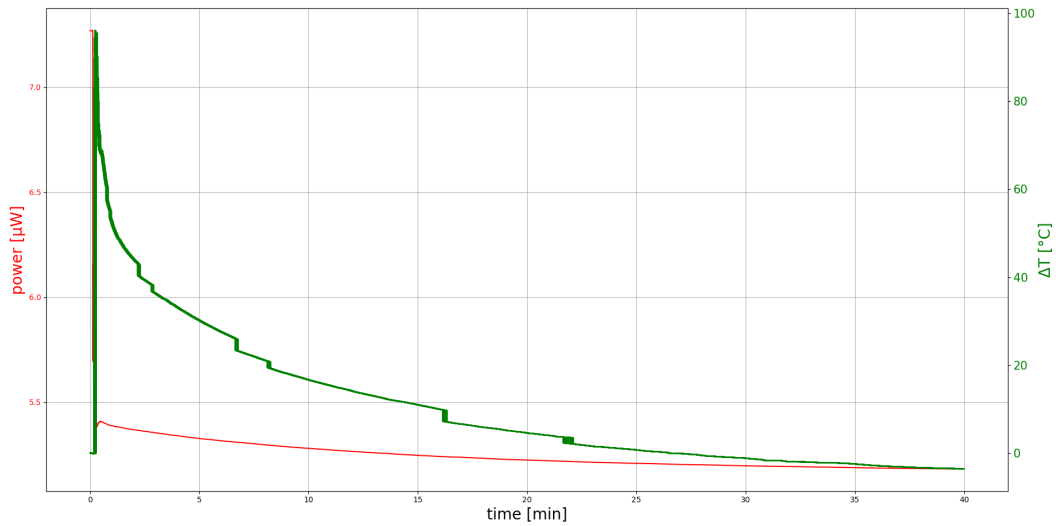


Figure 5.9: Acquisition of power and temperature.

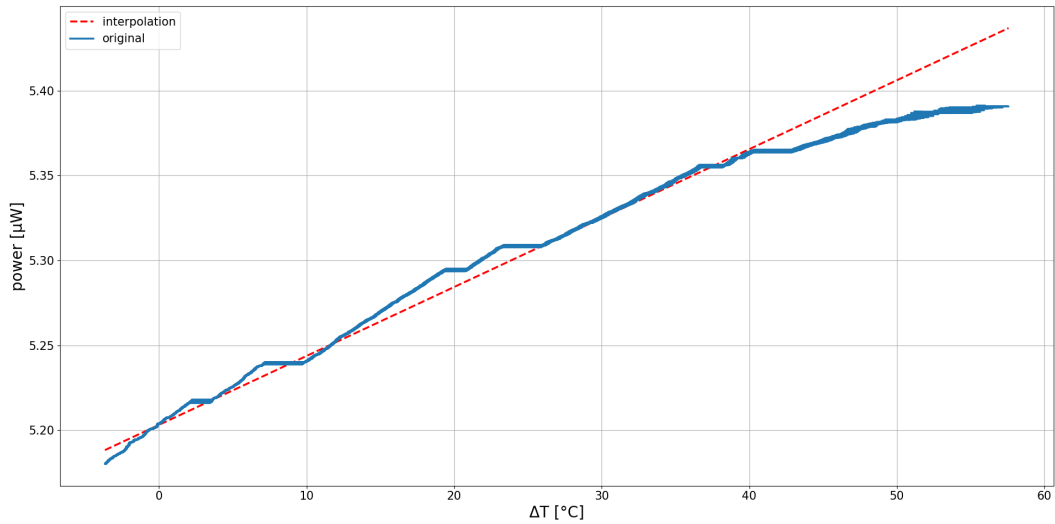


Figure 5.10: Acquired power in function of temperature.

### Test 6

The test is performed for 50 minutes with a  $\Delta T = 40^\circ\text{C}$  (Fig. 5.11). In this case the interpolation returns  $c_1 = 0.0044 \mu\text{W}/^\circ\text{C}$ ; the longer time of cooling, due to a higher room temperature with respect to previous tests, allows having a larger temperature interval with a linear relation between power and temperature (Fig. 5.12) but, as said before, for this specific application also a limited temperature range is enough.

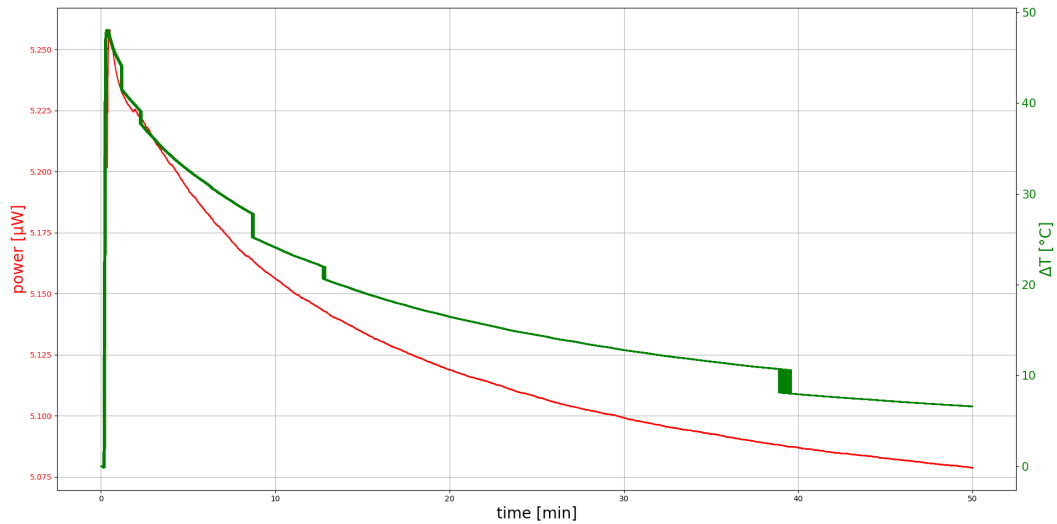


Figure 5.11: Acquisition of power and temperature.

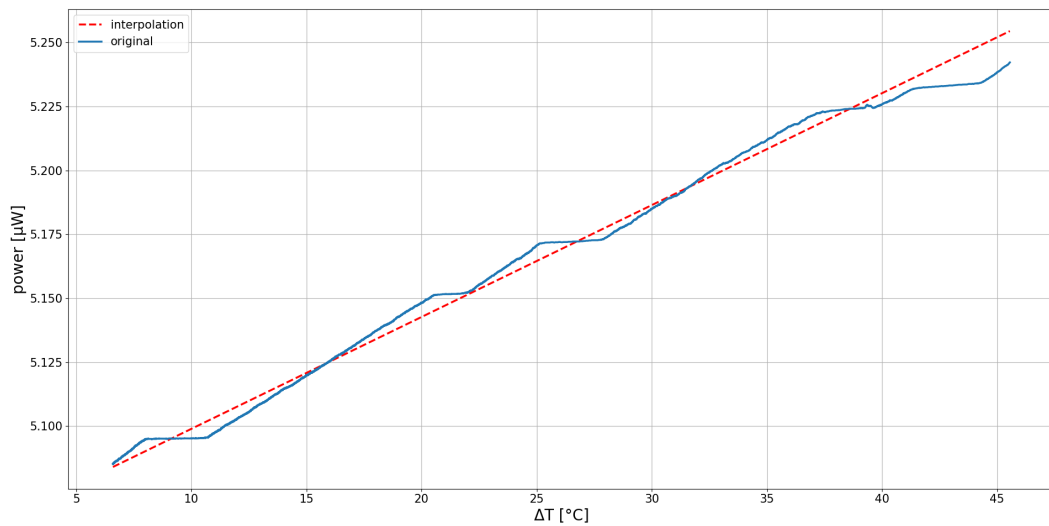


Figure 5.12: Acquired power in function of temperature.

Since 6 tests have been done the value of  $c_1$  can be computed in a more accurate way. In Tab. 5.1 are summarised the results.

Table 5.1: Summary of the computation of the temperature coefficient, intensity interrogation.

Test	$\Delta t$	$\Delta T$	Equation	$c_1$
1	30 min	20 °C	$y = 0.0060x + 5.25$	0.0060 $\mu\text{W}/^\circ\text{C}$
3	40 min	90 °C	$y = 0.0060x + 5.28$	0.0060 $\mu\text{W}/^\circ\text{C}$
4	40 min	40 °C	$y = 0.0059x + 5.23$	0.0059 $\mu\text{W}/^\circ\text{C}$
5	40 min	100 °C	$y = 0.0040x + 5.20$	0.0040 $\mu\text{W}/^\circ\text{C}$
6	40 min	40 °C	$y = 0.0044x + 5.05$	0.0044 $\mu\text{W}/^\circ\text{C}$

From Tab. 5.1 can be computed a mean value of the coefficient:  $c_1 = 0.0053 \mu\text{W}/^\circ\text{C}$ . From now on the computation of the refractive index can be done in a more accurate way removing the contribution of the temperature from the acquired power.

Another issue highlighted in Test 1 is the fact that the temperature acquisition presents a lot of steps with an oscillatory behaviour. Three further tests have been done to try to understand if there is a correlation between them. In Fig. 5.13 are reported the temperature acquisitions of the tests, performed again with hot water left cooling at room temperature.

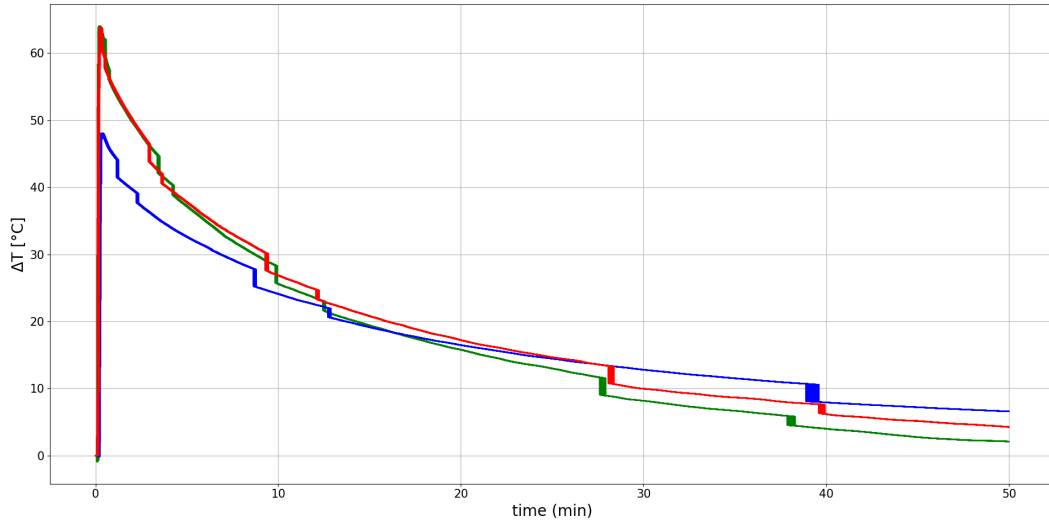


Figure 5.13: Multiple temperature acquisitions.

The green and red curves present a very similar behavior since they have been performed

very close to each other, while the third one have been done in a different day with different room temperature. Even with those differences the main thing that must be noticed is the fact that the steps are quite regular: they occur almost at the same temperature, suggesting that are due to something that happens every time the fiber reaches the same temperature. An hypothesis is that the plastic coating of the fiber, having a dilatation coefficient different from that of the silica, introduces some strain on the core. Unfortunately the coating of the fiber cannot be changed and so all the measures may be not so accurate due to this issue. In addition to that the behavior of the temperature cannot be filtered to remove the steps (Fig. 5.14), making the processing of the data really difficult. In case of real application of this sensor all the measures for the temperature compensation must be replied with an improved temperature sensor.

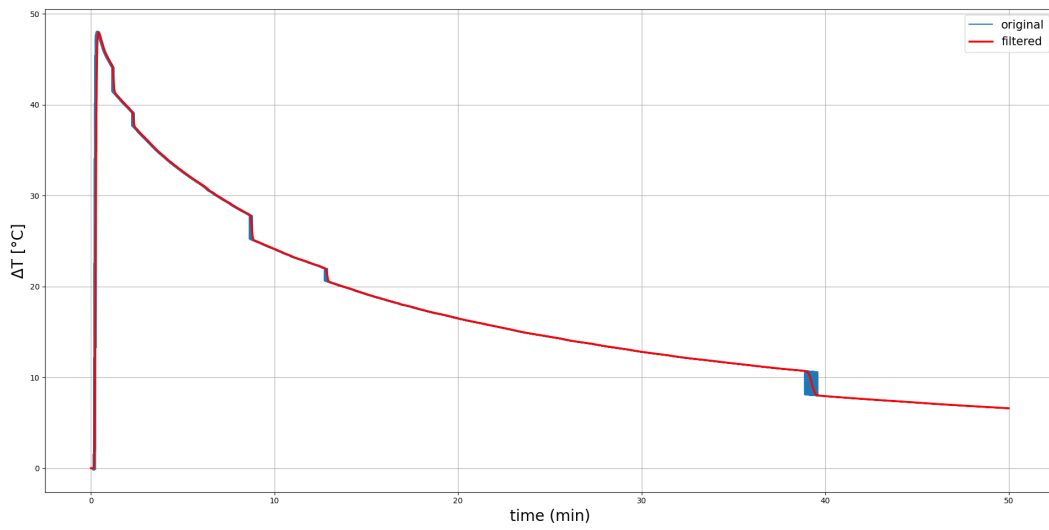


Figure 5.14: Temperature acquisition with filtering.

### 5.2.2 Refractive index measurements with temperature compensation

A test with a solution with changing RI has been carried out despite the issues reported in the previous paragraph. In Fig. 5.15 it is reported the acquired data for the temperature and the power. Some considerations about it are reported in the following:

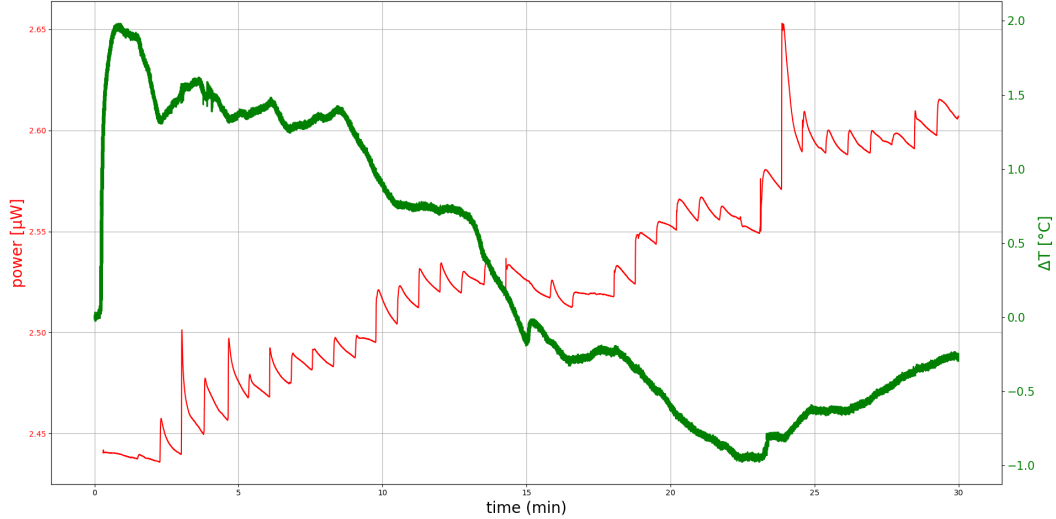


Figure 5.15: Acquisition of power and temperature.

- The test is performed with a solution of water (120 mL) and alcohol in different concentration: 1 mL of alcohol is added every 1 minute, in order to allow the solution to become homogeneous between two intervals.
- The temperature variation is of about  $3^{\circ}\text{C}$ , a range that allows using the coefficient  $c_1$  computed before, considered linear in a range of  $20^{\circ}\text{C}$ .
- The initial abrupt change in both power and temperature is because the water is added after the start of the acquisition.
- The power has a lower value with respect to the test performed before for the temperature compensation. This is due to the fact that fiber is connected to the LED and the power meter with a mobile connector that is not so good for measurements repeatability since every small displacement of the fiber modifies the power transmitted and received. In order to have repeatable measures a splicing with a fixed connector is needed. The variation of the power is just an offset, allowing the use of the consideration made until now for the temperature, since it affects each measure in the same way, not modifying the overall behavior. This test is performed just to understand if the use of the LED with the power meter is feasible for this application.

In Fig. 5.16 it is reported the variation of the power before and after the temperature compensation, showing small differences since the variation of the temperature is not so large.

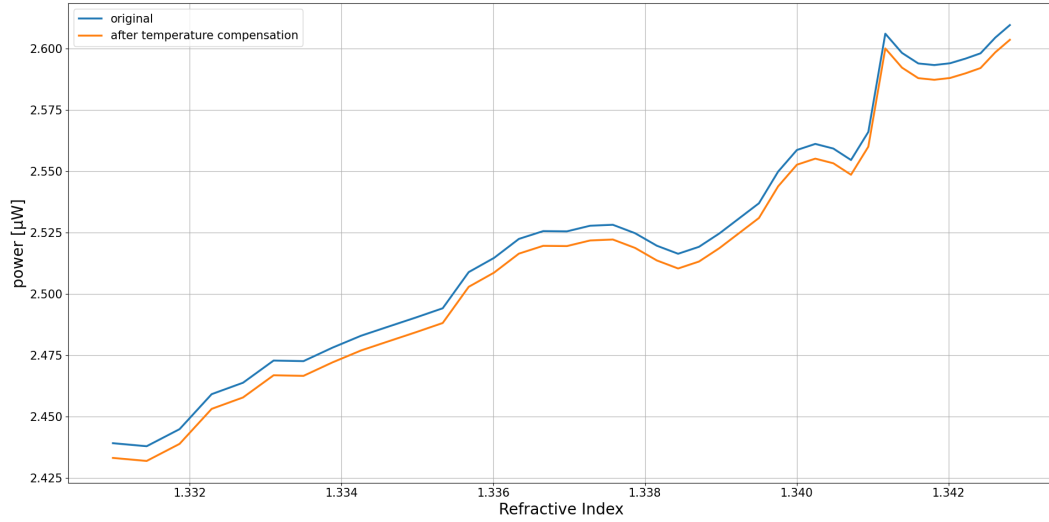


Figure 5.16: Acquired power compensated in temperature.

## 5.3 Wavelength interrogation

### 5.3.1 Temperature compensation: measurements

The same procedure followed for the temperature compensation in the intensity interrogation method is repeated substituting the LED and the power meter again with the broadband LED and the spectrometer. Also in this case the test are performed several times to obtain a more accurate result. The acquisition are performed with hot water let to cool at room temperature for 60 minutes.

#### Test 1

In Fig. 5.17 it is reported the acquisition of the first test, lasted 60 minutes. Again, as already explained in Chapter 3, the wavelength interrogation method has a really noisy behavior that require the processing of the acquired data. For this reason each spectrum must be interpolated with a parabola and then the result must be filtered with a FIR filter (Fig. 5.18). From Fig. 5.18 it can be seen also that a diminution of the temperature of about 30 °C causes an increase of the wavelength of about 15 nm. In Fig. 5.19 it is reported the relation between the wavelength and the temperature, and interpolating with a line, the  $c_1$  coefficient is obtained:  $-0.32 \text{ nm}/^\circ\text{C}$ . The very high noise in the wavelength acquisition is because the SPR fiber in this test was already used for many other tests and therefore with some damages in the gold coating. From the next test

another fiber, with the same characteristics, is used, reducing the noise but keeping all the other parameters unchanged.

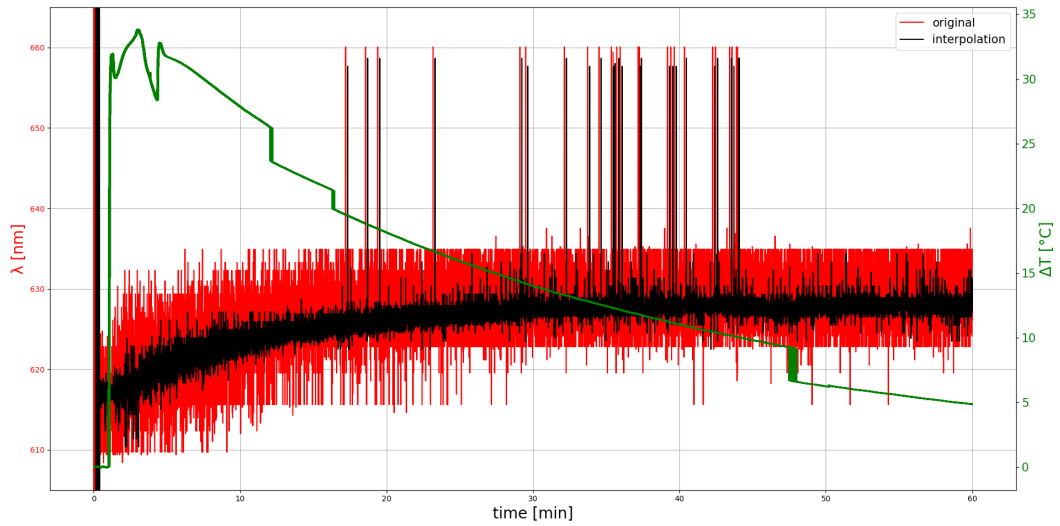


Figure 5.17: Wavelength of the dips and temperature.

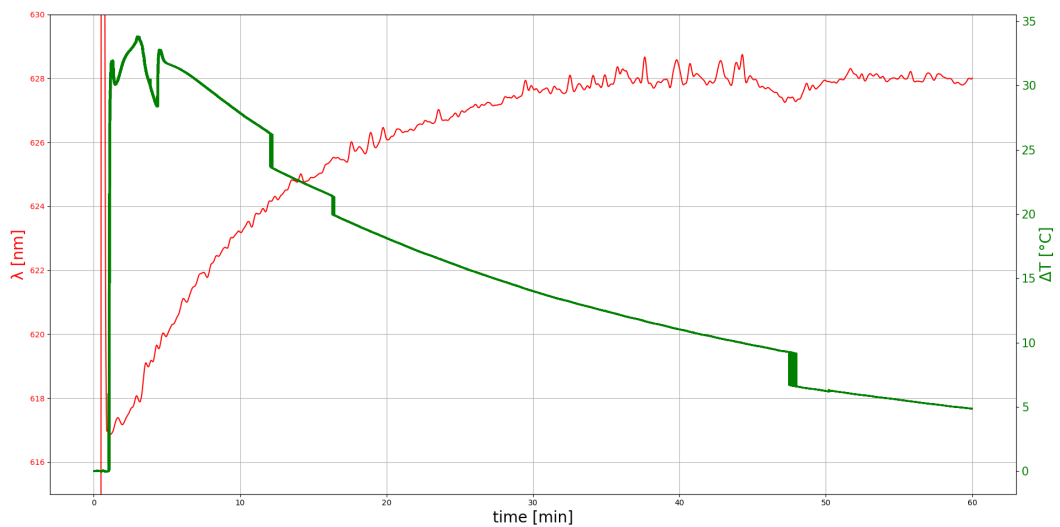


Figure 5.18: Wavelength of the dips filtered and temperature.

## Test 2

In Fig. 5.20 it is reported the acquisition of the second test, where the black curve represents the minimum values of the interpolated parabolas. Fig. 5.21 reports the same

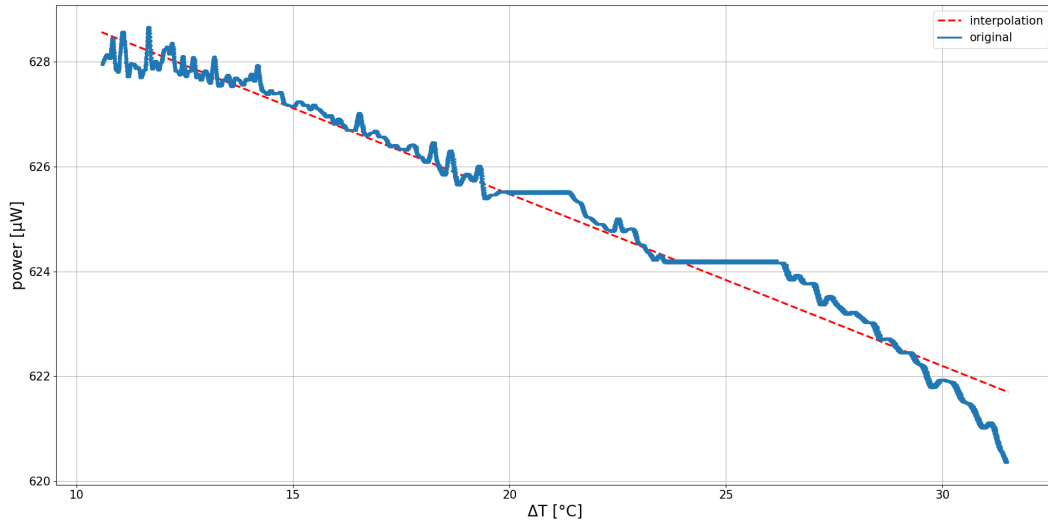


Figure 5.19: Acquired power in function of the temperature with interpolation.

acquisition after the application of the interpolation and the filter. The wavelength acquisition presents a smoother behavior, due to the fact that the used fiber is not damaged. The acquisition lasted 60 minutes with a temperature variation of  $50\text{ }^{\circ}\text{C}$  that leads to a wavelength red shift of  $5\text{ nm}$ . From Fig. 5.22 the interpolated line gives  $c_1 = -0.14\text{ nm}/^{\circ}\text{C}$ .

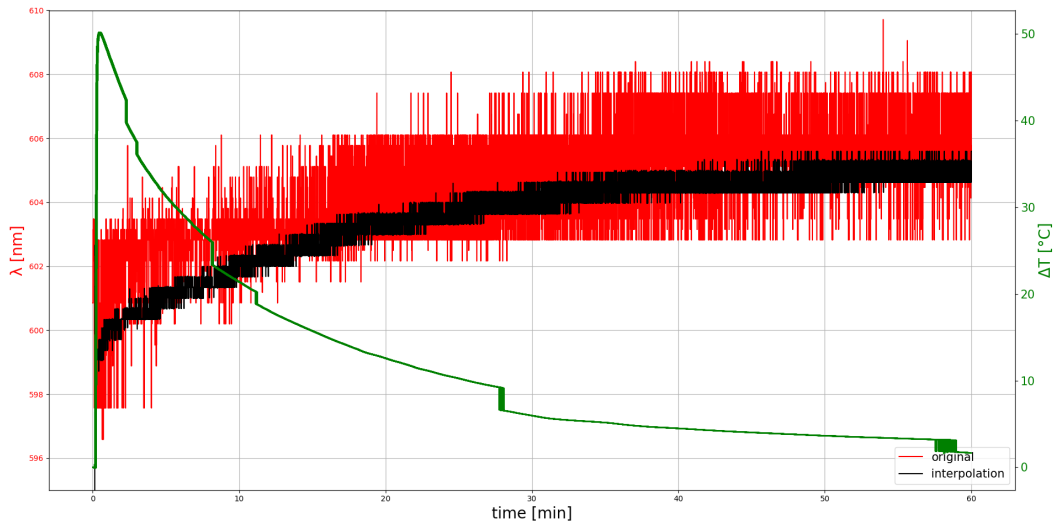


Figure 5.20: Wavelength of the dips and temperature.

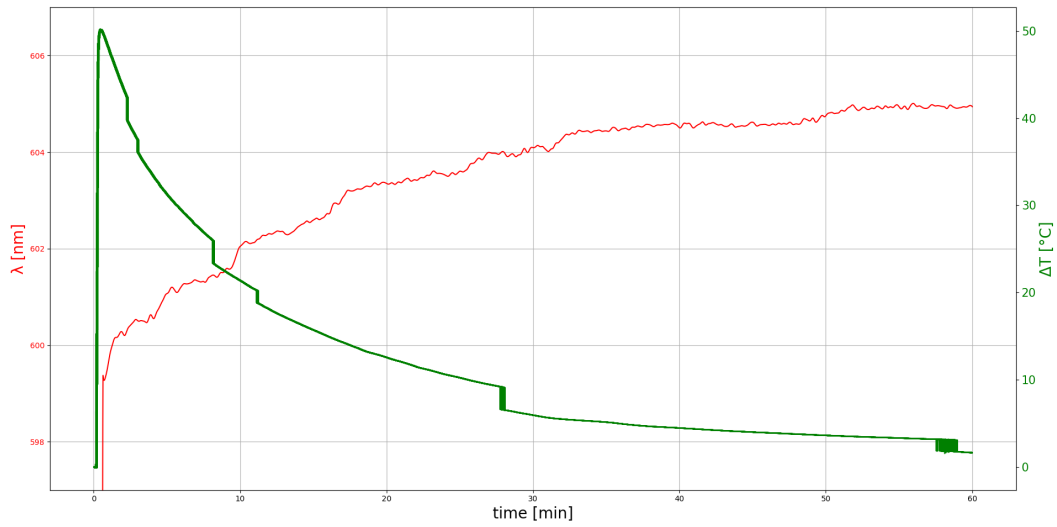


Figure 5.21: Wavelength of the dips filtered and temperature.

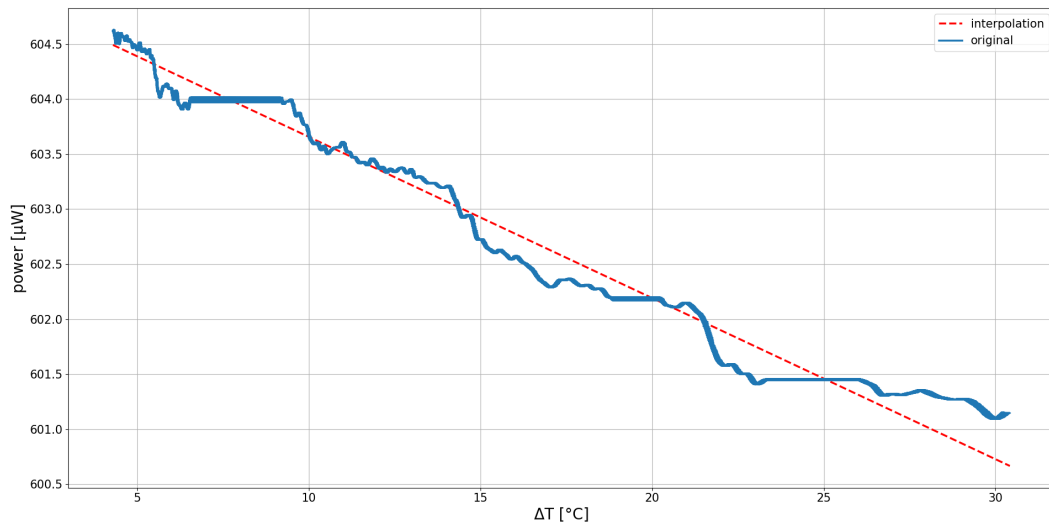


Figure 5.22: Acquired power in function of the temperature with interpolation.

### Test 3

In Fig. 5.23 it is again reported the acquisition of wavelength and temperature with the interpolation applied on each spectrum (black curve). The temperature has a variation of  $25\text{ }^{\circ}\text{C}$  leading to a wavelength red shift of  $2\text{ nm}$ . In Fig. 5.24 the FIR filter is applied. Also for this test the relation between wavelength and temperature is reported in Fig. 5.25, and the interpolation with a line allows the computation of  $c_1 = -0.2\text{ nm}/^{\circ}\text{C}$ .

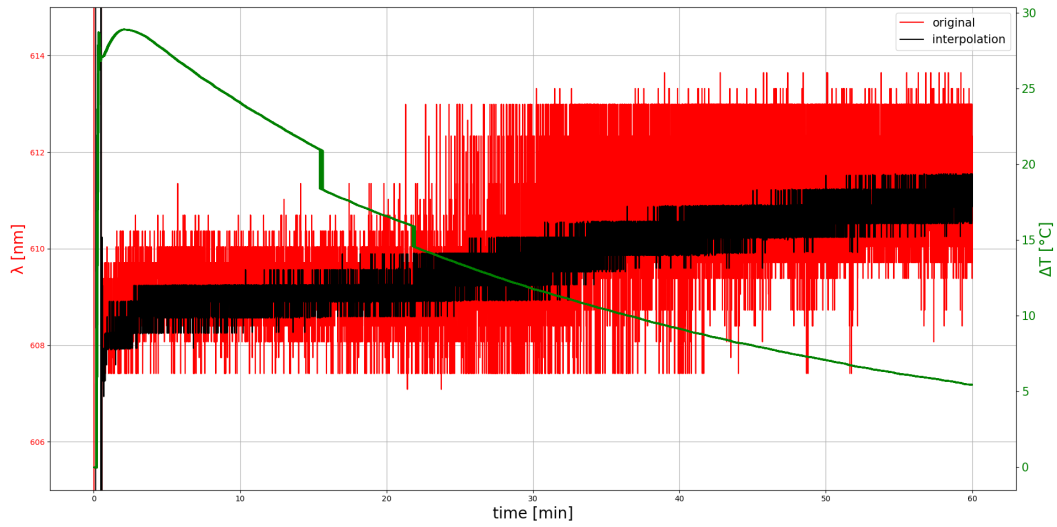


Figure 5.23: Wavelength of the dips and temperature.

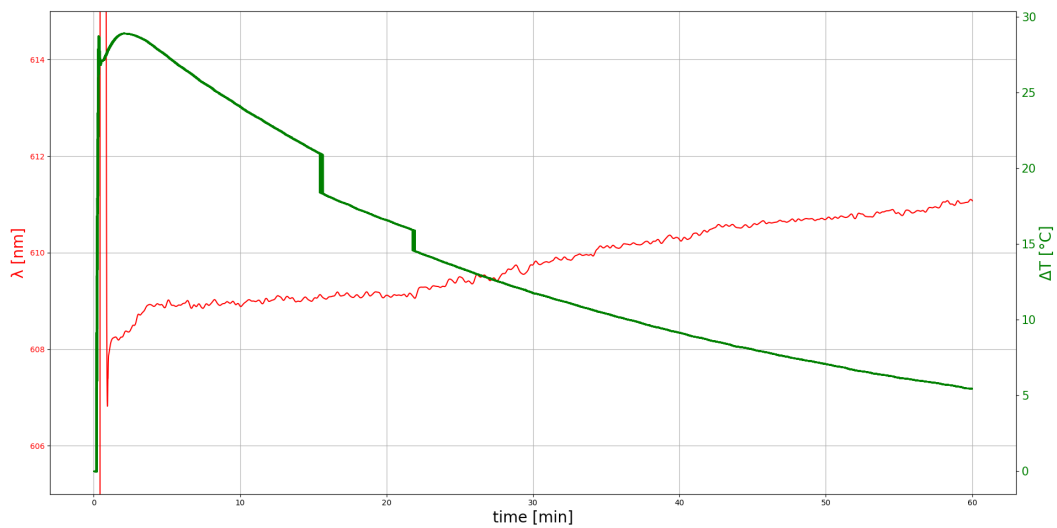


Figure 5.24: Wavelength of the dips filtered and temperature.

Since three tests have been done the value of  $c_1$  can be computed in a more accurate way. In Tab. 5.2 are summarised the results.

From Tab. 5.2 can be computed a mean value of the coefficient  $c_1$ :  $c_1 = -0.22 \text{ nm}/^\circ\text{C}$ . The evaluation of  $c_1$  is done on the interval where the characteristic presents a more linear behaviour, removing the parts that present a step. For more accurate evaluation of the correction coefficient a temperature sensor with less steps and uncontrolled behavior

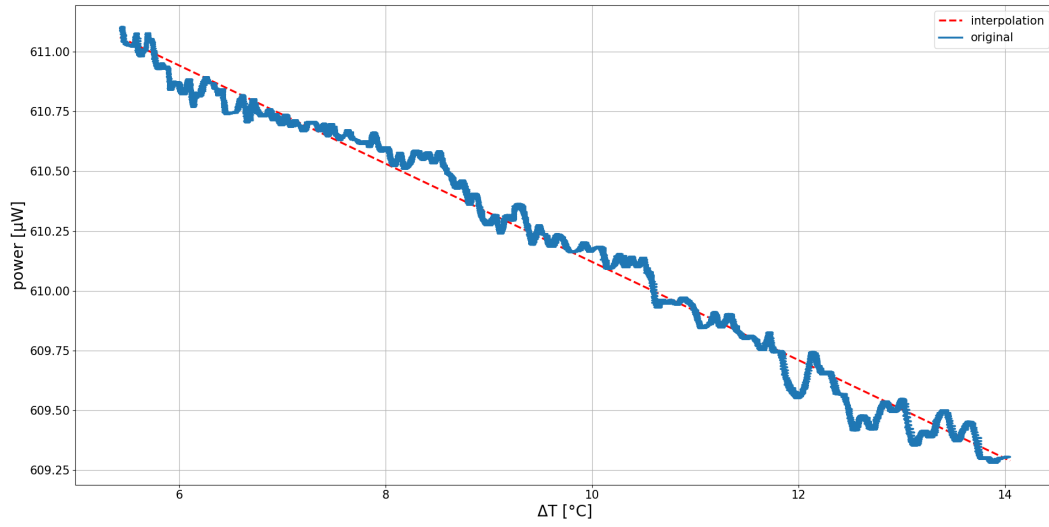


Figure 5.25: Acquired power in function of the temperature with interpolation.

Table 5.2: Summary of the computation of the temperature coefficient, wavelength interrogation.

Test	$\Delta t$	$\Delta T$	$\Delta \lambda$	$c_1$
1	60 min	30 °C	15 nm	-0.32 nm/°C
2	60 min	50 °C	5 nm	-0.14 nm/°C
3	60 min	25 °C	2 nm	-0.21 nm/°C

is needed. From now on the computation of the refractive index can be done in a more accurate way removing the contribution of the temperature from the acquired wavelength shift.



# Chapter 6

## Low-cost set-up

### 6.1 Experimental set-up and materials

The set-up used for the analysis of the performances with very low cost devices is based on the intensity interrogation method, being very similar to the one implemented in Chapter 4.

In this case the power meter has been substituted by a photodiode. In this way the set up can be controlled by an electronic board without the need of a computer to control the devices. Also the FBG temperature sensor has been substituted by a NTC thermistor in order to avoid using the Ibsen interrogator, which is bulky and really expensive and so not suitable for the application. The computer is needed only to read the serial output of the board, while in the future the output could be send to a remote device, allowing the device to be really portable and usable everywhere.

The response of the photodiode to RI variations is the same of the one reported in Chapter 4 for the power meter: since the LED is the same as before also in this case, in the RI range of contaminated water, an increase of RI will cause an increase of the power read by the power meter and so of voltage at the output of the photodiode.

Another variation with respect to the previous setup is the fiber positioning: since the vibration induced by the movement of the water in the plate is not suitable for high-precision measurements a metallic box has been designed, even if is too large to be used for real application and the measures still have some reproducibility problems.

#### 6.1.1 Design of the fiber holder and set-up

The metallic box is designed using FreeCAD, a free design tool that allows modeling 3D objects. The box presents two grooves on the sides to allow the fiber to exit without being bent from the lid. Inside the box it is also present a holder for the fiber: two raised rectangle designed to hold the fiber reducing vibrations and unwanted movements. Also the two rectangles present grooves to hold properly the fiber allowing better adherence of the resin to the surface. Moreover the two rectangles are removable in order to allow the fiber substitution without removing the resin, allowing changing the fiber without damaging it. In Fig. 6.1 is shown the 3D view of the box, the removable fiber holder and the lid. The optical set-up is a transmission configuration based on the intensity

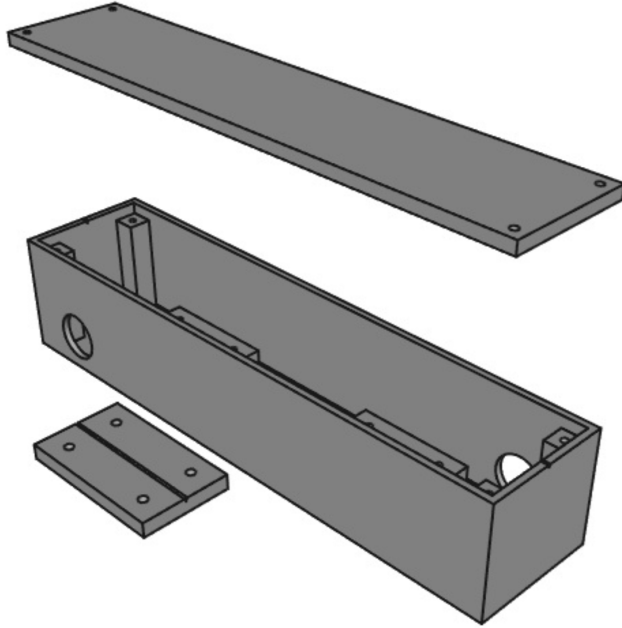


Figure 6.1: 3D view of the fiber holder.

interrogation method, with a single wavelength light and a photodiode.

- The single wavelength LED is the same used in the previous setup: a Ratioplast 660 nm LED with SMA connector (905SE660SM106 [27]), driven by the Arduino board.
- On the opposite side of the fiber is spliced to a bare fiber, to simplify the connection of all the components, and then connected a photodiode (EPD-660-5 from Roithner [29]), connected through a holder from Thorlabs (S1LEDM [30]) that allows coupling a T-1 3/4 with a SMA fiber connector.
- Again on both ends the bare fiber is connected to the instruments with a Thorlabs Universal Bare Fiber Terminator (BFT1 [15], Fig. 3.1c, left) equipped with a SMA905 multimode connector (B10440A [16], Fig. 3.1c, right).

Since the setup must be low cost the usage of a FGB sensor for the temperature compensation is not suitable because it requires a really expensive acquisition device. The FBG has been substituted by a NTC thermistor. Both the photodiode and the thermistor are connected to the acquisition board, which provides also the current for the LED. In this way the acquisition and power supply system becomes small and cheap. The board is an Arduino Uno Rev3 [31], a microcontroller board based on the ATmega328P, that allows connecting both digital and analogical input/output. In Fig. 6.2 is shown the complete setup.

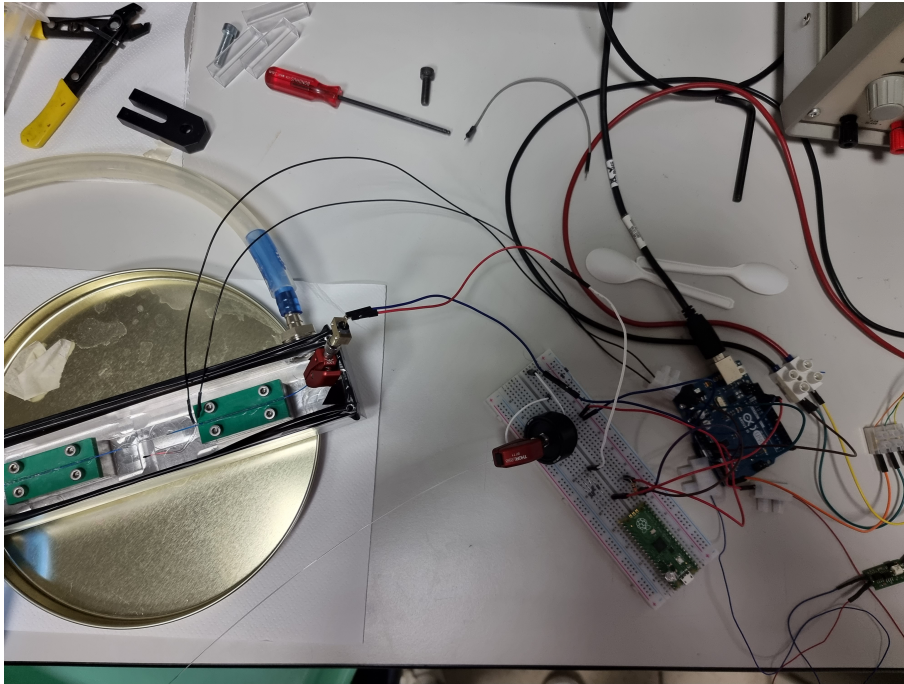


Figure 6.2: Intensity interrogation setup.

## 6.2 Experimental tests

The first test is done using a patchcord, without using the SPR sensing fiber, to measure the intensity of the LED and analyse the noise contribution. At the same time also the thermistor is tested in order to understand if the acquisition software is working properly. In Fig. 6.4 is reported the result of the first acquisition:

- The voltage acquisition represents the acquisition of the photo-diode output and is directly proportional to the intensity and so to the refractive index in the case of SPR sensor.
- The voltage is quite noisy but is due to the poor quality of the integrated ADC available on the Arduino board. Applying a FIR filter ( $sample\_rate=50$ ,  $f\_cutoff=0.1$  Hz) as for the previous interrogation methods is possible to have a smoother signal (Fig. 6.4).
- The temperature is constant at room temperature (about  $27^{\circ}\text{C}$  since the tests are done during the summer period). The peak in the temperature acquisition is due to the contact between the thermistor and a finger, obtaining a peak temperature of about  $36^{\circ}\text{C}$ .

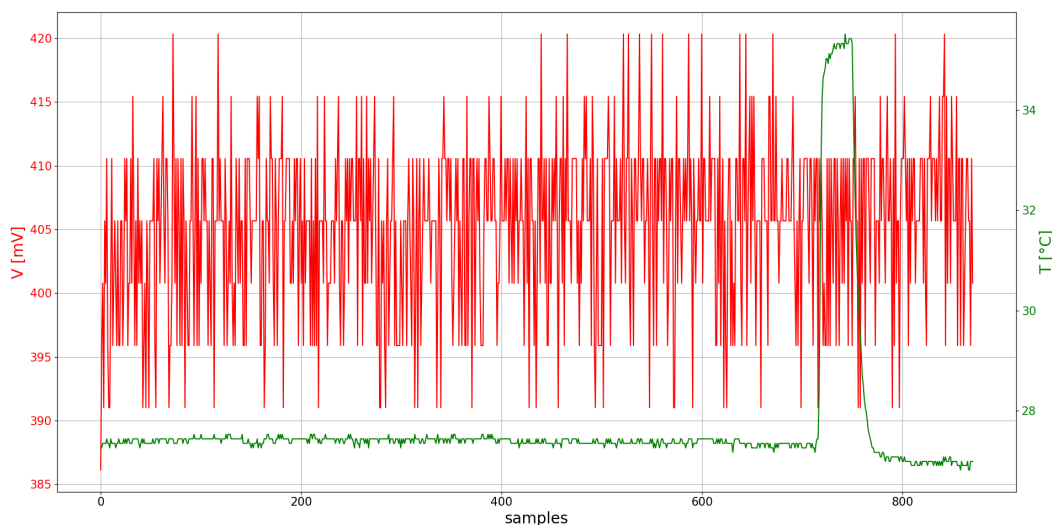


Figure 6.3: Voltage and temperature acquisition with patchcord.

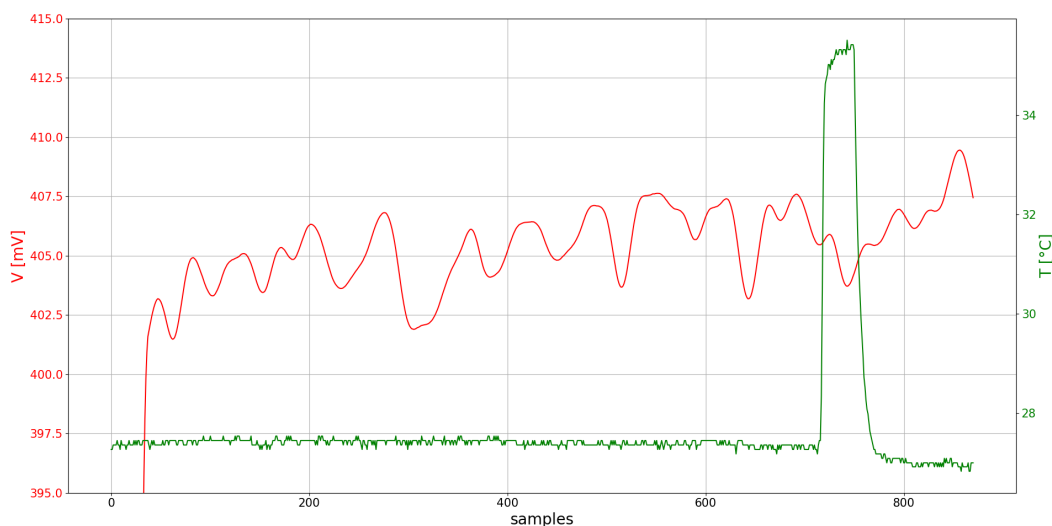


Figure 6.4: Voltage and temperature acquisition with patchcord, filtered.

### 6.2.1 Acquisition with temperature compensation

The acquisition is performed with room temperature tap water to study the stability of the SPR and temperature sensors. As reported in Fig. 6.5 the voltage acquisition, apart from the noise also seen before, presents a really small variation that can be explained considering the temperature changes during the acquisition due to the presence of an air conditioning system in the room. Also in this case adding a filter ( $sample\_rate=50$ ,  $f\_cutoff=0.1$  Hz) both on the voltage and the temperature allows smoothing the signals

even if some fluctuations are still present (Fig. 6.6). The presence of fluctuations are due, as already reported, to the poor quality of the ADC on the Arduino board. Adding an external ADC with an higher number of bits allows acquiring better the voltage allowing an higher precision on the RI measurements. The presence, in both measurements, of a

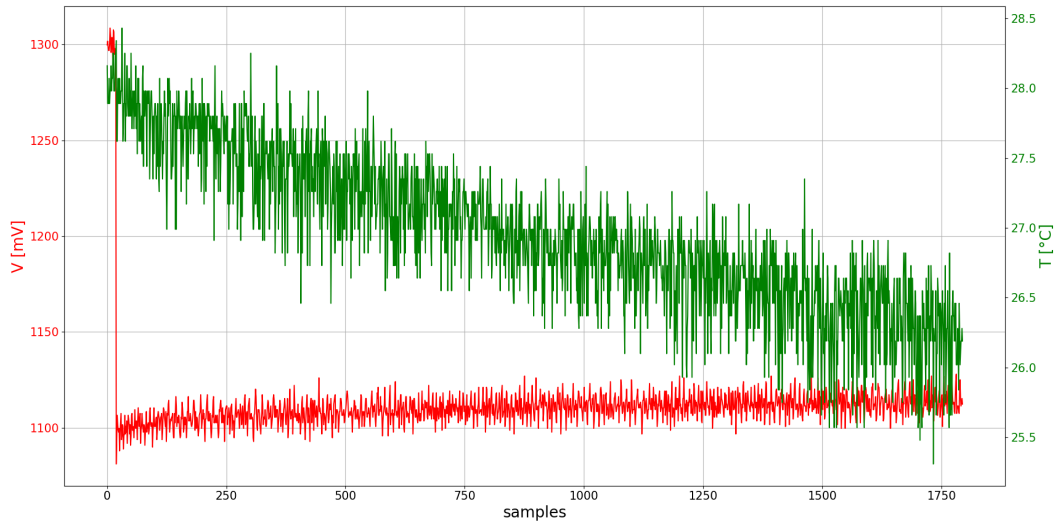


Figure 6.5: Voltage and temperature acquisition with room temperature tap water.

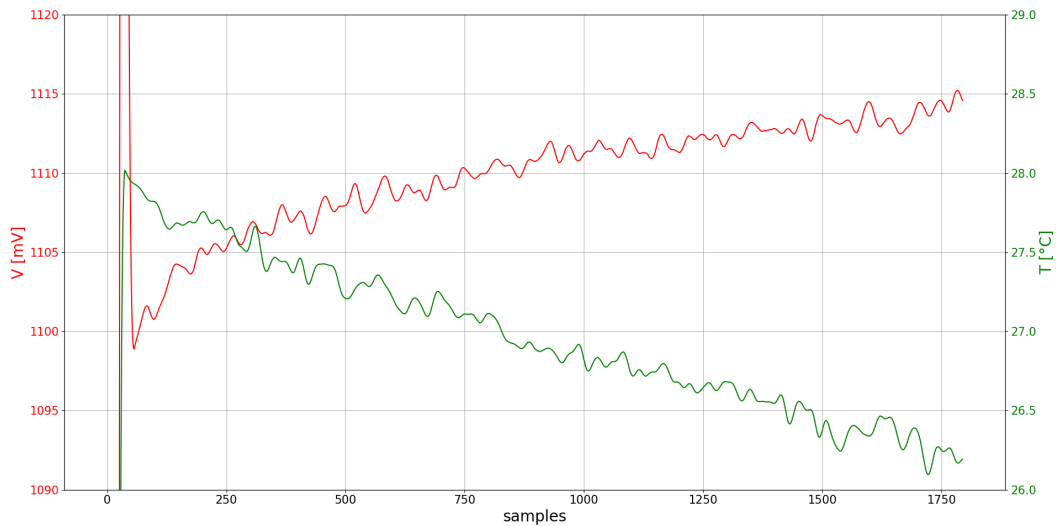


Figure 6.6: Voltage and temperature acquisition with room temperature tap water, filtered.

step at the beginning of the acquisition, both before and after the filter (Fig. 6.5 and 6.6), is due to the fact that at the start of the acquisition the dielectric around the sensors is

air and only after few seconds the water is added, causing a large change of temperature and refractive index. Also in this case, with the intensity interrogation method using a photodiode, as it can clearly be seen in Fig. 6.6, there is a correlation between the variation of voltage and temperature.

### Temperature compensation

To better evaluate the correlation between the two values and compensate the temperature also in this case, as in Chapter 5, some further test using hot water left cooling at room temperature have been done and are reported in the following.

In Fig. 6.7 is reported the result of the first acquisition:

- The acquisition has been performed for 90 minutes, with a temperature variation of 30 °C, from 60 °C to 30 °C.
- The temperature and the voltage at the very beginning of the plot present a step: this is due to the fact that the hot water was added after the start of the acquisition.
- Also in this case the temperature and the voltage are very similar, suggesting again a linear relation.
- The dip in the interval between 0 and 500 samples is caused by the high temperature of the water, that probably modifies the fiber and the gold coating introducing some dilatation or strain. Repeating the test with colder water (from 40 °C) the dip is not present anymore, as reported in the following section.

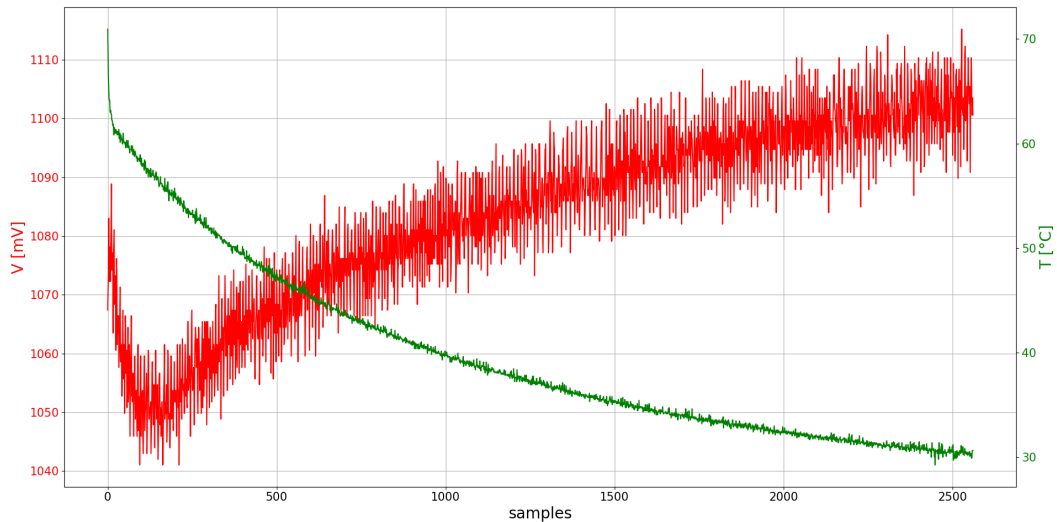


Figure 6.7: Voltage and temperature acquisition with hot tap water.

Also in this case both the temperature and the voltage are filtered with a FIR filter ( $sample\_rate=50$ ,  $f\_cutoff=0.1\text{Hz}$ ), removing part of the noise that does not allow

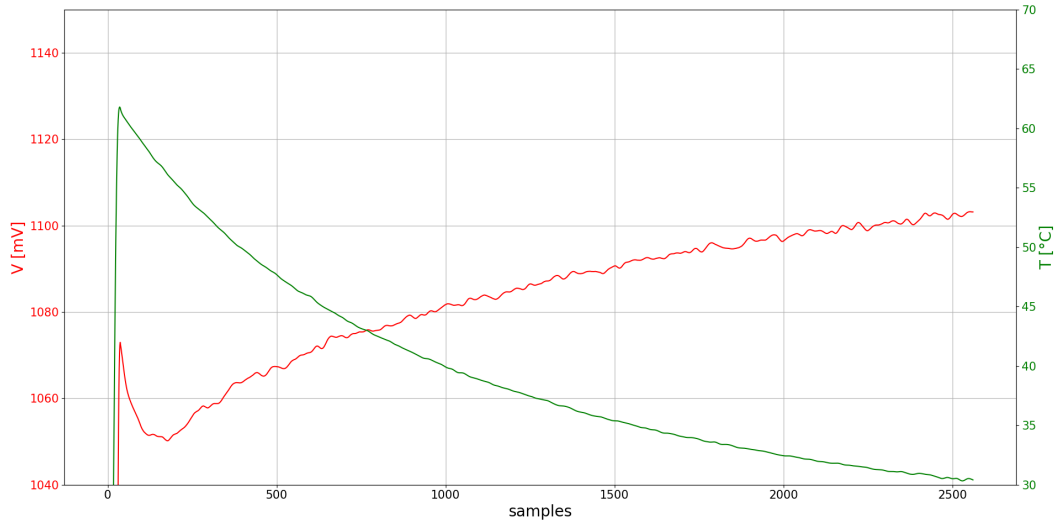


Figure 6.8: Voltage and temperature acquisition with hot tap water, filtered.

having a good resolution in sensing (Fig. 6.8). In Fig. 6.9 is reported the voltage in function of the temperature, and as suggested before the relation is linear: from the angular coefficient of the interpolating line the value of  $c_1$  can be obtained ( $-1.97443 \text{ mV}/^\circ\text{C}$ ).

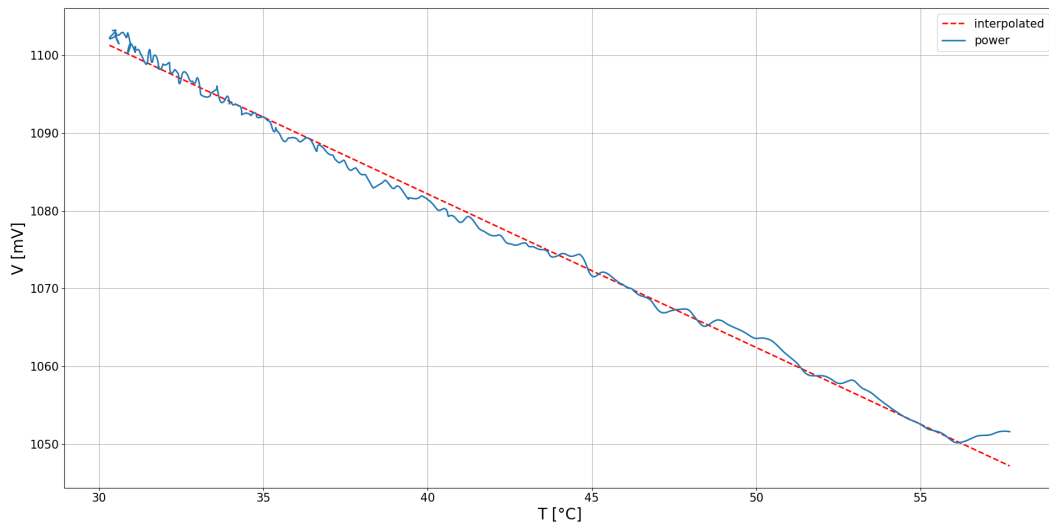


Figure 6.9: Voltage in function of temperature.

The temperature compensation is done knowing that:

$$V = V_0 + c_1\Delta T + c_2\Delta n \quad (6.1)$$

where

$$\Delta T = T - T_0 \quad \Delta n = n - n_0$$

The values  $V_0$ ,  $T_0$  and  $n_0$  refers to the values in the initial conditions, ideally at  $25^\circ\text{C}$  using distilled water.

Since in this case the water composition is constant  $\Delta n$  can be considered equal to zero, simplifying Eq. 6.1 by removing the last term. In this case the computation of the voltage is reduced to Eq. 6.2.

$$V = V_0 + c_1\Delta T \quad (6.2)$$

In this case  $V_0$  and  $T_0$  are referred to the initial condition of this specific acquisition: tap water at  $30^\circ\text{C}$ .

In Fig. 6.10 is reported the original, filtered, voltage acquisition with the same acquisition after the temperature compensation applying Eq. 6.2 using  $c_1 = -1.97443 \text{ mV}/^\circ\text{C}$ . The compensation in this case is not useful and is performed only to show that removing the temperature contribution the voltage acquisition is stable when the refractive index does not change. In the case of a real acquisition that must be compensated Eq. 6.1 must be used with  $c_1 = -1.97443 \text{ mV}/^\circ\text{C}$ .

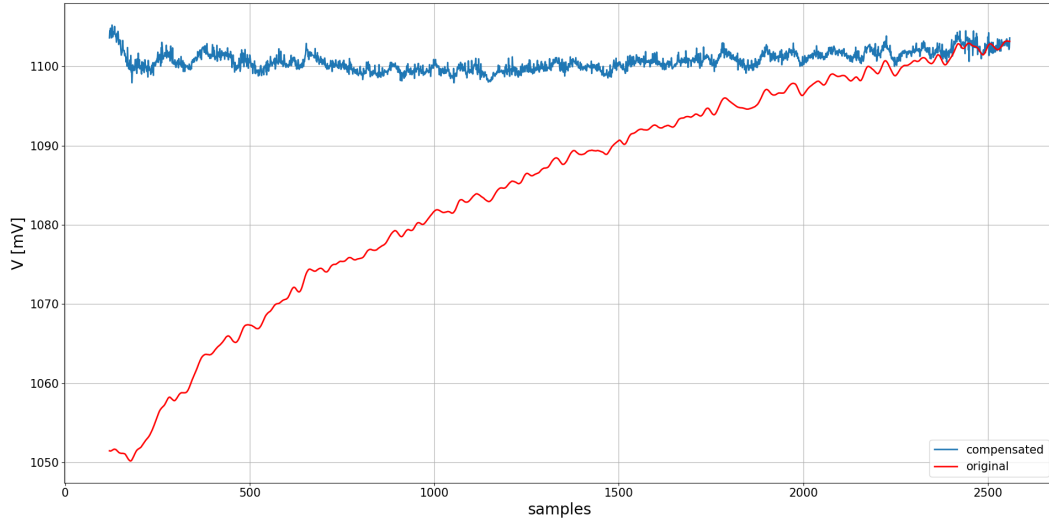


Figure 6.10: Acquired voltage with compensation.

## 6.3 Real measurements

Also in this case some tests with real samples are done. In particular three water sample are collected from Lago Maggiore (at Angera and Stresa) and from Lago d’Orta. For each sample five different test are done:

- Control: 400 mL of water from the lakes;
- Diluted control: 400 mL of water from the lakes and 1600 mL of tap water;
- Sanitized water: the “Diluted control” after sanitation in a sanitation device. The sanitation is performed three times and the acquisition is done every time.

Only for the Angera’s sample the control acquisition is not present because the acquisition is performed with a slightly different setup (the splice between the SPR fiber and the bare fiber has been changed after this first test) and so the acquired values of voltage are not comparable with the following, due to the different losses introduced by the two splices, and so the test is not taken into account.

### 6.3.1 Lago Maggiore - Angera

In Fig. 6.11 it is reported the voltage acquisition of the different test performed with the Angera’s sample. As said before the control test is not reported due to variation in the setup. Each test lasts 5 minutes in order to acquire more data to have a more accurate acquisition. As for the other test performed before, also in this case the acquisition is noisy so, to have a better result, all the acquisition are filtered with `sample_rate=50` and `f_cutoff=0.1` Hz. The result is shown in Fig. 6.12: some considerations are reported in the following.

- The values of voltage are compensated in temperature after the filtering.
- The test performed after the first sanitation presents some dips: are due to human interference during the test, so the data that can be considered relevant are limited to about 3.5 min;
- The four curves present a different mean value between each other, maintaining a similar, constant, behaviour.
- The shift between the mean value of the curves is the relevant information of the acquisition: different samples of water leads to different output voltages.

### 6.3.2 Lago Maggiore - Stresa

In Fig. 6.13 it is reported the acquisition performed with Stresa’s samples. Also in this case each acquisition lasts 5 minutes and is filtered with `sample_rate=50` and `f_cutoff=0.1` Hz (Fig. 6.14), some consideration are reported in the following.

- The values of voltage are compensated in temperature after the filtering.

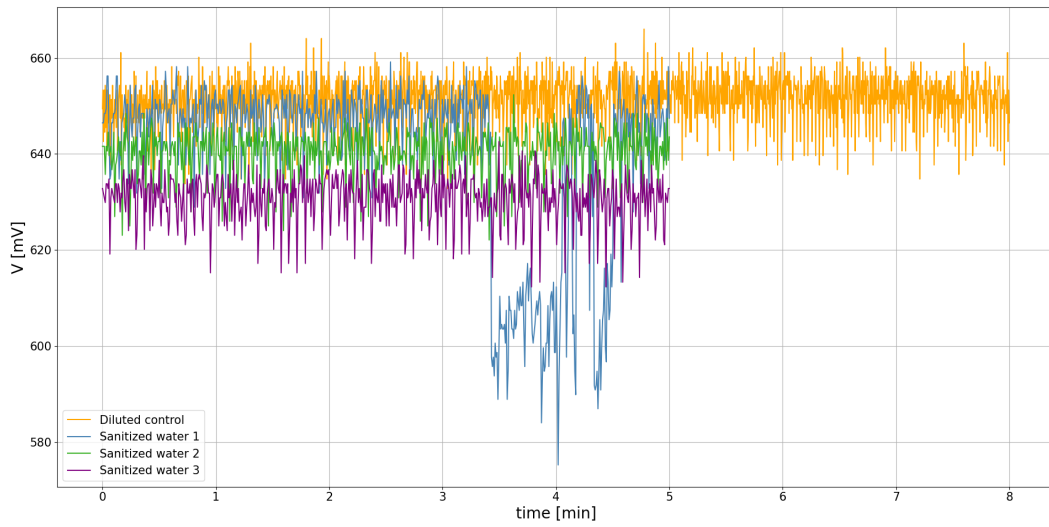


Figure 6.11: Voltage acquisition for Lago Maggiore - Angera.

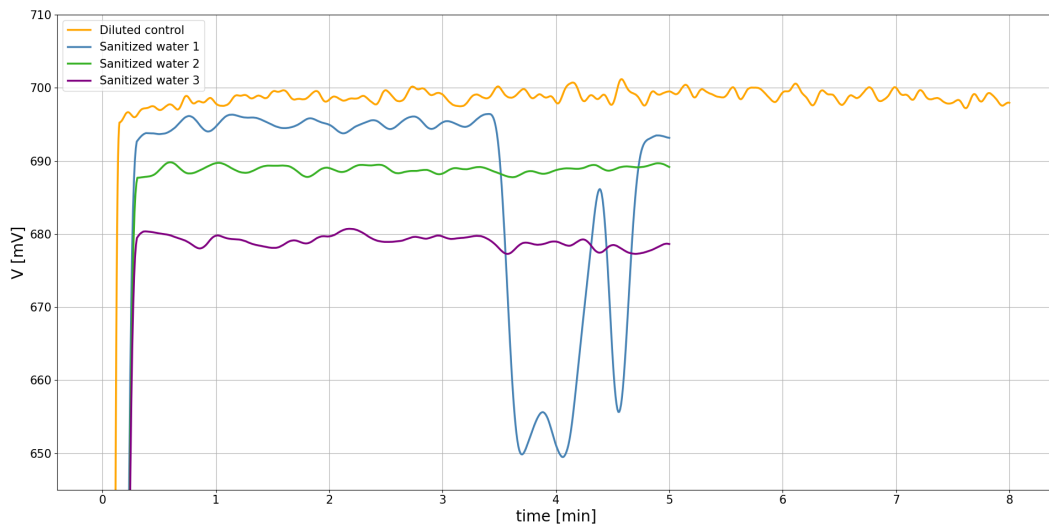


Figure 6.12: Voltage acquisition for Lago Maggiore - Angera, filtered and with temperature compensation.

- Five different acquisitions are reported, one for each sample. All the curves present a similar, constant behaviour, differing only for the mean value.
- The samples of the control and diluted water presents a similar mean value, while the three sanitized samples have a different, lower, value.

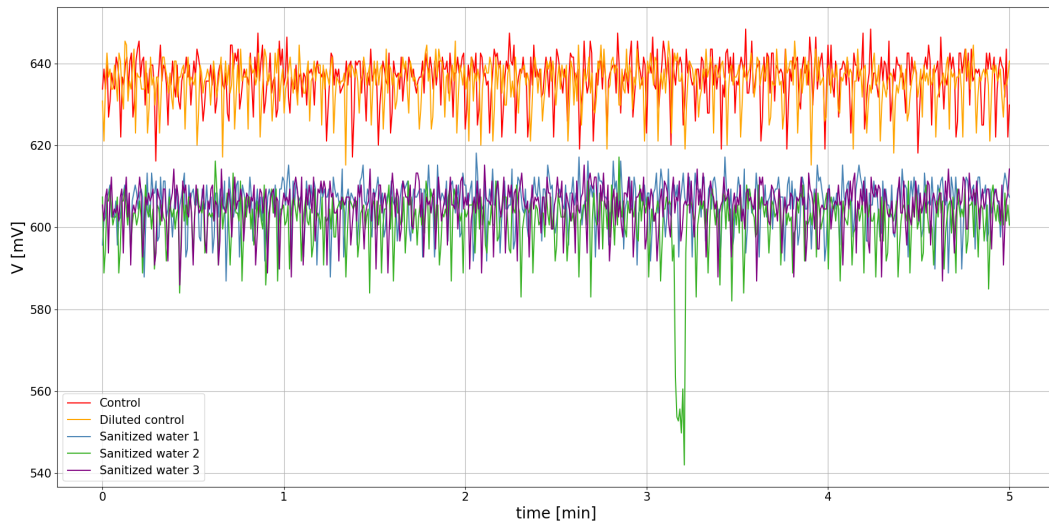


Figure 6.13: Voltage acquisition for Lago Maggiore - Stresa.

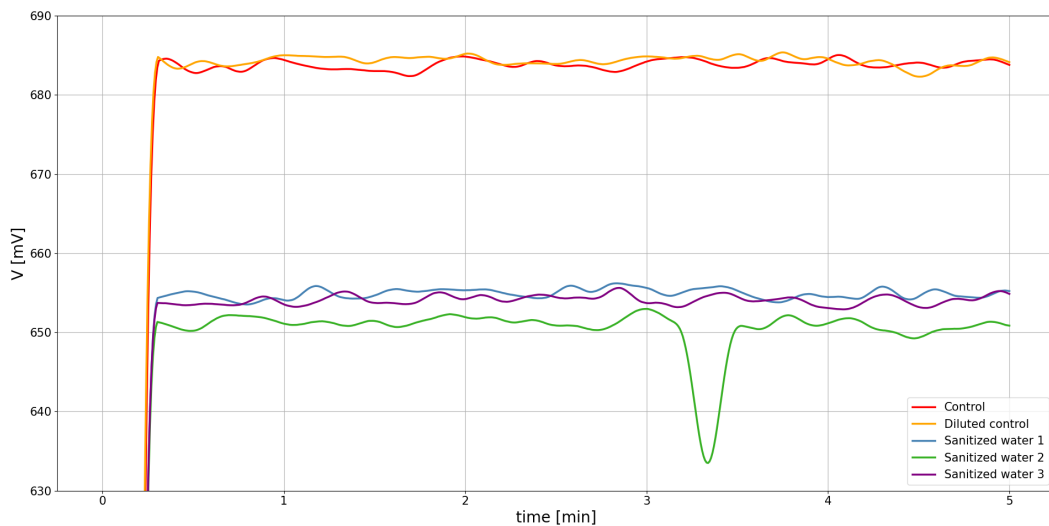


Figure 6.14: Voltage acquisition for Lago Maggiore - Stresa, filtered and with temperature compensation.

### 6.3.3 Lago d'Orta

In Fig. 6.15 is reported the acquisition performed with Orta's samples. Also in this case each acquisition lasts 5 minutes and is filtered with  $\text{sample\_rate}=50$  and  $f\_cutoff=0.1$  Hz (Fig. 6.16), some consideration are reported in the following.

- The values of voltage are compensated in temperature after the filtering.

- Five different acquisitions are reported, one for each sample. All the curves present a similar, constant behaviour, differing only for the mean value.
- In this case the curves have all a similar mean value except one that presents a lower value.

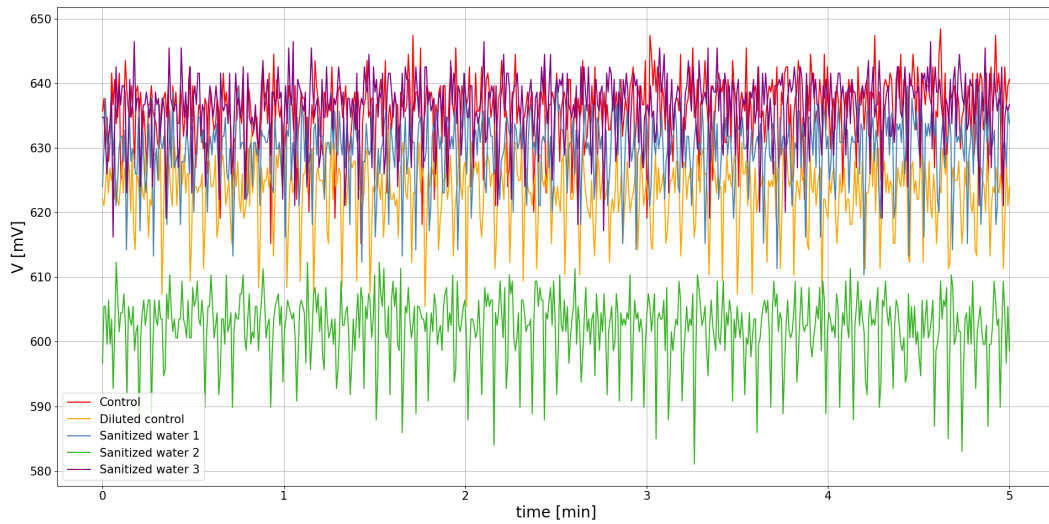


Figure 6.15: Voltage acquisition for Lago d'Orta.

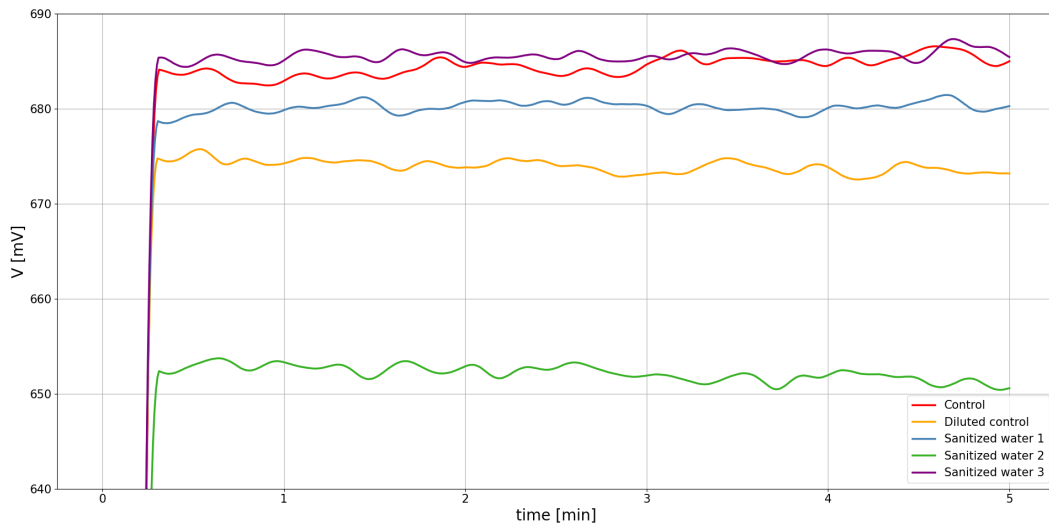


Figure 6.16: Voltage acquisition for Lago d'Orta, filtered and with temperature compensation.

## Results

Analyzing the three acquisition together it can be noticed that the results doesn't have a constant behavior, since the difference between the different samples dos not follow a constant pattern: considering for example the diluted control in the first two tests presents a value higher than the sanitized samples while in the last test presents a lower value. This is due to the poor quality of the setup: the designed box works properly if the water sample is the same and the refractive index is changed adding each time some new liquid. If the sample is completely different each time the box must be emptied and refilled. This procedure causes a modification of the entire setup since the mobile connectors are not suitable to be moved. This modification causes a small difference in the acquired voltage, independently on the dielectric that surrounds the SPR sensor. To overcome this issue some modifications to the setup must be done. Can be useful to substitute the mobile connectors with a splice, to maintain fixed the junction and repeatable the behavior of the sensor.



# Chapter 7

## Conclusion

The main aim of the thesis is to understand if different acquisition techniques are suitable for the development of a low-cost device to detect refractive index changes in water samples.

Three main configurations have been designed and tested, two based on the intensity interrogation method and one on the wavelength interrogation method. The last configuration, analyzed first, is the one that allows better stability and sensitivity, having on the other hand the more complex and expensive setup, since it uses broadband light sources and optical spectrometers. Moreover the acquisition through the spectrometer needs to be performed with a computer with LabVIEW, requiring bulky instruments and a lot of space.

The setup based on the intensity interrogation requires only narrow band LED and a power meter. It allows a good sensitivity with a smaller and less expensive setup. Even if the setup is not yet low-cost and enough small to be installed anywhere, also because the interrogation of the power meter must be performed with a computer.

The third configuration, again based on the interrogation method, uses a photo diode instead of a power meter to acquire the intensity of the light at the end of the fiber. The use of the photodiode has some advantages, such as the fact that the photodiode is smaller and fifty times cheaper than the power meter. Moreover the photodiode does not require a computer to be acquired, a micro-controller, e.g. the one present on an Arduino board, is sufficient for the scope, being small and cheap enough for the application of the sensor almost everywhere.

The temperature is a parasitic effect that does not allow an accurate measurement of the refractive index. The temperature affects all the configurations in a similar way ( $0.22 \text{ nm}/^\circ\text{C}$ ,  $0.0053 \mu\text{W}/^\circ\text{C}$  and  $2 \text{ mV}/^\circ\text{C}$ ), for this reason a compensation procedure is proposed (Chapter 5). The compensation is based on the external measurement of the temperature through a sensor, that can be a FBG in the case of more complex and expensive setup or a NTC in the case of the low cost set up, in order to be acquired directly with the acquisition board.

To improve the setup, both on the point of view of the compactness and of the performances, some modifications can be done, such as the substitution of the mobile

connectors with splices to have better repeatability also with different water samples. Also the quality of calibration can affect the precision of the sensor, for this reason can be useful to calibrate the device using calibrated refractive index liquids, that allows knowing exactly the RI of the solution, removing the error introduced by handmade water-alcohol solutions. Also the fiber holder can be improved to be more efficient: a smaller and easier-to-handle box can improve the way the measures are performed, allowing an higher precision. Moreover the addition of a coupler and a second photodiode allows to monitor in real time the behaviour of the LED source removing the noise and the fluctuations due to the light source. To improve the compactness of the device also a IoT transmitter can be added in order to send the acquired data to a remote device, making the setup really usable everywhere.

# Bibliography

- [1] <https://www.emergenresearch.com/industry-report/water-quality-monitoring-market>.
- [2] <https://sdgs.un.org/goals/goal6>.
- [3] WHO/UNICEF, “Progress on household drinking water, sanitation and hygiene 2000-2020: Five years into the sdgs,” 2021.
- [4] WHO, “Guidelines for drinking-water quality.”
- [5] W. Yusmawati and W. M. M. Yunus, “Optical properties and kinetic behavior of chlorine in pure water and swimming pool water using surface plasmon resonance technique,” *American Journal of Applied Sciences*, vol. 4, pp. 1024–1028, Dec 2007.
- [6] A. K. Sharma and B. Gupta, “Theoretical model of a fiber optic remote sensor based on surface plasmon resonance for temperature detection,” *Optical Fiber Technology*, vol. 12, no. 1, pp. 87–100, 2006.
- [7] V. Yesudasu, H. S. Pradhan, and R. J. Pandya, “Recent progress in surface plasmon resonance based sensors: A comprehensive review,” *Heliyon*, 2021.
- [8] R. B. M. Schasfoort, ed., *Handbook of Surface Plasmon Resonance*. The Royal Society of Chemistry, 2017.
- [9] A. K. Sharma, R. Jha, and B. D. Gupta, “Fiber-optic sensors based on surface plasmon resonance: A comprehensive review,” *IEEE Sensors Journal*, vol. 7, no. 8, pp. 1118–1129, 2007.
- [10] B. D. Gupta, A. M. Shrivastav, and S. P. Usha, “Surface plasmon resonance-based fiber optic sensors utilizing molecular imprinting,” *Sensors*, vol. 16, no. 9, 2016.
- [11] A. Bano, “Optical fiber sensors for water quality monitoring,” 2020.
- [12] <https://www.thorlabs.com/thorproduct.cfm?partnumber=MBB1F1>.
- [13] <https://www.thorlabs.com/thorproduct.cfm?partnumber=LEDD1B>.
- [14] <https://www.avantes.ru/en/spectrometer/avaspec3648.php>.
- [15] <https://www.thorlabs.com/thorproduct.cfm?partnumber=BFT1>.
- [16] <https://www.thorlabs.de/thorproduct.cfm?partnumber=B10440A>.
- [17] <http://tfilter.engineerjs.com>.
- [18] <https://scipycookbook.readthedocs.io/items/FIRFilter.html>.
- [19] M. Born, E. Wolf, A. B. Bhatia, P. C. Clemmow, D. Gabor, A. R. Stokes, A. M. Taylor, P. A. Wayman, and W. L. Wilcock, *Principles of Optics: Electromagnetic Theory of Propagation, Interference and Diffraction of Light*. Cambridge University Press, 7 ed., 1999.
- [20] P. Schiebener, J. Straub, J. M. H. Levelt Sengers, and J. S. Gallagher, “Refractive index of water and steam as function of wavelength, temperature and density,”

- Journal of Physical and Chemical Reference Data*, vol. 19, no. 3, pp. 677–717, 1990.
- [21] E. Sani and A. Dell’Oro, “Spectral optical constants of ethanol and isopropanol from ultraviolet to far infrared,” *Optical Materials*, vol. 60, pp. 137–141, 2016.
  - [22] G. Perrone, “Industrial photonics: Lecture notes,”
  - [23] R. Orta, “Passive optical components: Lecture notes,”
  - [24] <https://refractiveindex.info/?shelf=mainbook=SiO2page=Malitson>.
  - [25] <https://www.thorlabs.com/thorproduct.cfm?partnumber=LED670L>.
  - [26] <https://www.thorlabs.com/thorproduct.cfm?partnumber=L405G2>.
  - [27] <http://www.ratioplast.info/pdf/rpo/905/SE/E05SE660SM106.pdf>.
  - [28] [https://www.thorlabs.com/thorproduct.cfm?partnumber=PM16\\_120](https://www.thorlabs.com/thorproduct.cfm?partnumber=PM16_120).
  - [29] [http://www.roithnerlaser.com/pd\\_selective.html](http://www.roithnerlaser.com/pd_selective.html).
  - [30] <https://www.thorlabs.com/thorproduct.cfm?partnumber=S1LEDM>.
  - [31] [https://docs.arduino.cc/hardware/uno\\_rev3](https://docs.arduino.cc/hardware/uno_rev3).